Technische Universität Dortmund

Dissertation

Ultrafast coherent lattice dynamics coupled to spins in the van der Waals antiferromagnet $FePS_3$

Arbeit zur Erlangung des akademischen Grades

Dr. rer. nat.

von

Fabian Mertens

Geb. in Wickede (Ruhr)

AG Cinchetti

Fakultät Physik

November 2023

technische universität dortmund

Accepted by the Faculty of Physics of the TU Dortmund University, Germany.

Examination board:
Prof. Dr. Mirko Cinchetti
apl. Prof. Dr. Ilya Akimov
Prof. Dr. Gudrun Hiller
PD Dr. Dominik Elsässer

Submission date:	23^{th} November 2023
Date of the oral examination:	30^{th} January 2024

Abstract

2D materials, like the antiferromagnetic van der Waals semiconductors $FePS_3$ studied in this work, open up new possibilities for technological applications due to the unique interaction of their magnetization with electronic, optical, and mechanical properties. Furthermore, they provide the potential to study magnetism and magnetization dynamics in reduced dimensions. Up do date, the coherent control of the magnetization of these materials has barely been studied. Our research addresses this gap by using ultrashort light pulses. In this context, time-resolved studies can give an insight into the evolution of the light-induced dynamics, which essentially require a dedicated experimental setup.

In this thesis, we present a comprehensive study on the development and application of a table-top laser setup designed for magneto-optical pump-probe experiments and adaptable for the investigation of microscopic samples. The system employs two optical parametric amplifiers, with a tunable photon-energy range of 0.5 eV - 3.5 eV for both the pump and the probe beam. Remarkable is the high pump amplitude modulation rate at 50 % of the laser repetition rate, realized via the integration of an electro-optical modulator, blocking every second pump pulse. Combined with a high-frequency digitizer, performing single pulse detection, our system can achieve a high sensitivity, down to 50 µdeg of the probe polarization rotation. The setup can apply magnetic fields of up to ± 9 T, and voltages in the kV regime while providing a temperature control between 4 K-420 K.

The functionality of the setup's systems is demonstrated by performing static Kerr-rotation and ultrafast demagnetization measurements in a cobalt single crystal as a function of the most important experimental parameters.

The major part of this thesis is dedicated to our studies on a coherent optical lattice mode of terahertz frequency triggered by femtosecond laser pulses in the antiferromagnetic van der Waals semiconductor $FePS_3$. This specific 3.2 THz phonon mode shows a close relation to the antiferromagnetic order, as it vanishes above the Néel temperature and hybridizes with a magnon mode in the presence of a magnetic field. We investigate it as a function of sample temperature, probe polarization, excitation photon energy and externally applied magnetic fields. The resonant excitation of a crystal-field split electronic *d*-*d* transition efficiently pumps the displacive excitation process of the mode, while the magnetic linear dichroism is identified as the magneto-optical effect, which reflects the phonon mode in the probe rotation. By applying magnetic fields of up to 9 T we can generate and observe the coherent hybridized phonon-magnon mode, thus exploiting the hybridization to excite coherent spin-dynamics. Furthermore, we investigate the coherent phonons in the bulk form of $FePS_3$ and in an exfoliated flake with a thickness of 380 nm.

Kurzfassung

2D-Materialien, wie der in dieser Arbeit untersuchte antiferromagnetische van der Waals Halbleiter $FePS_3$, können, aufgrund der einzigartigen Wechselwirkung ihrer Magnetisierung mit elektronischen, optischen oder mechanischen Eigenschaften, neue technologische Möglichkeiten bieten. Vorallem bieten sie aber auch eine Möglichkeit, Magnetismus und magnetische Dynamiken in reduzierten Dimensionen zu untersuchen. Trotzdem gibt es bis heute kaum Studien zur kohärenten Kontrolle der Magnetisierung solcher Materialien. Die Herangehensweise unserer Forschung zu dieser Lücke beruht auf der Verwendung ultrakurzer Lichtpulse. Hierbei können zeitaufgelöste Messungen Einblicke in die lichtinduzierten Dynamiken ermöglichen, wofür ein spezialisiertes Experiment notwendig ist.

In dieser Arbeit stellen wir eine Studie zur Entwicklung und Anwendung eines Laseraufbaus für magnetooptische Experimente vor, das an die Untersuchung mikroskopischer Proben angepasst werden kann. Das System verwendet zwei optische parametrische Verstärker mit einstellbaren Photonenenergien zwischen 0,5 eV - 3,5 eV sowohl für den Pump- als auch für den Probe-Strahl. Die Pump-Pulse werden mit hoher Frequenz durch einen elektrooptischen Modulator, der jeden zweiten Pump-Puls blockiert, moduliert. Zusammen mit einem hochfrequenten Digitalisierer, der einzelne Pulse aufnehmen kann, erreichen wir so eine Genauigkeit von 50 µ° in der Detektion der Rotation der Probe-Polarisation. Der Aufbau kann Magnetfelder von bis zu ±9 T und Spannungen im kV-Bereich anlegen. Zusätzlich bietet er eine Temperaturregulierung zwischen 4 K und 420 K.

Die Funktionalität der einzelne Systeme innerhalb des Aufbaus werden durch Messungen der statischen Kerr-Rotation und der ultraschnellen Demagnetisierung in einem Kobalt-Einkristall erprobt und die Abhängigkeiten der wichtigsten experimentellen Parameter werden demonstriert.

Der Hauptteil der Arbeit liegt in der Untersuchung einer kohärenten Schwingungsmode mit THz Frequenz, die durch femtosekunden Laserpulse in $FePS_3$ angeregt wird. Dieses 3,2 THz Phonon ist eng mit der antiferromagntischen Ordnung verbunden, indem es oberhalb der Néel-Temperature verschwindet und bei angelgetem Magnetfeld eine Hybridisierung mit einer Magnon-Mode aufweist. Die optische Anregung eines kristallfeldaufgespaltenen *d*-*d*-Übergangs pumpt effizient den Anregungsprozess der Phononmode, während der magnetische Linearedichroismus als der dominierende, von dem Phonon modulierte, magneto-optische Effekt identifiziert wird. Durch das Anlegen von Feldern von bis zu 9 T können wir die hybridiserite Phonon-Magnon Mode anregen und somit kohärente Spindynamiken erzeugen. Wir untersuchen die Phononmode sowohl in einem makroskopischen $FePS_3$ Kristall, als auch in einer exfolierten Flake-Probe mit einer Dicke von 380 nm.

Contents

Introduction **1**

1 Theory **4**
1.1 Ferro- and Antiferromagnetism 4
1.2 Magnetic van der Waals materials 9
1.3 Magneto-optical effects 13

2 Experimental setup **18**
2.1 Pump-probe Spectroscopy 18
2.2 System Layout 20
2.3 Laser system 22
2.4 Balanced detection 24
2.5 Data acquisition 26
2.6 Magnet and cryostat 31
2.7 Microscopic pump-probe configuration 34
2.8 Experimental software and graphical user interface 37
2.9 Conclusion 40

3 Ultrafast demagnetization in Cobalt **41**
3.1 Basics of ultrafast demagnetization in ferromagnets 41
3.2 Static characterization 43
3.3 Pump fluence dependence 44
3.4 Temperature dependence 48
3.5 Pump photon energy dependence 48
3.6 Magnetic field dependence 50
3.7 Conclusion 51

4 Coherent lattice and phonon–magnonic dynamics in bulk $FePS_3$ **53**
4.1 Coherent excitation of the phonon modes 54
4.2 Pump-photon energy dependence 55
4.3 Probe polarization dependence 62
4.4 Temperature dependence 64
4.5 Excitation of a coherent hybridized phonon-magnon mode 67
4.6 Conclusion 71

5 Lattice and spin dynamics in flake FePS3 **72**
5.1 Sample 72
5.2 Pump-photon energy dependence 74
5.3 Temperature dependence 77
5.4 Flake degradation 79
5.5 Conclusion 80

6 Conclusion **82**

Bibliography **87**

Acknowledgements **99**

Introduction

The introduction of reliable femtosecond pulsed light sources in pump-probe experiments [1] led to the discovery of the ultrafast light-induced magnetization quenching as reported in the infamous work of Beaurepaire and Bigot published in 1996 [2] and eventually magnetic phenomena up to the terahertz-timescale have become experimentally accessible. The high peak power of the laser pulses enhances the generation efficiency of the higher-order effects, compared to continuous wave or nanosecond pulsed light sources. These nonlinear effects can be directly adapted as a probing mechanism, for example via second-harmonic generation [3, 4], but also provide a vast plethora of nonlinear mechanisms that expand the experimental possibilities from a technical point of view. Higher harmonic generation and optical parametric amplification allow the expansion of the accessible optical range of a single light source [5] and are available as implementations in turn-key optomechanical devices [6]. Furthermore, via the generation of supercontinuum light, even the simultaneous probing over large ranges became possible [7]. The explorable phenomena, based on these techniques, range from the ultrafast demagnetization to the coherent excitation of phonons [8] or magnons[9] and reach up to the demonstration that light pulses are capable of switching the magnetic orientation in ferro-[10], ferri-[11] as well as in antiferromagnets [12].

In parallel, the fabrication of atomically thin materials, starting with the investigation of graphene [13] and followed up by low-dimensional magnetical systems [14–17], offer a new perspective on the observation of physical properties in reduced dimensions. A prototypical material class well suited for investigating magnetism in two dimensions are the magnetic van der Waals materials [15]. Magnetic van der Waals materials exhibit only a weak interlayer nge coupling [18]. They can also be used to create specimens of low thickness by exfoliating defined layer numbers down to single atomic layers. In the case of one to few atomic monolayers, the magnetic character can be distinctly different from the bulk form, unveiling true reduced dimension effects, which have already been demonstrated in some materials down to the monolayer[19, 20]. In two dimensions, the magnetization strongly relies on the magnetocrystalline anisotropy, even leading to the full loss of long-range magnetic order in its absence, which makes the magnetization sensitive and possibly controllable via accessing the anisotropy. Especially in the group of MPS_3 (M=3d transition metal), the strong dependence of the magnetization on stacking layers[17], pressure[21], shear[22] and

even light[23] has already been demonstrated. It was shown that close relations between lattice modes and the magnetization are possible in this group of van der Waals materials [24]. All these possibilities to tune or tailor the magnetism highlight the importance of the MPS_3 group for technical applications. Moreover, the antiferromagnetic order of MPS_3 is particularly advantageous for specific applications where the absence of stray fields, the robustness against external perturbations and intrinsically fast spin dynamics are required.

Given the growing demand for computational and data storage capabilities, which is further accelerated by the widespread accessibility of cloud and AI services today, there is a search for new technologies that are spatially efficient, energy-saving, and computationally time-effective. Additionally, the industry's high dependence on steady support of semiconductor devices was revealed with the 2020 semiconductor chip crisis at the latest[25]. Above all, the tunability, small size and fast spin dynamics of 2D antiferromagnetic semiconductors immediately make them candidates for sensor or data storage applications. Although the motivation for the investigation of 2D magnets can be found in possible technical applications, a physicist's main drive always lies in increasing understanding of fundamental physical relations. Here, magnetic van der Waal materials provide an ideal playground to explore magnetism of reduced dimensions.

The research presented within the framework of this thesis is dedicated to contributing to the exploration of ultrafast (sub-picosecond) dynamics of crystal lattices and spins by using light. The here presented approach ranges from the incoherent demagnetization dynamics in a bulk metal to the coherent dynamics in the 2D-antiferromagnet $FePS_3$, with a primary goal lying in establishing an experimental technique that is capable of capturing these phenomena in microscopic samples of reduced dimensionality.

The approach of this thesis will be as follows:

- In the first chapter, we will discuss the basic physical principles of the here-used methods and sample systems. The chapter contains a basic introduction to ferro- and antiferromagnetism and introduces the general material classes to which $FePS_3$ is assigned. Moreover, an introduction to the detection mechanisms is given.
- The second chapter provides a detailed discussion of the experimental system developed during the thesis framework and introduces the concept of pump-probe spectroscopy. It presents the different subsystems and their integration into the setup.
- First experimental results are obtained from ultrafast demagnetization measurements in a cobalt single crystal. The measurements are performed as

a function of the most striking free experimental parameters of the setup, providing a benchmark for the system's capabilities.

- In the chapter on coherent lattice and spin dynamics in $FePS_3$, we demonstrate a coherent phonon excitation in bulk $FePS_3$, which is closely related to the antiferromagnetic order. The zone-folded phonon mode shows a hybridization with a magnon mode, which is utilized to excite coherent spin dynamics.
- Finally, in the last result chapter on flake $FePS_3$ we will progress with the findings from the bulk $FePS_3$ chapter and apply them to a flake sample of microscopic size. We thus demonstrate the scalability of our experimental approach.
- The last chapter provides a conclusion of the thesis with an outlook on possible future progress on this topic.

1 Theory

This chapter outlines the basic physical concepts that will be part of the investigations of this work, beginning with a description of the long-range magnetic order of the sample systems. A short introduction into $FePS_3$ as a magnetic van der Waals material will be given and the observed magneto-optical effects will be introduced.

1.1 Ferro- and Antiferromagnetism

The study of magnetism at the microscopic level has led to the development of various theoretical models for the description of magnetic interactions and the formation of long-range magnetic order. Here, we will give the basic framework to the models used for ferro- and antiferromagnetism, which will aid in discussing the concepts described in this thesis. Both describe the spontaneous, i.e., without the presence of a magnetic field, formation of a magnetically ordered state. Mainly, we will discuss the idea of the Heisenberg and Ising models for the description of magnetism with localized magnetic moments and the Stoner model describing the ferromagnetic ordering regulated via $3d$ electron bands in Fe, Co and Ni.

Collective magnetism of localized electrons

In the first description, we assume that the magnetic moments are fully localized at their atomic positions. Within the absence of external magnetic fields or magnetic anisotropies, the Hamiltonian for the interaction between neighboring spins S_i is given by the Heisenberg model:

$$H = -2 \sum_{\mathrm{i<j}}^{N} J_{\mathrm{ij}} \mathbf{S_i} \cdot \mathbf{S_j} \,, \tag{1.1}$$

where J_{ij} denotes the coupling constant between $\mathbf{S_i}$ and $\mathbf{S_i}$, given by the exchange integral over the overlapping wavefunctions of the corresponding electrons [26]. The sign of the coupling constant J_{ij} indicates which ordering type is favored in the specific material. For values $J_{\mathrm{ij}} > 0$ the energy of the system is minimized for parallel

ordering of the electron spins, favoring ferromagnetic order, while $J_{ij} < 0$ antiparallel ordering i.e., antiferromagnetic ordering minimizes H. Both cases are illustrated in Figure 1.1. In the presence of an anisotropic exchange, the spin orientations $\mathbf{S_i}$ can be reduced to one dimension $\mathbf{S_i^z}$, reducing the Hamiltonian to an Ising type [27]:

$$H = -2 \sum_{i<j}^{N} J_{ij} S_i^z \cdot S_j^z \,. \tag{1.2}$$

The magnetic anisotropy describes the preference of a specific magnetization direction in a material, termed as the easy axis. Deviations from this direction require energy, defining anisotropy energy as the energy difference between the hard (maximum energy) and easy axes. Often the effect of the anisotropy is introduced as an effective magnetic field H_A oriented parallel to the easy axis. Analogously, the exchange interaction can also be described with an effective exchange field H_{Ex}, acting on each moment. The source of the magnetic anisotropy can be an intrinsic property of the material, as seen in the case of magnetocrystalline anisotropy, where the orbital magnetism couples via the spin-orbit coupling to the magnetic moment of the spins in the lattice. A specimen's shape or external factors such as strain or pressure can induce a magnetic anisotropy as well [27].

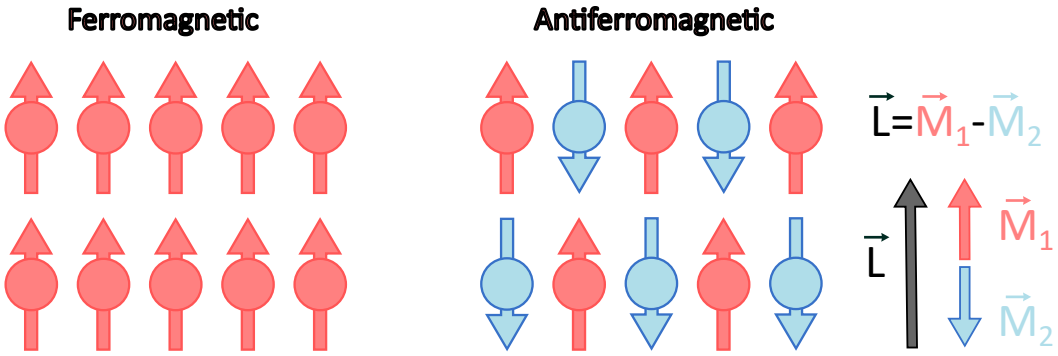

Figure 1.1: Ferromagnetically (left) and antiferromagnetically (right) ordered magnetic moments in an atomic lattice at T = 0 K. The arrows on the far right side illustrate the magnetization of each sublattice, forming the antiferromagnetic order parameter **L**.

Antiferromagnetic ordering can be described with two antiparallel sublattices with magnetizations M_1 and M_2 of parallel aligned magnetic moments. In a fully compensated antiferromagnet, the magnetization of the two sublattices cancel out

on a macroscopic scale to yield zero net magnetization:

$$\mathbf{M}_1 + \mathbf{M}_2 = 0\,. \tag{1.3}$$

The ordering in an antiferromagnet can be described by the antiferromagnetic order parameter $\mathbf{L}$, which is defined as:

$$\mathbf{L} \coloneqq \mathbf{M}_1 - \mathbf{M}_2\,. \tag{1.4}$$

A third possibility, not further discussed, is ferrimagnetism, where the two sublattices $\mathbf{M}_1^{\text{ferri}}$ and $\mathbf{M}_2^{\text{ferri}}$ are aligned antiparallel but, are of different magnitude ($\mathbf{M}_1^{\text{ferri}} + \mathbf{M}_2^{\text{ferri}} \neq 0$).

In addition to the absence of a net magnetization, antiferromagnets exhibit properties that can be appealing from an application point of view. The typical exchange field can lie in the order of 100 T, making them exceptionally resistant against external perturbations and increasing the characteristic frequencies of their spin dynamics, surpassing the of ferromagnets with typical values for H_{A} below 1 T [28]. The ferromagnetic resonance frequency $\omega_{\text{FM}} \approx \gamma H_{\text{A}}$ directly depends on the anisotropy field H_{A} and the gyromagnetic ratio γ, while the antiferromagnetic resonance frequency is increased by a factor of $a\sqrt{H_{\text{ex}}}$, which, due to the high exchange field H_{ex}, intrinsically exceeds the resonance frequency of ferromagnets[28].

For finite temperatures ($\text{T} > 0\,\text{K}$), thermally excited magnons soften the ideal parallel/antiparallel alignment of the magnetic moments, effectively reducing the magnetic order. Above a critical temperature T_{Crit} the thermal fluctuations are too strong to upkeep the long-range magnetic order and a paramagnetic behavior takes over. The critical temperature for ferro- and antiferromagnets is called the Curie temperature (T_C) and the Neel temperature (T_{N}), respectively. The temperature dependence of the saturation magnetization M below the critical temperature can be numerically calculated within the molecular field theory, as exemplarily shown in figure 1.2 [29]. Near the critical temperature, where a second-order phase transition from the magnetically ordered to unordered state occurs, certain magnetization-related properties can exhibit a magnetic critical behavior. Within the Landau description of second-order phase transitions, these properties can be described by a power law. For instance, the saturation magnetization M and specific heat C, in the absence of external fields, are described by the following equations [26, 30, 31]:

$$M(T/T_{Crit}) \propto (1 - T/T_{\text{Crit}})^{\beta} \tag{1.5}$$

$$C(T/T_{Crit}) \propto (1 - T/T_{\text{Crit}})^{-\alpha}\,. \tag{1.6}$$

The critical exponents β and α can differ for different ordering structures (e.g. Heisenberg-, Ising-type...) or the spin dimensionality and thus give insight into

the magnetic structure of the material[30]. Figure 1.4 shows the formation of magnetic moments for the different ordering types. In some materials, the specific heat capacity can show an asymptotic rise near T_{Crit}, which also impacts the magnetization dynamics, leading to critical effects in the characteristic timescales near the transition temperature [32]. The inset of figure 1.2 shows the trends for the typical reduction of magnetic order as a function of the temperature.

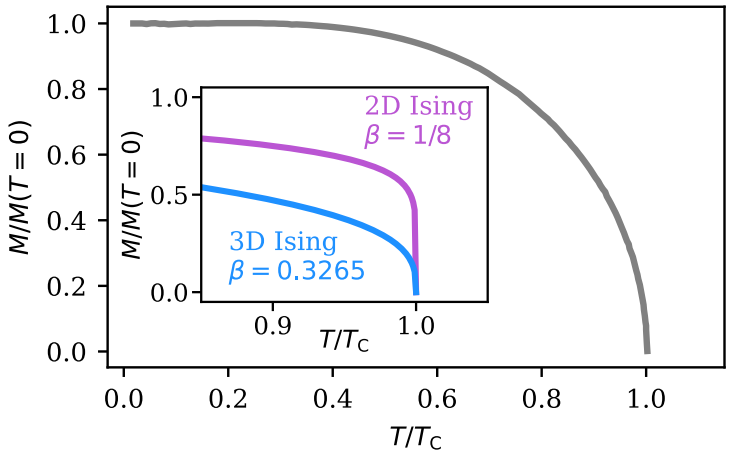

Figure 1.2: Theoretical temperature dependence saturation magnetization, without external magnetic fields, as derived from the molecular field theory (data taken from Ref. [26]). Inset: behavior close to the critical temperature for Ising-type magnets in three (blue) and two (purple) dimensions. The values for β are taken from reference [30]. The magnetization is normalized by the saturation magnetization at $T = 0\,\mathrm{K}$.

Band ferromagnetism

In a metal, the electrons are highly mobile and the assumption of fully localized magnetic moments does not hold for the description of the typical transition metal ferromagnets iron, cobalt and nickel. Generally, the assumption of fully localized electrons at the atomic sites is oversimplified, as it does not allow for a large overlap of the electronic wavefunctions, which is the essence of a strong exchange coupling [31]. Therefore, the general idea of band ferromagnetism within the Stoner model will be presented here.

We turn to a band description of the electronic states and separate each electron band into a spin-up and a spin-down band, as shown in figure 1.3. A net magnetization

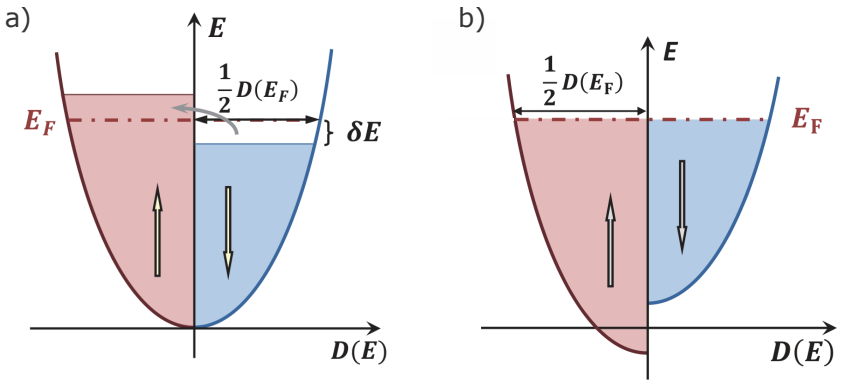

Figure 1.3: Formation of ferromagnetic order in the Stoner model. When a rearrangement of the magnetic moments from the spin down to the spin up band (a) is energetically favored, the two bands split in energy, increasing the population of the spin up band (b). Taken and modified from [33].

.

M will occur when the total occupation of the spin up ($n_\uparrow$) or spin down ($n_\downarrow$) bands exceeds the other [29].

$$|M| = \mu_B(n_\uparrow - n_\downarrow) \tag{1.7}$$

We therefore refer to them as the majority- (here labeled as up) and minority electrons. The bands will only be asymmetrically occupied if the energy levels within a band positioned at the Fermi energy (E_F) are split for up and down electrons, energetically favoring the majority band. For example, the application of an external magnetic field B can split the energy level of the conduction band by twice the Zeeman energy $\Delta E_Z = 2\mu_B B$, allowing the observation of Pauli-paramagnetism [34]. For the spontaneous formation of a ferromagnetic order, however, the splitting of the electron bands has to be an intrinsic property of the material and form without the presence of an external field by reducing the total energy of the system. We assume electrons shift from the minority to the majority band, leading to a change in the number of electrons to:

$$n_{\uparrow,\downarrow} = \frac{1}{2}(n_0 \pm D(E_F)\delta E)\,, \tag{1.8}$$

where n_0 is the total electron number, $D(E)$ the density of states and δE the energy difference between the minority and majority band. The shift of the electrons from the minority band to the majority band would increase the total kinetic energy ΔE_{Kin} of the electrons by

$$\Delta E_{\mathrm{Kin}} = \frac{1}{2}D(E_F)(\delta E)^2\,. \tag{1.9}$$

For the ferromagnetic order to form, this increase of kinetic energy has to be compensated by the exchange interaction, which can favor a parallel alignment, reducing the potential energy E_{pot} in the magnetically ordered state:

$$\Delta E_{\mathrm{tot}} = \Delta E_{\mathrm{kin}} + \Delta E_{\mathrm{pot}} \,, \tag{1.10}$$

with a ferromagnetic order forming, when the condition $\Delta E_{\mathrm{tot}} < 0$ is fullfilled. We assume that the magnetization that builds up by the surplus of majority electrons acts as a mean magnetic field on all electrons [33]. The strength of the mean-field described by U and its reduction of the potential energy is determined by the exchange integral and the electron occupation at the Fermi energy. From this considerations the Stoner criterion

$$UD(E_F) > 1 \tag{1.11}$$

for ferromagnetism in metals can be derived [33]. When fulfilled, this allows for spontaneous long-range ferromagnetic order. It can be seen that a high electron density close to the Fermi energy is beneficial for the ordering. The stoner criterion is fulfilled for the three room temperature $3d$-transition metals iron, cobalt and nickel. The magnetic properties are mostly dominated by the $3d$ electrons, while the s-bands have a low density of states and are mostly neglectable for the ferromagnetic ordering [29].

1.2 Magnetic van der Waals materials

Van der Waals materials are a class of solids consisting of stacked layers with intralayer covalent bonds and inter-layer van der Waals bonds. With a free space called the van der Waals gap between two layers. As a result, they can be easily separated and exfoliated up to the isolation of single layers of the material. Therefore, van der Waal materials are suitable for investigating physical phenomena in the two-dimensional limit. Also, multilayer specimens are often referred to as quasi-two dimensional when their interlayer interaction becomes neglectable [35]. The exfoliation process allows the fabrication and investigation of flake samples with a defined layer number on a substrate or heterostructures consisting of layers of different materials [17]. The stability of these exfoliated materials varies in ambient conditions, with some being stable [36]. In contrast, others degrade rapidly but can be protected by layers of other, air-stable van der Waals materials such as hexagonal boron nitride (hBN) or graphene [37].

Of outstanding interest are van der Waals materials, which show a formation of long-range magnetic order. Already derived in the 1960s, the Hohenberg-Mermin-Wagner (HMW) theory states that in a fully isotropic system, neither ferro- nor

antiferromagnetism can form in a system of one or two dimensions. At finite temperatures (T>0), thermal fluctuations are supposed to suppress the ordering[38]. Therefore, the exchange coupling $\mathbf{J_{ij}}$ as the only interaction influencing the magnetic moments, as described in the ideal isotropic Heisenberg model (see Eq.(1.2)), can not by itself maintain long-range magnetic order. Magnetic ordering is achievable only when combined with an additional contribution to the Hamiltonian, such as magnetocrystalline anisotropy. A simple, generalized description for a Hamiltonian, with an anisotropy contribution, can be given by:

$$H = -\frac{1}{2}\sum_{i,j}\left(J_{i,j}\mathrm{S_i}\cdot\mathrm{S_j} + BS_i^zS_j^z\right) - \sum_i A(S_{iz})^2 \tag{1.12}$$

where the B represents the anisotropy in the exchange interaction along the z-direction and A is a single-ion anisotropy term, aligning the spins along the z-direction. For $B \approx 0$ and $A \approx 0$ (Heisenberg model), all spin directions are possible, which corresponds to a spin-dimensionality of n=3. In the Ising model ($A \to \infty$) the magnetic moments align along a strong easy-axis (n=1) and in the XY-model ($A \to -\infty$) within an easy plane (n=2)[17]. Although the HMW theorem states that the existence of some form of magnetic anisotropy is conditional on stabilizing the magnetic order in two dimensions, the existence of a magnetically ordered state down to the monolayer has been demonstrated for different materials[19, 39]. Moreover, it was shown recently that the HMW theorem can already be lifted in a 2D system when the assumption of infinite crystal expansion is reduced to finite sizes [40] and ordered states in few- or monolayers systems of low anisotropy systems were found [41, 42]. Despite the limitations of the HMW theorem, it holds that the anisotropy in two-dimensional or quasi-two-dimensional magnetic systems plays a key role in the magnetic behavior, which can cause physical and magnetic properties to drastically change in the transition from the multi- to the few and single layer.

Without the presence of a strong anisotropy, in many cases, the critical temperature is reduced, as the total layer number is reduced[17]. The number of layers may also influence the magnetic order. For example, in the ferromagnet CrI_3, only the bi-layer exhibits an antiferromagnetic ordering, while the higher multilayer specimens and even the single layer display Ising-type-ferromagnetic properties [43]. In other materials, the introduction of a small anisotropy via the application of a gate voltage [44] or an external magnetic field [41] can increase the transition temperature, allowing the control of the long-range magnetic order via electric or magnetic fields.

The magnetic phenomena in atomically thin van der Waals materials can be probed optically in the form of Raman spectroscopy [20] or other magneto-optical effects [45], often based on dichroism[46]. For magnetic linear dichroism, it was demonstrated in

$FePS_3$ that the creation of optical cavities from the matched combination of sample thickness and probing-light wavelength can drastically increase the magneto-optical contrast [47]. Detecting the optical spectrum can also be suitable for measuring the thickness of flakes on a substrate via optical contrast spectroscopy and is often combined with atomic force microscopy. Additionally, magneto-transport measurement [48] and electrical photo response[36] have been performed.

Transition metal phosphorus trisulfides - MPS_3

A subgroup of the magnetic van der Waal materials are the transition metal phosphorus trisulfides or short MPS_3 (M=transition metal). All members of the MPS3 group are antiferromagnetic semiconductors with a Néel temperature above the liquid nitrogen temperature. The MPS_3 group spans a wide range of band gap energies (1.5 eV-3.0 eV) and includes different spin-dimensionalities. Table 1.1 lists the physical features of the predominantly investigated MPS_3-family members.

Table 1.1: Important properties of some members of the MPS3-family.

	$FePS_3$	$NiPS_3$	$MnPS_3$
Néel temperature	118 K [39]	155 K [49]	78 K [49]
Band-gap	1.5 eV [50]	1.6 eV[51]	3.0 eV[52]
Magnetic anisotropy [53]	Ising	XY	Heisenberg
Interlayer coupling [53]	AFM	FM	FM

All MPS_3 members crystallize in a monoclinic crystal structure with a c2/m space group. The transition metal ions carry the magnetic moments and order within the *ab* plane in a hexagon, known as a honeycomb structure. Figure 1.4 displays the structure of a MPS_3 crystal. In the center of the transition metal hexagons, P_2S_6 clusters are covalent bond to the metal-ions, mediating the exchange interaction[53].

$NiPS_3$ has an in-plane spin orientation (see Fig. 1.5), with a ferromagnetic interlayer coupling. It was shown that the low anisotropy in $NiPS_3$ leads to a reduction of T_N with a reduced number of layers until the magnetization fully quenches in the monolayer [20]. A trigonal distortion by the NiS_6 octahedra leads to a crystal-field splitting of the 3*d*-states. The spin-forbidden *d*-*d* transition between the crystal field split states can be used to optically excite coherent magnon modes [55]

The magnetic moments of $MnPS_3$ do not fully align with the trigonal axis of the crystal, simultaneously breaking space-inversion and time-reversal symmetry, which makes the magneto-electrical effect symmetry allowed [56]. Here, the magnetic order is maintained even in the monolayer [19].

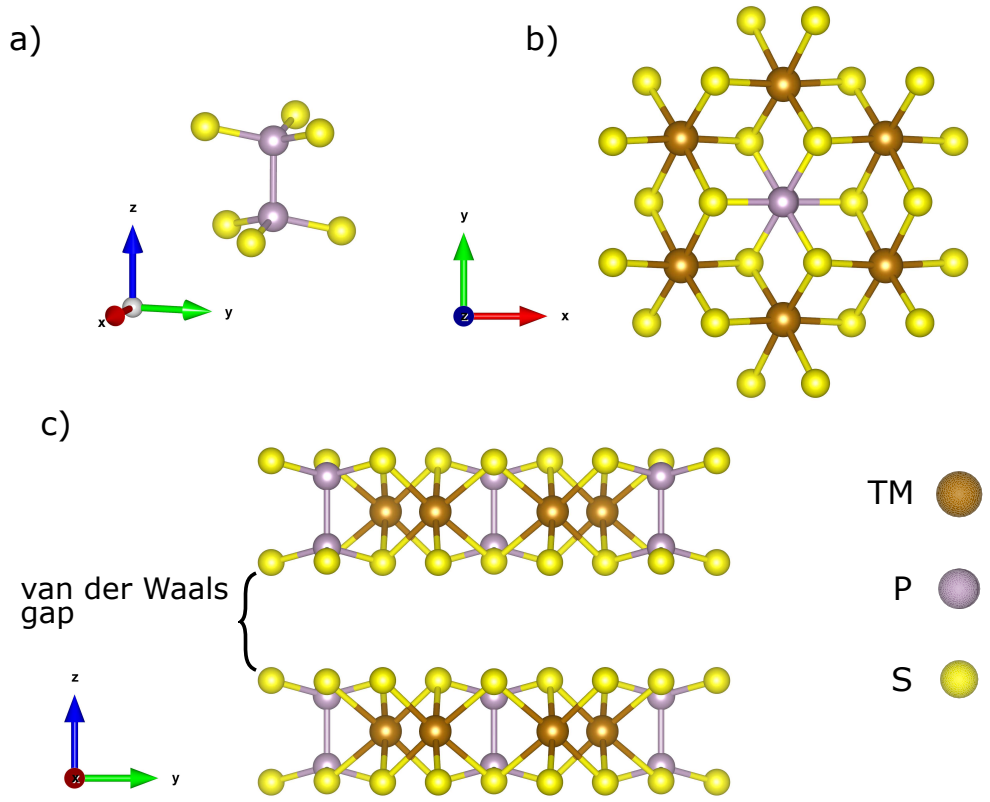

Figure 1.4: Crystal strucure of MPS_3. a) $P_2S_6^{4-}$-anion that is centered in the honeycomb structure formed by the transition metals. b) Top view on a single layer MPS_3. c) Two stacked layers hold together via the van der Waals force. The illustrations were created with the software VESTA[54].

$FePS_3$, which will be investigated within the framework of this thesis, has a strong out-of-plane magnetic anisotropy, with a magnetization very stable towards a reduction in dimensionality, as it maintains its long-range magnetic order, even in a monolayer form[39, 57] [20]. Also, its critical temperature stays virtually unchanged down to the monlayer[39]. In its magnetically ordered phase, below the Néel-temperature of approximately 120 K [39, 58] the magnetic moments of $FePS_3$, carried by the Fe^{2+} ions form a zigzag pattern within the layers. This pattern creates a stripe-like formation of the magnetic moments aligned parallel or respectively antiparallel to the out-of-plane axis of the material[35]. The time-resolved experimental investigation of the material can be found in chapter 4 and 5.

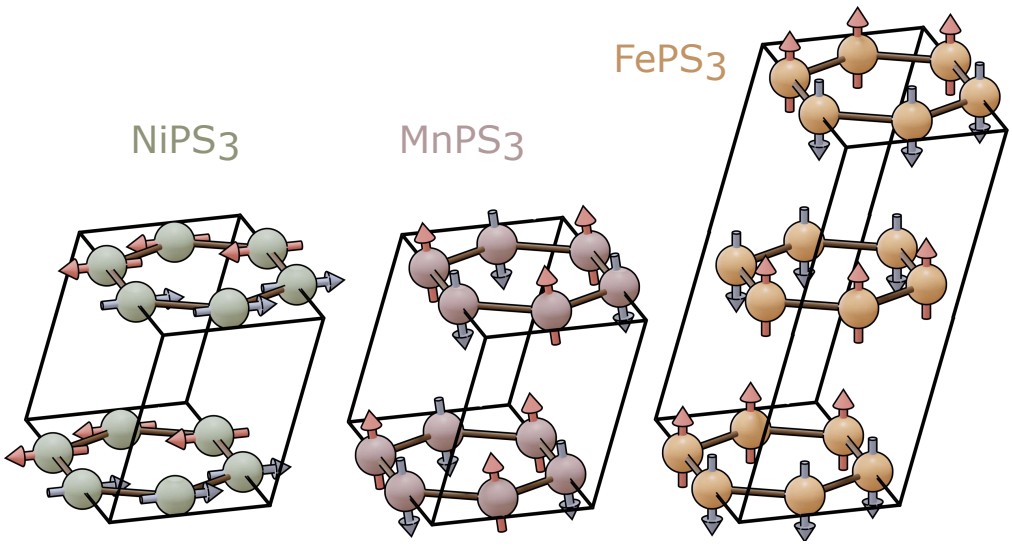

Figure 1.5: The transistion metal ions and orientation of the magnetic moments within the magnetic unit cells of $NiPS_3$ (XY), $MnPS_3$ (Heisenberg) and $FePS_3$ (Ising). The antiferromagnetic interlayer ordering in $FePS_3$ doubles the size of its magnetic unit cell along the z-axis. Inspired from Ref. [53].

1.3 Magneto-optical effects

The interface between our experimental apparatus and the sample properties is the optical and the magneto-optical effects of the samples on the reflected or transmitted probe beam. The properties of the light can be altered by the sample in terms of light intensity, polarization and ellipticity via various effects. Here, we will give an idea of the two cases that are observed within the presented experiments: the magneto-optical Kerr effect (MOKE) and the magnetic linear dichroism (MLD). In general, magneto-optics describes the interaction between light and magnetism. Typically, the observed effects are a result of the splitting of energy levels due to the Zeemann effect and spin-orbit interaction, resulting in a variation of the optical anisotropy, depending on the light polarization or helicity [59].

Magneto-optical Kerr effect

Among the various magneto-optical effects, the Kerr effect stands out due to its widespread applications as a probe for magnetization. It describes the rotation and induced ellipticity of the polarization plane of linearly polarized light when it interacts with a magnetized material. In particular, the here mentioned variation is the polar Kerr effect, which applies to magnetization orientation perpendicular to the sample plane and in the propagation direction of the light.

The type of effect that the probing beam undergoes after the interaction with the sample surface and/or its body is defined by the dielectric permittivity tensor $\hat{\epsilon}$, which by itself may be altered by the magnetization and the crystal-lattice. The interaction between the electric field of the light and the material is then described by the electric displacement

$$\mathbf{D} = \epsilon_0 \hat{\epsilon} \mathbf{E} \,. \tag{1.13}$$

with the vacuum permittivity $\epsilon_0$and each matrix-element having a complex value.

We first consider an optically anisotropic non-magnetized medium without any external fields. Here the dielectric tensor is purely diagonal:

$$\hat{\epsilon}(M_z = 0) = \begin{pmatrix} \epsilon_{11} & 0 & 0 \\ 0 & \epsilon_{22} & 0 \\ 0 & 0 & \epsilon_{33} \end{pmatrix} \tag{1.14}$$

The presence of a magnetic field, magnetizing the crystal in the direction of the light propagation (here: in z-direction), introduces a magnetization dependence of the matrix elements, also at the off-diagonal positions [60]:

$$\hat{\epsilon}(M_z) = \begin{pmatrix} \epsilon_{xx}(M_z) & \epsilon_{xy}(M_z) & 0 \\ -\epsilon_{xy}(M_z) & \epsilon_{yy}(M_z) & 0 \\ 0 & 0 & \epsilon_{zz}(M_z) \end{pmatrix} \tag{1.15}$$

The diagonal elements are even functions of the magnetization M_z, while the off-diagonal elements are odd functions of M_z.

In a classical description of electron motion, we can see that the electrons are driven by the electric field of the light and circularly polarised light will cause the electrons in the medium to move in a circular motion. In the presence of a magnetic field, either externally applied or as an effective field with contributions from the magnetization of the medium, the radii of the moving electrons are increased or decreased for left or right circular motion by the Lorentz force. As the electron motions are described by the dielectric tensor, this anisotropy is reflected in the non-diagonal elements of $\hat{\epsilon}$ [61].

Any linear polarized light wave

$$\mathbf{E}(\mathbf{r},\mathbf{t}) = E_0 \mathrm{e}^{-i(\omega t - \mathbf{kr})} = \mathbf{E}_+(\mathbf{r},t) + \mathbf{E}_-(\mathbf{r},t) \tag{1.16}$$

can be considered as the superposition of two circular polarized components of opposite helicity($\mathbf{E}_+(\mathbf{r},\mathbf{t}), \mathbf{E}_-(\mathbf{r},\mathbf{t})$) with amplitudes of $E_0/2$ [62]. The eigenvalues of $\hat{\epsilon}(M_z)$ can be calculated as

$$N_\pm = \epsilon_{xx} \pm \mathrm{i}\epsilon_{xy} \tag{1.17}$$

and correspond to the complex refractive index for left (-) and right (+) circularly polarised light. It can be shown that the difference in phase and reflectivity for the two components $\mathbf{E}_+(\mathbf{r},t)$ and $\mathbf{E}_-(\mathbf{r},t)$ induces a change in polarization θ_K and ellipticity η_K of the reflected light [60]. The magnitude of polarization and ellipticity change is given by the complex Kerr angle:

$$\Phi_K = -\frac{\epsilon_{xy}}{(1-\epsilon_{xx})\sqrt{\epsilon_{xx}}} \tag{1.18}$$

With the real and imaginary part corresponding to the polarization rotation (circular birefringence) and induced ellipticity (circular dichroism):

$$\theta_K = \mathrm{Re}(\Phi_K) \tag{1.19}$$

$$\eta_K = \mathrm{Im}(\Phi_K)\,. \tag{1.20}$$

They can be seen as the results of circular birefringence and circular dichroism effects, respectively [63]. Figure 1.6 presents a schematic of the two values θ_K and η_K.

Magnetic linear dichroism

The Kerr effect is well suited for detecting the magnetic state in ferromagnets. In the case of fully compensated antiferromagnets, no net magnetization is present and therefore the Kerr effect, except for some special cases[64, 65], is not a generally applicable detection method. Here, second-order effects, sensitive to $\mathbf{L}^2$ become relevant in the dielectric tensor and can be observed as a magnetic linear birefringence or linear magnetic dichroism[9, 46, 66]. In other cases, the magnetization dynamics can induce an effective magnetization, which can be detected analogously to the Kerr effect[67].

We will shortly elaborate on the second important magneto-optical effect observed in the presented work: magnetic linear dichroism. Linear birefringence or dichroism refers to an optical anisotropy that causes a material to exhibit different refraction

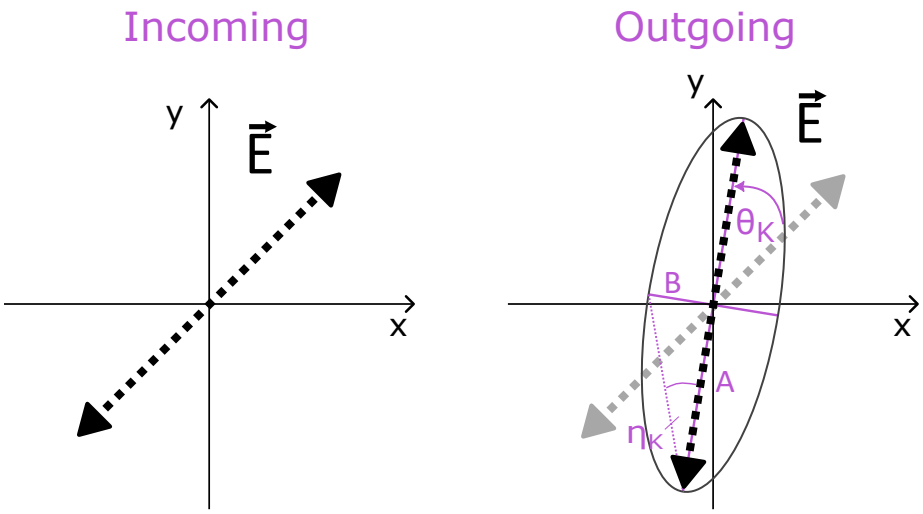

Figure 1.6: Sketch illustrating the Kerr effect on a linearly polarized light beam. On the left, the incoming light beam is linearly polarized. On the right, after interaction with a medium, the beam exhibits Kerr rotation, rotating its polarization plane by the angle θ_{K} and becoming elliptically polarized. The elliptical polarization is characterized by the major axis A and the minor axis B.

coefficients for different polarization angles of linearly polarized light. The complex index of refraction $\tilde{n}$ can be described as:

$$\tilde{n} = n + \mathrm{i}k\,. \tag{1.21}$$

The real part n, also referred to as the refractive index, is descriptive for the refraction at the transmission between two media, the phase velocity and thus the dispersion of light. Polarization-dependent differences in n are called birefringence, while the extinction coefficient k is descriptive of the absorption in a medium and thus for the dichroism. In the case of circular dichroism, the light absorption depends on its helicity ($k_+ \neq k_-$), while for linear dichroism, the absorption coefficients of the perpendicular light components differ ($k_\parallel \neq k_\perp$).

To quantify the optical anisotropy between two perpendicular axes and their respective reflectivity R we use the linear dichroism value:

$$LD = \frac{R_\parallel - R_\perp}{R_\parallel + R_\perp}\,. \tag{1.22}$$

Depending on the strength of the anisotropy, an incoming beam, polarized at an angle ϕ relative to the anisotropy axis, will undergo a polarization rotation of

Θ_{LD} [46]:

$$\Theta_{\mathrm{LD}} \approx \frac{LD}{2} \sin 2\phi \,. \tag{1.23}$$

Figure 1.7 shows an example of light polarized 45° towards the optical anisotropy axes and experiencing linear dichroism. After interacting with the medium, its polarization plane is effectively rotated.

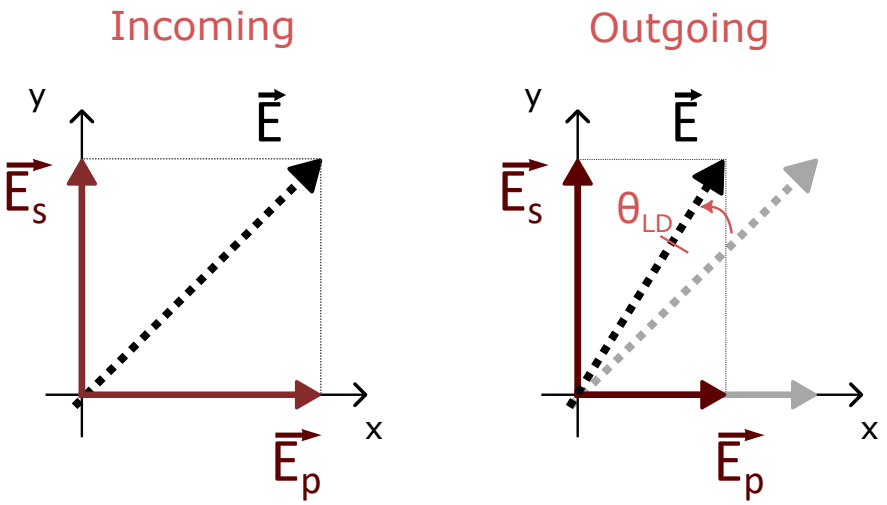

Figure 1.7: Schematic of the magnetic linear dichroism effect. The absorption for the p- and s-polarized electric field components E_{s} and E_{p} is different in magnitude. On the right example, after passing through or being reflected by a medium, only the p-component is partially absorbed, leading to a rotation θ_{LD} of the total polarization plane.

2 Experimental setup[1]

A significant portion of the work related to this thesis was dedicated to establishing the time-resolved magneto-optical setup, which is used for the experiments of the subsequent chapters. In the present chapter, the setup and instruments will be discussed in detail and the general experimental concepts of the employed methods will be explained. It can be noted that a part of the setup has also been addressed in another thesis [68]. Here, we will go into greater detail about every subsystem and thoroughly discuss the full scope of the experiment. Furthermore, this chapter can also act as a primer for future students seeking to familiarize themselves with the experiment.

After introducing the concept of pump-probe spectroscopy, we will begin with a general description of the optical setup and its layout before the single components are described.

2.1 Pump-probe Spectroscopy

Optical pump-probe spectroscopy is a time-resolved method to investigate light-induced dynamical phenomena in matter. It can surpass the time resolution of purely electronic detection and is a common method for investigating sub-picosecond phenomena. Two pulsed light sources, typically lasers, illuminate the sample at a tunable time delay Δt. One pulse, labeled as the pump, serves as a source of excitation, while the second pulse, the probe, is meant to detect the current state of the sample. Whereby the probe pulse should be set low enough in intensity that a probe-induced perturbation of the studied system can be neglected. Figure 2.1 presents a schematic image of the method.

The pump induces dynamic processes in the sample that can span a wide range of phenomena, including electronic transitions, the quench or switching of magnetization and the excitation of quasiparticles [2, 9, 55, 69]. By varying the time delay Δt between the two pulses, it is possible to resolve the pump-induced excitation and

[1] Parts of this chapter are published in "Wide Spectral Range Ultrafast Pump–Probe Magneto-Optical Spectrometer at Low Temperature, High-Magnetic and Electric Fields" In: *Review of Scientific Instruments* 91.11 (2020)

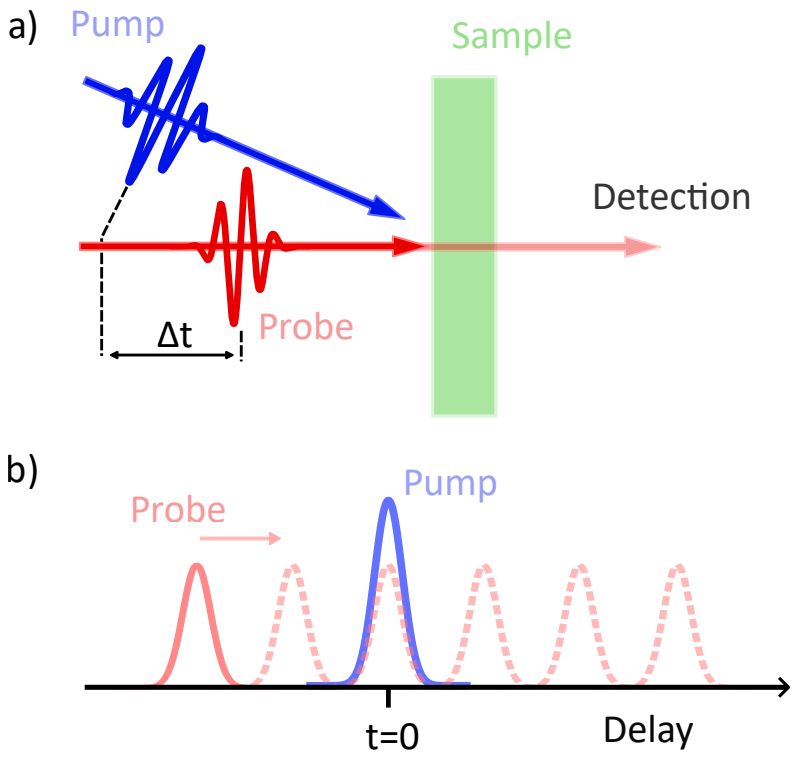

Figure 2.1: a) Schematic of a pump-probe measurement in transmission. The pump beam (blue) excites the sample and the probe beam (red) detects the pump-induced changes in the sample. b) The time evolution of the light-induced dynamics are detected by varying the relative time delay between the pump and probe pulse.

induced dynamics in time. Ideally, for the investigation of non-switching phenomena, the sample returns into its ground state before the next pump pulse arrives. With this type of detection, the time resolution is not limited by the speed of the used electronics, which lies in the order of nanoseconds for typical photodiodes[70]. Instead, the time resolution depends on the pulse duration of the two laser pulses and their convolution. The probe beam is reflected from the surface or transmitted through the sample and is afterward guided to a detection scheme.

In our case, the signal S is given by changes in the polarization, intensity or ellipticity of the probe. By introducing an amplitude modulation to the pump-induced transient signal is calculated by

$$\Delta S = S_{\mathrm{On}} - S_{\mathrm{Off}} \tag{2.1}$$

where S_{On} describes the signal with pump illumination and S_{Off} is the signal with the pump pulse fully blocked.

2.2 System Layout

The time-resolved magneto-optical setup relies on a tabletop layout powered by a femtosecond pulsed laser source with two optical parametric amplifiers (OPA), allowing tunable photon energies for the pump and the probe beam. The laser system uses a custom-made amplitude modulation by an electro-optical modulator (EOM), blocking every second pump pulse. It is described in detail in section 2.3. A schematic overview of the setup is shown in Figure 2.2. After the laser system, a mechanically

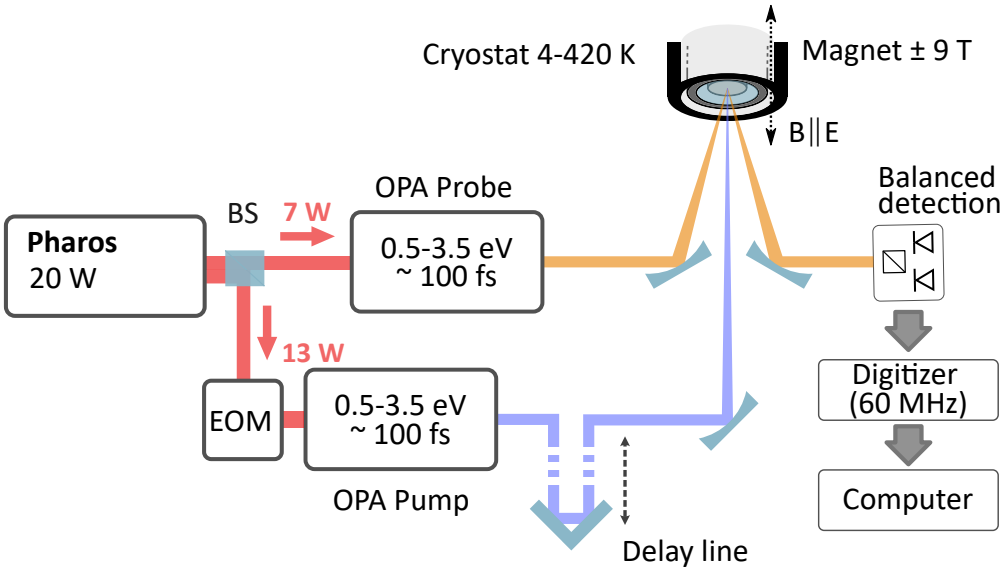

Figure 2.2: Schematic of the total optical setup in a non-collinear reflective geometry. The setup is convertible it into transmission geometry. Furthermore, focusing the beams down to a few micrometers is possible using a microscope objective.

and computer-controlled delay line (DL) in the pump beam path provides the time delay between the pump and the probe pulses. The linear motor of the delay line (*Newport DL325*) can move in step sizes as small as 75 nm. When approaching absolute positions, as is the case with multi-scan pump-probe measurements, we observe a positional accuracy of approximately 4 µm, corresponding to 2.5 fs for a single DL pass and 5 fs for passing the delay line twice, at it is in the current configuration. Spherical mirrors focus the pump and the probe beam on the sample, while the mirror focusing the pump is controlled via piezoelectric motors to ensure precise spatial overlap of the pump and probe beam. The use of spherical mirrors avoids spectral changes in the focus position and simplifies the integration of the

wide spectral bandwidth of the OPAs into the experiment. The sample is mounted within a flow cryostat capable of cooling down to 4 K with liquid helium and heating up to 420 K and a superconduction magnet with a maximum field of $\mu_0 H = \pm 9$ T parallel to the light propagation direction (out of plane). After transmission or reflection from the sample, the probe is recollimated and guided to the balanced detection scheme, where the polarization rotation and light intensity is detected. A high-frequency data acquisition card (*Spectrum Instrumentation M2.4964*) operating at 60 MHz detects the analog signal from the detector, digitizes it and transfers it to the computer.

We can precisely monitor the pulse energy per unit area (fluence) by using a *Ophir Spiricon* laserbeam profiler with a pixel size of 4 µm. By placing a mirror between the focusing optics and the sample surface, the light is directed to the position of the beam profiler, which is placed at the distance of the focal length. An example beam profile in the focus position is shown in figure 2.3. An attenuator combination consisting of a broadband half-waveplate and a Glan polarizer in each line regulates the laser power to the desired value in accordance with the detected focus size. In

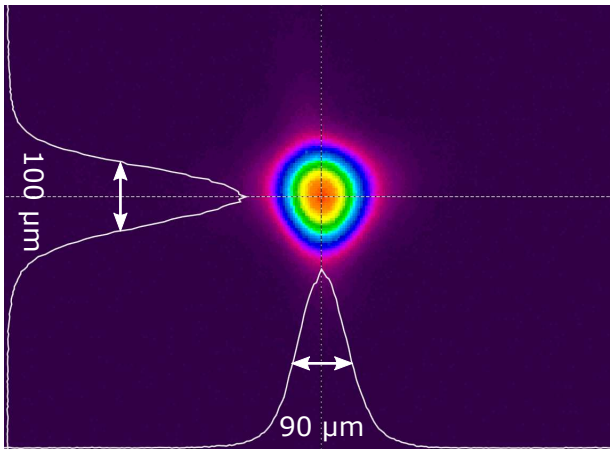

Figure 2.3: Profile of the beam in the focus position. The wavelength is set to 1550 nm and a spherical mirror with a focal distance of 50 cm is employed. The marked distance in the profiles projected on the vertical and horizontal axis corresponds to the full width at half maximum of the beam intensity. Adapted from Ref.[6].

the following, we will define the fluence F as the energy per pulse per illumination area. The illumination area A is approximated by the area covered within the range

of the full width at half maximum (FWHM) of the beam intensity profile:

$$F = \frac{P}{f_{\mathrm{rep}} \cdot A_{\mathrm{FWHM}}} \,. \tag{2.2}$$

The average laser power is given by P and the repetition rate by f_{rep}.

2.3 Laser system

The light source is the most fundamental element in the experiment. Its specifications will determine the time resolution and range of excitable and detectable physical phenomena. The here presented system shall provide a wide spectral range for the pump and the probe beam, while being capable to detect terahertz dynamics at a high sensitivity. A high repetition and modulation rate can increase sensitivity, reducing $1/f$-noise and increasing the number of statistics.

The laser system is a custom-built setup supplied by the company *Light Conversion* (*LC*), able to emit femtosecond light pulses with widely tunable photon energies. The main light source is a single-unit pulsed laser (*LC Pharos*), with Yb:KGW (ytterbium-doped potassium gadolinium tungstate) as an active medium. It has an average power output of 20 W at variable repetition rates, tunable from single-shot up to 1 MHz. The center wavelength of the laser lies at 1030 nm with a pulse duration of 300 fs. The 20 W output of the laser is split into two parts, each pumping one Optical parametric amplifier (OPA, *LC Orpheus-F*). One with a power of 13 W seeding the pump OPA and the other one with an output power of 7 W seeding the probe OPA. A schematic of the laser systems layout can be found in figure 2.2. In between the pump OPA and the Pharos laser a Pockels cell driven electro-optical modulator (EOM) functions as a pulse picker. The EOM is triggered by a TTL signal emitted by the laser in a frequency of an integer fraction n of the repetition rate, effectively only transmitting every n-th pulse. In the standard operation, every second pulse is blocked, modulating the pump at 50 % of the repetition rate.

In all of the here-mentioned measurements performed on the setup, the repetition rate is set to 200 kHz. A change in the rate of typically more than ten percent will require realignment of the OPAs, as the pulse energy changes when the repetition rate is tuned at a constant output power. This need arises due to the OPAs' sensitivity to the pulse energy, which can modify the efficiency of numerous nonlinear effects within the optical crystals [5, 71]. Additionally, there is a risk of exceeding the damage threshold for the optics of the devices, which are exposed to focused light.

Figure 2.4 shows a simplified layout of the OPAs and the energy scheme of the processes within. The OPA is an optical device that utilizes higher-order optical

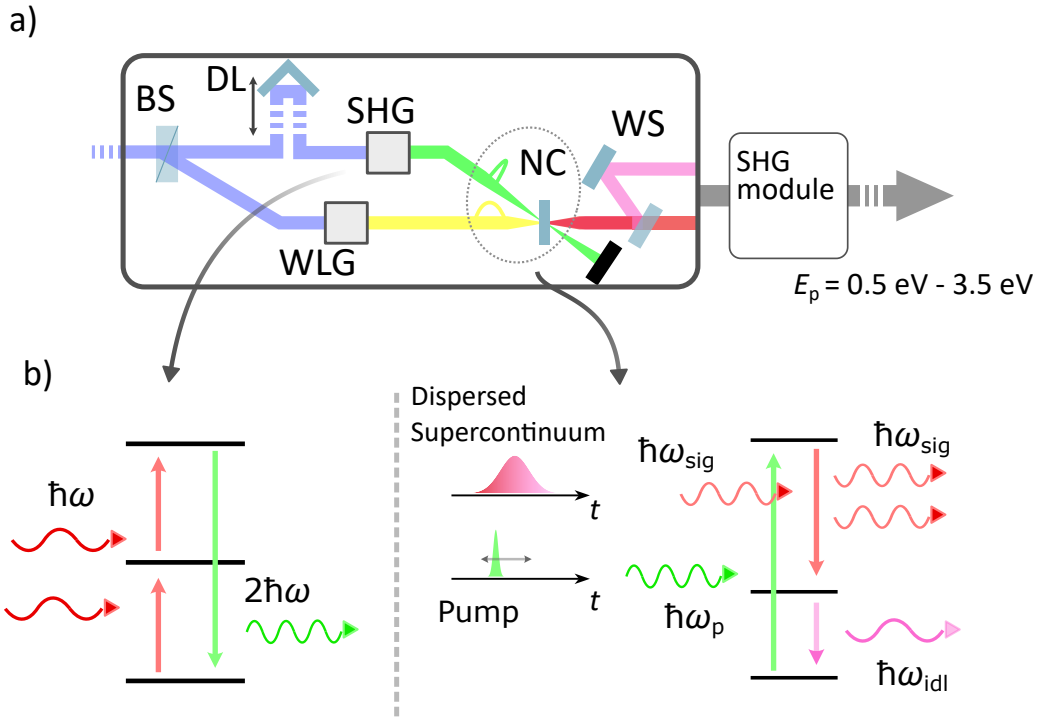

Figure 2.4: a) Simplified layout of the OPA in combination with the SHG module. The following apprevations are used: BS (Beamsplitter), DL (Delay line), SHG (second harmonic generation), nonlinaer crystal (NC) and WL (wavelength separator). b) Energy scheme of the basic interactions inside the OPA - the second harmonic generation (left) and apitcal parametric amplification (right).

effects to tune the photon energy of a pulsed pump laser. The main mechanism is the optical parametric amplification, where a high photon energy pump with the energy $\hbar\omega_{\mathrm{Pump}}$ excites a virtual state in a nonlinear crystal. A second light pulse, labeled as signal, with a photon energy of $\hbar\omega_{\mathrm{Signal}} < \hbar\omega_{\mathrm{Pump}}$ induces the stimulated emission of photons at the frequencies $\hbar\omega_{\mathrm{Signal}}$ and $\hbar\omega_{\mathrm{Idler}}$. Thus, the energy of the pump light is converted into energy for amplifying a light pulse of lower energy, labeled as the signal, and into energy for generating a second pulse, labeled as idler. For the three photon energies the condition

$$\hbar\omega_{\mathrm{Pump}} = \hbar\omega_{\mathrm{Signal}} + \hbar\omega_{\mathrm{Idler}} \tag{2.3}$$

for differential frequency generation holds. Additionally, the phase-matching condition for the light wavevectors

$$\Delta\vec{k} = \vec{k}_{\mathrm{Pump}} - \vec{k}_{\mathrm{Signal}} - \vec{k}_{\mathrm{Idler}} = 0 \tag{2.4}$$

has to be satisfied [5, 71].

The LC Orpheus-F is designed to cover a spectrum from the near UV to the near-infrared, which was technically realized as follows: The initial 1030 nm light of the Pharos laser is split into two components. One component generates the second harmonic of the 1030 nm laser, which will serve as the pump, while the residual of the 1030 nm light is filtered out. The other component is used for white light generation. The supercontinuum is transmitted through a dispersive medium and focussed on a nonlinear crystal together with the pump. A mechanical delay line sets the relative delay between the pump and the dispersed white light, allowing one to choose a specific photon energy to serve as the signal. In the crystal, the optical parametric amplification occurs, amplifying the signal and generating the idler. The following optics include a dichroic mirror reflecting the 515 nm pump into a water-cooled beam dump and two more pairs of dichroic mirrors for selecting either the signal or idler, while the other beam is blocked. In the following, the beam is compressed by a pair of prisms to pulse durations of 100 fs or less. An additional second harmonic generation module after the OPAs can be deployed, turning a nonlinear crystal into the focus position of a telescope, doubling the signal and idler frequency and increasing the total range of tunable photon energies to 0.5 eV to 3.5 eV.

2.4 Balanced detection

Balanced photodetection is an optimal tool for sensing the polarization rotation encountered in magneto-optical pump-probe experiments. The reflected or transmitted probe beam passes through a Wollaston prism and is split into its s- and p-polarized components E_s and E_p. Each component is then focused on one of the diodes of a balanced photodetector (see Fig. 2.5 a)).

The main idea of a balanced photodetector is to amplify a signal proportional to the difference in intensity between two light beams. Thus, common noise from the two beams is reduced and a signal, highly sensitive to relative intensity differences, is returned. A typical scheme can consist of two matched in-series connected photodiodes, with a reverse bias voltage applied, as shown in figure 2.5 b). At the junction between the two diodes (labeled as A and B), a transimpedance amplifier converts the difference of the two photocurrents I_Diff into a voltage:

$$U_\mathrm{Diff} = A(E_\mathrm{Ph})\,(I_\mathrm{A} - I_\mathrm{B}) \tag{2.5}$$

The current-to-voltage conversion and possible additional amplification stages are given by the factor A. Additionally, it should be noted that the photocurrent is

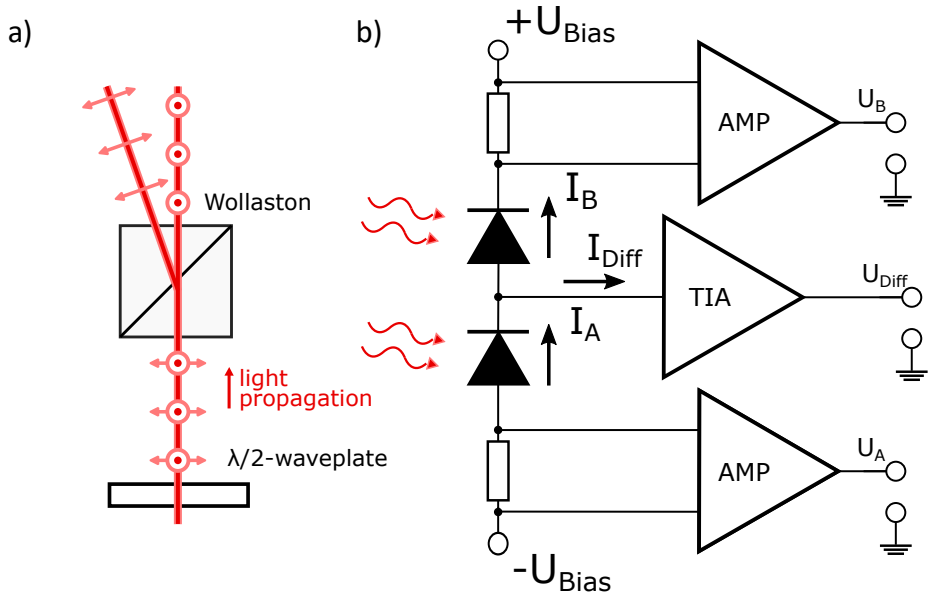

Figure 2.5: a) The Wollaston prism splits the incoming probe beam into its s- and p-components. Both components are of equal intensity in the initial position of operation - the balanced position. b) Typical schematic of the electronic circuit in a balanced photodetector. The active area of the photodiodes is illuminated to generate a photocurrent and the current difference is amplified electronically. In this example, a voltage proportional to the single-diode currents is generated.

sensitive to the probe photon energy of the incident light. Transimpedance amplifiers are notable for the low (virtually zero) input resistance and absence of distortions to the light-induced currents. Many balanced photodetectors have the additional option to monitor the intensities on the single diodes. For this purpose, additional amplification stages can be used to amplify the voltage at the resistors coupled in series to the diodes.

A half-wave plate in front of the Wollaston prism sets the detection into the balanced condition, where $E_\mathrm{s} = E_\mathrm{p}$. By assuming a rotation of the polarization plane by the angle θ induced by the reflection or transmission of the probe beam away from the balanced position, for example, by a pump-induced effect, we receive the two electric field components:

$$E_\mathrm{s} = E \sin(\pi/4 + \theta) \tag{2.6}$$

$$E_\mathrm{p} = E \cos(\pi/4 + \theta)\ . \tag{2.7}$$

The photocurrent on the two diodes is proportional to the light intensity, i.e. $\propto E^2$. Therefore, the difference signal of the photoreceiver is proportional to the difference of the photocurrents of both photodiodes and thus:

$$\begin{aligned} U_{\mathrm{A-B}} \propto & E^2 \sin^2(\pi/4+\theta) - E^2 \cos^2(\pi/4+\theta) \\ = & E^2 \sin(2\theta) \\ \approx & 2E^2\theta = 2I\theta\,. \end{aligned} \tag{2.8}$$

It can be seen that the signal is proportional to the total laser intensity and the light polarization θ. The small-angle approximation is justified, as the expected pump-induced rotation of the laser polarization typically does not exceed the one-degree range[46]. Depending on the design of the balanced photoreceiver, it is possible to output a signal proportional to the single photodiodes' photocurrents simultaneously to the difference signal. With a simultaneous detection of the total light intensity and the balanced signal, it is possible to normalize the rotation signal and convert it into the corresponding polarization rotation, assuming a calibration was performed. In other configurations, the benefits of balanced detection could also be used to detect other light properties. By placing a quarter-waveplate in the correct rotation before the Wollaston prism, the light-ellipticity will be converted into a rotation value and can thus be measured[9, 72]. For reflectivity or transmissivity measurements, it is possible to split the beam into a reference beam and a detection beam. Both beams illuminate one diode each, while only the detection beam passes the sample. In this case, the balancing can be done by placing a variable attenuator in one of the beams [73].

2.5 Data acquisition

The detection in the magneto-optical setup relies on the use of a high frequency digitizer card (DAC, Spectrum Instrumentation M2i), that is connected to the balanced photodetector and triggered by the laser, performing a single pulse acquisition. Another key element that is adjusted to the use with a DAC is the pump modulation via the EOM, blocking every second pulse. The combination of these two elements within an optical setup has proven to be a highly versatile detection method that simultaneously can compete with the performance of a lock-in amplifier [74].

Figure 2.6 shows a schematic of the total detection system as it is implemented in the setup. The DAC receives a TTL trigger from the laser and starts the data acquisition after a fixed time delay. The DAC detects four channels for each incoming probe

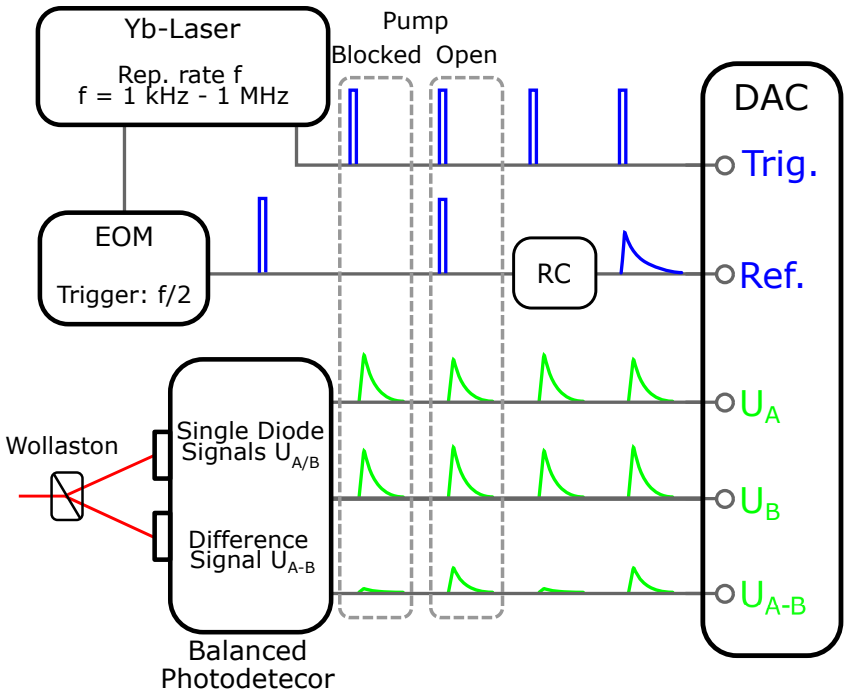

Figure 2.6: Schematic of the data acquisition at a 50 % pump amplitude-modulation. The card is triggered by the laser trigger and records the three channels (U_{A}, U_{B}, $U_{\mathrm{A\text{-}B}}$) of the balanced photodetector and the reference channel. Based on the presence of a reference signal, the data will be sorted into groups of pump-induced and non-pump-induced signals. Taken from Ref.[24].

pulse: The difference signal $U_{\mathrm{A\text{-}B}}$ from the balanced detector, together with the two single diode signals U_{A} and U_{B} and a reference signal emitted from the EOM.

The sampling rate of 60 MHz is able to fully resolve the electronic response of the detector at a resolution of 16 Bit (see inset of Fig. 2.7). However, the acquisition only takes place within the region of the highest signal-to-noise (S/N) ratio in the electronic pulse emitted by the detector. This way, the acquired data points are kept to a minimum and the calculation time is reduced while a high signal quality is achieved. According to eq.2.8 the difference signal $U_{\mathrm{A\text{-}B}}$ is proportional to the rotational angle θ and the probe intensity. We can therefore use the sum of the single diode channels $U_{\mathrm{A}} + U_{\mathrm{B}}$, to normalize $U_{\mathrm{A\text{-}B}}$ and receive a quantity independent of the probe power and proportional to the rotation angle:

$$\theta \propto \frac{U_{\mathrm{A\text{-}B}}}{U_{\mathrm{A}} + U_{\mathrm{B}}} \,. \tag{2.9}$$

Now, this conversion can be used to estimate the (S/N)-ratio of the rotational signal distributed over the electronic response of the detector to one probe pulse. We bring the detection out of the balanced position by tilting the $\lambda/2$-waveplate and detect a series of full electronic pulses. Additionally, we calculate the standard deviation σ of the normalized signal for every sampling point, again covering the full range between two pulses. We use the standard deviation to plot the (S/N)-ratio of the normalized signal for every delay time between the trigger and the data acquisition, retrieving a quantity equivalent to the S/N-ratio $\theta/\sigma(\theta)$ of the probe rotation θ (see Fig.2.7)). It becomes clear, that the S/N-ratio is very unevenly distributed over

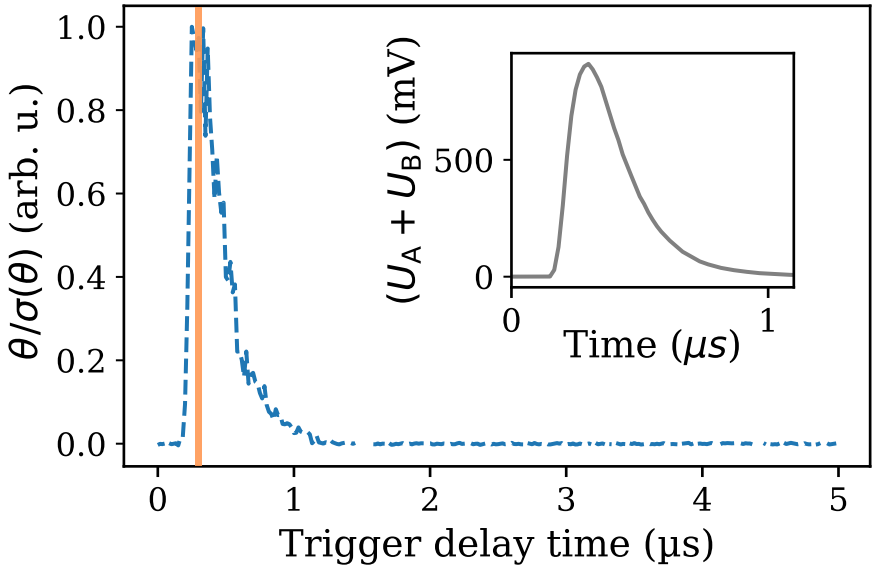

Figure 2.7: Signal to noise ratio of the detector's response on an incoming laser pulse (details are given in the main text). The orange line marks the position of the detection. Gaps in the graph for $t > 1.5\,\mu s$ are caused by numerical limitations. Inset: The detector voltage of the single diodes.

the electronic signal. Therefore the trigger delay and aquisition window are set to detect only at the marked position.

The EOM reference signal is a short TTL signal that does not necessarily overlap with the data acquisition window. Therefore, a simple RC circuit stretches the TTL signal to several microseconds. The presence of a high voltage in the EOM reference channel indicates that the modulator is opened and a pump pulse was present for the detected pulse. The data can then be sorted into pulses with (U_{ON}) and without (U_{OFF}) the presence of a pump pulse. At this point of the data processing, all the single pulse information is available and can be evaluated. Within the framework of

the pump-probe measurements performed in this thesis, only the average value is of interest, as a boxcar averager or Lock-in amplifier would return it. Therefore, to save computational resources, the sorted data is averaged over several pulses and the average for every channel with the pump opened and blocked is saved. The influence of the calculations on the experimental time is kept to a minimum by performing it simultaneously with moving the delay line. From this data, it is possible to calculate the pump-induced rotation of polarization $\Delta\theta$ from eq.(2.8) and eq.(2.9) using the calibration factor a:

$$\Delta\theta = \frac{(U_{\text{A-B}})_{\text{ON}} - (U_{\text{A-B}})_{\text{OFF}}}{(U_{\text{A}})_{\text{OFF}} + (U_{\text{B}})_{\text{OFF}}} \cdot a \quad . \tag{2.10}$$

The pump-induced reflectivity $\Delta R/R$ or analogue the pump-induced transmissivity $\Delta T/T$ can be retrieved as

$$\Delta R/R = \frac{\left[(U_{\text{A}})_{\text{ON}} + (U_{\text{B}})_{\text{ON}}\right] - \left[(U_{\text{A}})_{\text{OFF}} + (U_{\text{B}})_{\text{OFF}}\right]}{(U_{\text{A}})_{\text{OFF}} + (U_{\text{B}})_{\text{OFF}}} \quad . \tag{2.11}$$

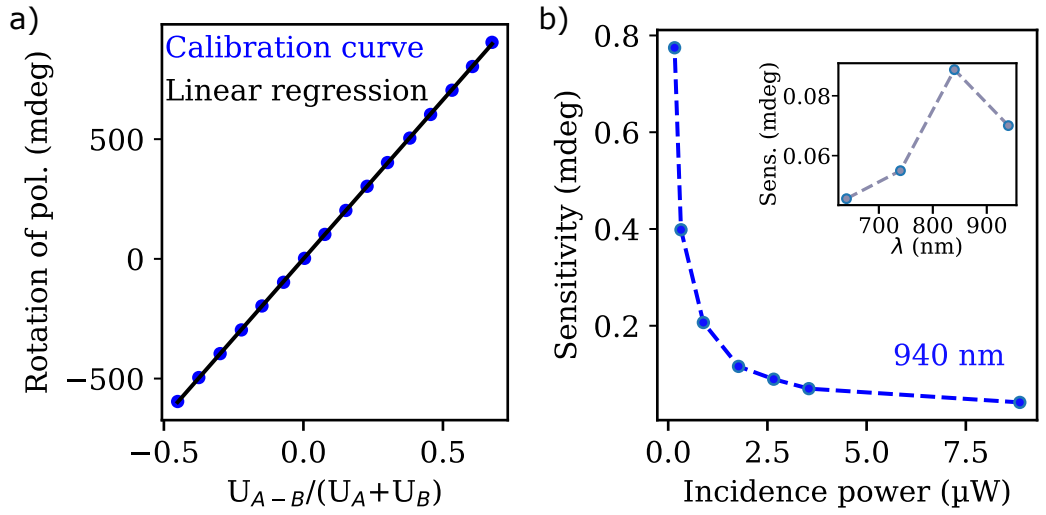

Figure 2.8: a)Calibration curve of the balanced photodetector. b) Calculated sensitivity as a function of the incidence probe power. Inset: Sensitivity for different probe wavelengths at a constant power. In both cases the probe is reflected by a cobalt single crystal sample.

The calibration of the detector is performed to convert the normalized difference signal $U_{\text{A-B}}/U_{\text{A}} + U_{\text{B}}$ into a rotation value. It is done by placing a $\lambda/2$-waveplate

in the detection line and by rotating it with a motorized stage in a polarization range of one degree, by steps of 100 mdeg. The detector signals are then measured as a function of the rotation angle. In Figure 2.8, the polarization angle θ is plotted against the total light intensity normalized difference signal $U_{\text{A-B}}/(U_{\text{A+}U_{\text{B}}})$. Following eq.(2.8) and the linear response of the detector a fit of the function:

$$\theta = a \cdot \frac{U_{\text{A-B}}}{(U_{\text{A+}U_{\text{B}}})} + c \tag{2.12}$$

is applied. The fit parameter $a = 1.3$ deg is the calibration factor and c is a possible offset from the balanced position. With the calibration, it is now possible to convert the balanced detector signal into a polarization rotation value and estimate the detection sensitivity. The sensitivity is estimated by taking the standard deviation of a group of data points, each consisting of 16000 light pulses, which amounts to about half a second of recording time. This standard deviation is then multiplied by the calibration factor a, returning a sensitivity value. The procedure is performed for several fluences of the probe beam, as shown in figure 2.8 b), returnig a possible sensitivity of less than 50 µdeg. As one may expect, the sensitivity increases with increasing illumination. The more critical information that can be taken from this data is, that high sensitivity can even be achieved with low probe fluences of less than 5 µJ/cm^2 (beam diameter 110 µm). A low fluence will be crucial for sensitive samples, which might suffer thermal damage in higher absorbing areas. Additionally, the probe photon energy is varied at a constant incidence fluence of 3.5 µJ/cm^2 (see inset Fig.2.8 b)). The sensitivity varies depending on the reflectivity of the sample (here, a cobalt single crystal) and all following optics, as well as on the spectral dependence of the diode's response.

Typical sources of noise within the experiment can be the following:

- 1/f-noise: This type of noise originates primarily from electronic noise created by any given resistor. As the name already suggests, it scales by apporximately the factor 1/f. This means that a high repetition rate and modulation frequency can dampen it to a minimum level [75].

- The power grid: Small variations in the power grid might influence several electronic components, which can be seen especially in the photodetector. Critical are disturbances in the power line which are close to the modulation frequency of the EOM, which by itself can interfere with the power supply in the laboratory. This can especially be the case when many electronic devices in the laboratory have high power consumption and draw significant amounts of current from the power lines.

- Laser pulse-to-pulse noise: This type of noise describes the variations between single laser pulses. For our system, these variations are typically low compared to the electronic noise.
- Diode misalignments: The balanced photoreceiver is sensitive to slight misalignments, as the non-normal incident angle on the active area of the diodes changes their response time and, misbalancing the detector's electronics and thus canceling out its common noise rejection capabilities.
- Thermal drift: A temperature gradient in the laboratory can lead to the expansion or contraction of any given optic, thus causing misalignment of the system
- Vibrations: Vibrations in the lab can have a variety of sources, such as as vacuum pumps, compressors or simply transmitted through the ground by other building facilities. Vibrations will cause spatial variations between the pump and probe beam. They are especially critical in flake samples, where they cause intensity variations due to the flake edges moving over the light.
- Digitization: The data acquisition board has a limited resolution. Nevertheless, as the binning size is variable and offsets can be applied to set the dynamical range close to the expected signal range, resolution loss by digitization can be neglected compared to the electronic noise of the photodetector.

2.6 Magnet and cryostat

We use a combination of a superconducting magnet and a flow-cryostat to control the initial magnetization of the sample. The strong exchange coupling in antiferromagnets requires strong external fields to impact the magnetization. The option to cool the sample to liquid helium temperature and heat it above room temperature allows to explore magnetic phase transitions in various materials.

The superconducting magnet can create magnetic fields of up to $\mu_0 H = \pm 9\,\mathrm{T}$ in the polar geometry i.e., parallel to the incident direction of the light. Figure 2.9 shows a schematic of the magnet, together with the time dependence of the magnetic field during a full ramping process. The ramping rate is reduced at higher fields to avoid a quenching of the superconducting magnet. It is a fully closed-cycle system, cooled by a pulse tube cryo-refrigerator, which cools by the expansion of externally compressed helium gas. The sample is placed on the cold finger of the cryostat, which by itself can be moved inside the magnet's bore. The magnet is a solenoid that creates a homogeneous field in almost the whole bore, allowing the sample to be moved inside the magnet. Both instruments, the magnet and the cryostat, are

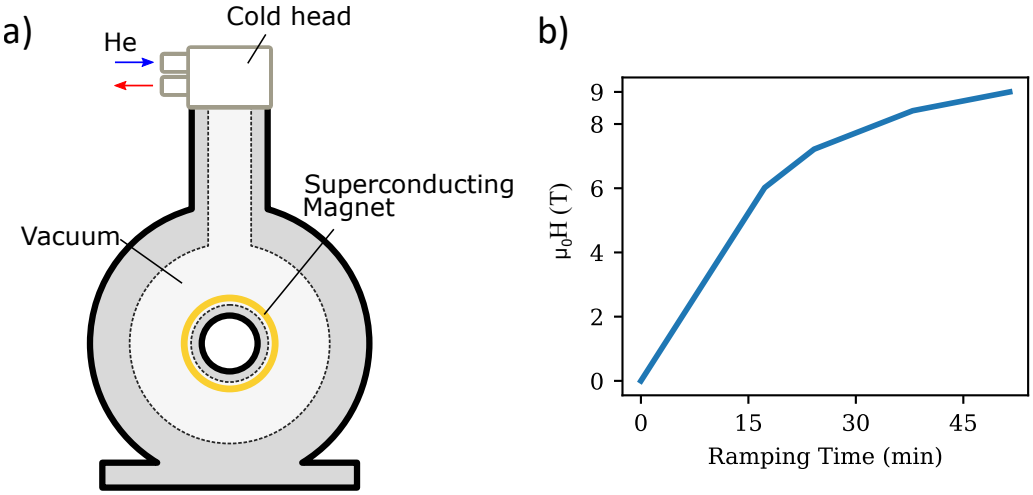

Figure 2.9: a) The layout of the superconducting magnet. The cold head is connected to an external helium compressor unit, forming a closed-cycle helium cooling system. The field is accessed via the bore in the center. Adapted from Ref.[76]. b) Ramping time of the magnet from 0 T to the maximum of 9 T. The ramping rate is decreased step-wise at higher fields. The maximum field is reached after 50 minutes.

mechanically decoupled to avoid the transfer of vibrations created by the magnet's helium compressor. This is crucial for the experiments, as the sample systems with exfoliated flakes can be as small as several micrometers and undamped vibrations can easily exceed this order.

In contrast to the closed cycle cooling of the magnet, the cryostat is a flow cryostat, cooled by a constant flow of liquid helium (or, alternatively, nitrogen), provided by an external helium dewar. A combined turbo- and membrane pump pumping stand evacuates the cryostat to a pressure of at least below 10^{-2} mbar before cooling, typically below 10^{-4} mbar. The coolant flow is given by a membrane pump connecting the outlet of the cryostat to the helium recovery, thus creating an underpressure in the cryostat, as shown in the schematic of the cryostat in figure 2.10 a). The flow can be regulated by a needle valve in the transfer line between the dewar and cryostat or, more importantly, by a computer-controlled magnetic proportional valve (MPV) in front of the membrane pump. For the full cooldown, the maximum voltage is applied to the MPV, fully opening it. For precise temperature regulation, the MPV voltage is lowered to reduce the helium consumption to a minimum. Simultaneously, the PID control of the heater inside the cryostat is activated, which is able to either keep a constant temperature at a stability of less than 10 mK or sweep it at a constant rate. The total temperature range that is

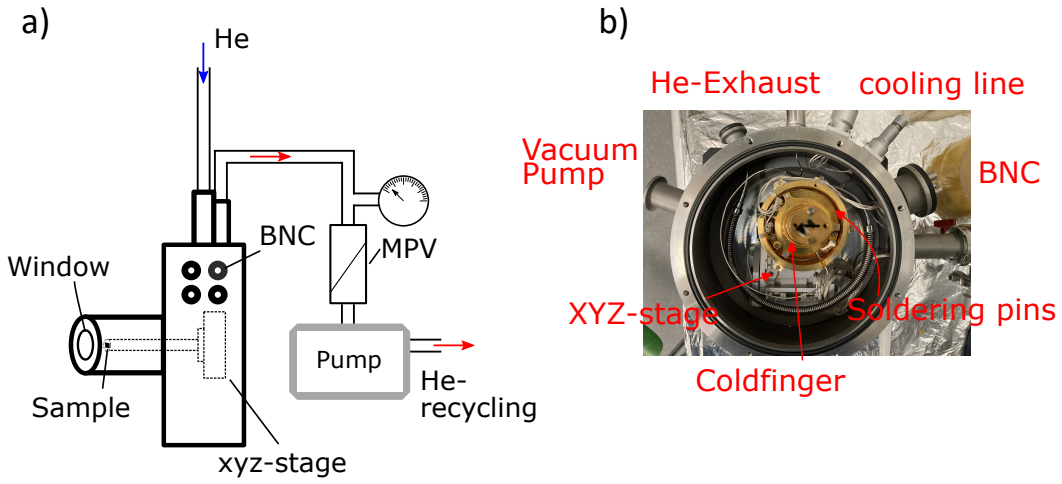

Figure 2.10: a) Layout of the cryostat and the helium flow. The arrows indicate the flow of the incoming liquid cooling medium (blue) and outcoming gas (red). Instead of helium liquid nitrogen can also be used as a coolant. Adapted from Ref.[76] b) Inside view of the flow cryostat.

spanned ranges from T =4 K, when cooled with liquid helium, up to $T = 420$ K.

Figure 2.10 b) shows the inside of the cryostat. Several electrical feed-throughs in the cryostat connect internal soldering pins to external BNC connections. The connections allow for installing electronic devices and sensors inside the cryostat and applying electric fields on the sample. The electric field can be created by applying one electrode to the sample holder plate and the second one on the sample surface, given that it was prepared with a conductive covering layer. A typical cover-layer material is indium-tin-oxide (ITO), which shows a high conductivity while still allowing mostly undisturbed optical access to the sample in the visible and IR-range due to its transparency and refractive index close to one [77]. Given the high electronic breakthrough voltage in near-vacuum conditions, the maximum electric field is mainly limited by the external voltage supply. It can lie in the range 10 kV/mm for typical bulk crystal thicknesses in the 100 µm regime.

The sample is mounted on a piezo-driven three-axis translation stage with nanometer precision. High position control is essential for choosing homogeneous sample areas, especially in Flake samples of lateral sizes down to 5 µm, and moving the sample inside the focus position of short working distance microscope objectives.

2.7 Microscopic pump-probe configuration

In the previous paragraph, we discussed the general optical setup and the beam path in a configuration optimized for macroscopic samples. Nanometer thick samples in the form of exfoliated flakes however, can have lateral sizes in the order of ten micrometers or less. Some structures may consist of terraces of different thicknesses with lateral sizes also down to less than 10 micrometers.

The low optical contrast between thin flakes and the substrate and their small size requires a dedicated imaging system including a high magnification and sample illumination. In a setup configuration like the one previously described, designed for macroscopic samples, locating the position of flakes on the substrate is feasible only for relatively large specimens. Moreover, the laser spot size in the focus plane will surpass the lateral size of the flakes. Therefore, to fully capture the unique properties of a flake or a specific terrace, we adjust the experimental system for the use of microscope optics.

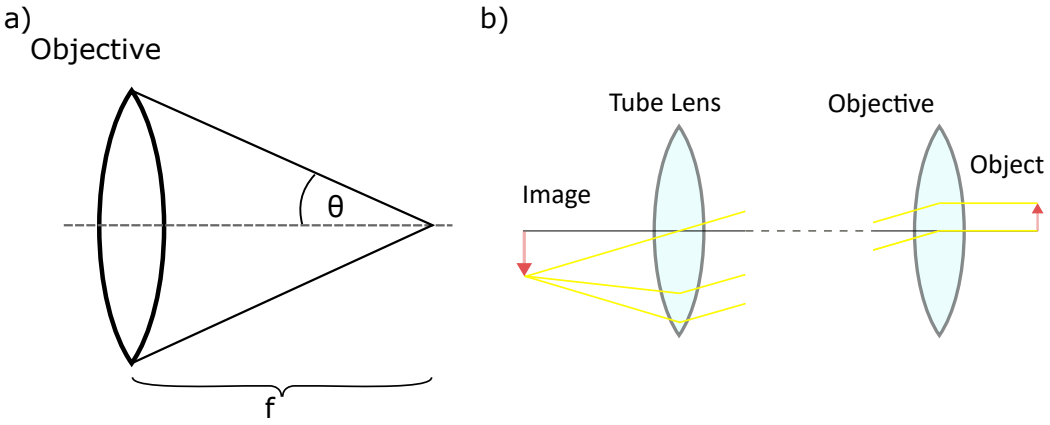

Figure 2.11: a) Schematic of the light cone created by an objective with a numerical aperture of NA=$n \sin\theta$. b)The parallel light beams enable additional optics to be placed in the virtually arbitrary wide settable gap between the objective and the tube lens. Adapted from Ref.[78].

We use an infinity-corrected microscope objective as the focusing optic and deploy it in a collinear pump and probe beam scheme. The microscope objective functions as the focussing and recollimation optic for both the pump and the probe beam and allows the observation of a microscopic image of the sample surface. Some necessary specifications of a microscope objective relevant to our purposes are the numerical aperture (NA), magnification and working distance. The numerical aperture describes the angular range in which light can be accepted into or emitted

by the microscope and is defined as [78]:

$$NA = n \sin\theta \tag{2.13}$$

Where n is the refractive index of the medium between the objective and the sample surface and θ describes the half of the cone angle created by the opening of the objective (see Fig. 2.11 a). In our case, this medium is air or the vacuum inside the cryostat, as no immersion agent is used. We, therefore, can assume $n \approx 1$. The numerical aperture is descriptive for the diffraction limit, in which a structure of the minimal size d can be resolved by the objective and for the smallest possible laser spot size. The diffraction limit of an objective with the numerical aperture NA to resolve a structure of the size d is given by the Abbe-equation[79]:

$$d \geq \frac{\lambda}{2NA} \tag{2.14}$$

The equation describes the special case in which the numerical aperture of the objective is the same as the numerical aperture of the condenser lens used for illumination. Here, this assumption applies, as the same objective is used for illumination and light collection. The equation is derived from the smallest diffraction grid, which still allows detecting at least the first order of side maxima created by a diffracted point of light [78, 79]. Comparable to the smallest resolvable structure, the numerical aperture also provides a focused laser's smallest possible spot size. For a perfectly Gaussian beam shape and a large beam diameter compared to the objective's entrance pupil diameter, the full width at half maximum of the laser spot is given as

$$FWHM = 0.51\frac{\lambda}{NA} \quad . \tag{2.15}$$

The working distance is defined as the distance between the outer part of the objective and its focal plane. A high working distance is often desirable for applications in magneto-optical experiments, as geometrical constraints in the form of cryostats can define a gap between the sample and the closest objective position. According to eq.(2.13), the numerical aperture describes the opening angle of the microscope objective. The minimal geometrically necessary working distance at a fixed objective opening limits the possible range of suitable NAs. The magnification of an objective M_{Design} is typically provided with the corresponding design tube lens focal distance f_{Design} for which this amplification applies. The effective magnification of an infinity-corrected microscope objective with which an interim image is created will then be calculated as follows:

$$M_{\text{Eff}} = M_{\text{Design}} \cdot \frac{f_{\text{tube}}}{f_{\text{design}}} \tag{2.16}$$

An additional ocular after the interim image would be used in a full microscope setup, multiplying the effective magnification from the microscope objective and tube lens by the ocular magnification [78].

Infinity-corrected microscope objectives project the image from the focal plane at infinity, not creating an interim image by themselves but only in combination with a tube lens. In other words, the light scattered from the focal plane will be collimated by the objective and the light that enters the objective will be focused in the focal plane. An incoming laser beam will then be focused by the objective alone and will again be collimated by it, allowing it to propagate further into a detection or imaging scheme.

The mostly employed infinity-corrected objective is produced by the company Mitutoyo. It has a numerical aperture of $NA = 0.42$ at a working distance of 17 mm. The objective is apochromatic and designed for use in a wavelength range of 480 nm to 1800 nm (2.6 eV - 0.7 eV). It has a magnification of M_{design}=50x at f_{design}=200 mm.

In the here described collinear setup (see Fig.2.12), we use a set of wide spectral range non-polarizing plate beam splitters for collinearization of the pump and probe beam ($\text{BS}_{\text{collin}}$), for catching the reflected light and guiding it to the detection scheme (BS_{det}) and an optional one to illuminate the sample surface with white light (BS_{ill}). The pump and probe beam hit the first splitter $\text{BS}_{\text{collin}}$ at a 90° angle relative to each other, one being transmittted, the other reflected. Both, now collinearly aligned beams, transmit through BS_{det} and enter the objective in normal incidence, while a beam dump blocks the reflected component. The objective focuses the beams on the sample surface and collimates the reflection. The outcoming beam is then again reflected by BS_{det} and guided to the detection scheme, as described in the previous sections.

As both beams are spatially overlapping, the pump has to be filtered out by means of one or a set of color filters. In some of the experiments, when pumping in the infrared, it is possible to choose a pump photon energy below the detector's sensitivity, e.g., in the case of Si-diodes below 1.1 eV.

A white light tungsten-halogen lamp (Throlabs SLS201L) is used to image the sample surface, and the flip-mounted beamsplitter BS_{ill} is inserted before BS_{det}. A collimator lens brings the white light in an almost collimated state. The inserted beam splitter is coupled into the beam path and guided along the same path as the pump and probe beam. After the reflection from the second beam splitter, the light is intercepted by a flip mirror at a position before the detection scheme begins. After being collimated by the microscope objective, the white light will create the image of the sample surface at infinity. Therefore, we place a lens in the

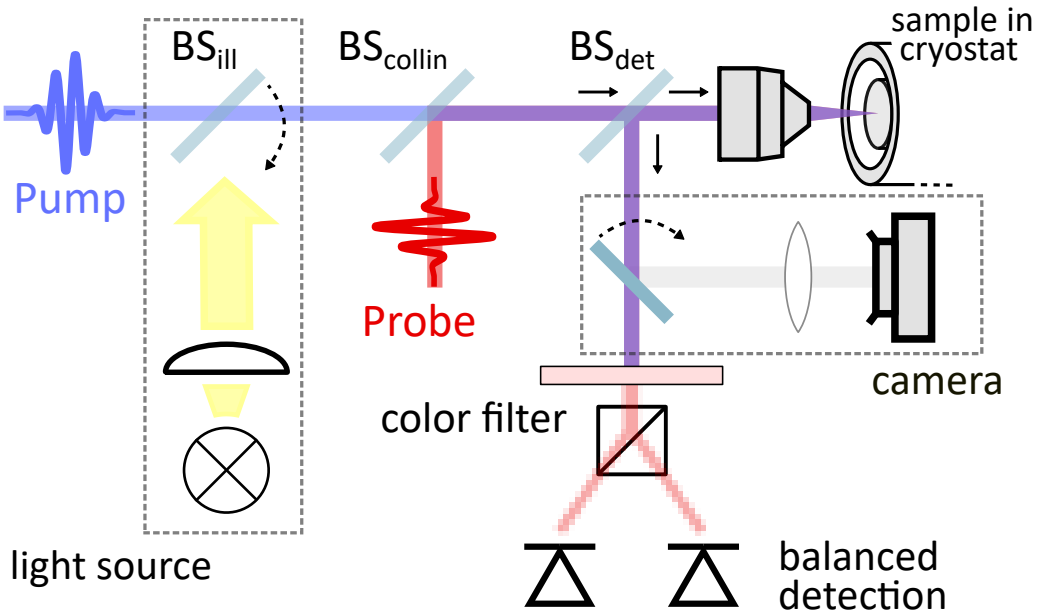

Figure 2.12: Schematic view of the experimental setup for the time-resolved investigations of microscopic samples.

beam path, which will instead create an image in the focal plane of the lens (see Fig.2.11). A camera sensor will detect the image and transfer it to the computer at this position. Alternatively, it is possible to use a spectrometer at the same or an equivalent position, which may be used for static optical or optical contrast spectroscopy. Optical-contrast spectroscopy on selected flakes measures the changes in the reflection spectra caused by the absorption in the flake and the interference between the light reflected from the substrates and the flakes' surface. It thus shows a dependence on the flake thickness and can be used to approximate the number of layers [80].

2.8 Experimental software and graphical user interface

A data acquisition card detecting single laser pulses at a high repetition rate will create a significant amount of data points. The high amount of data makes careful on-the-fly data handling and time and memory-efficient data processing in the software necessary. The control software is implemented in Python and is operated via a graphical user interface (GUI). In this section, we will describe the concept of

the software and the essential information, which, together with the documentation in the Python script, can help expand or apply changes to the program.

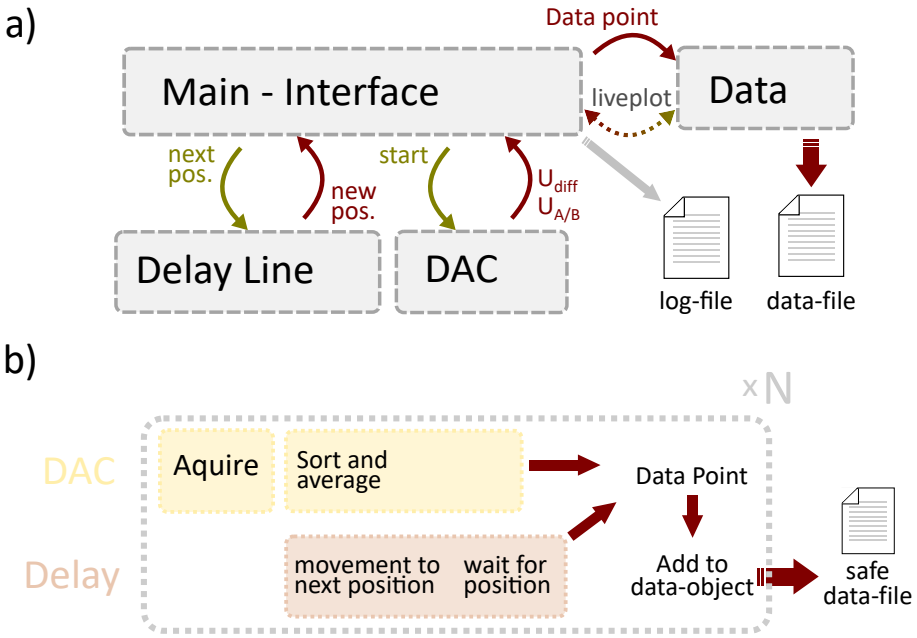

Figure 2.13: a) Schematic of the relation between different objects in the experimental software. b) Timing between the data acquisition card (DAC) and the delay line during the time-resolved measurement.

The control software consists of several classes representing the main interface, instruments and the acquired data. The main object creates the GUI, generates the other objects and functions as a hub between them. Figure 2.13 a) schematically shows the relation and exchange between the different objects and the files created by the measurement.

With the software's start-up, a data object and an object for every instrument, including the data acquisition card (DAC), are created. A live-plotting function is operated in a separate thread to not interfere with the GUI inputs while continuously updating the initial data object with the current detector signal and delay line position. The data object can return several quantities calculated from the sorted detector outputs, as described in section 2.5. These quantities are requested from the main object and displayed in the live-plot canvas. The instrument objects communicate with the instrument itself by sending commands. These commands, which are integrated into the instrument's driver, can dictate actions such as setting the next position on the delay line or initiating the arming command for the DAC. Other instruments can be and are implemented analogously but will be neglected

here. By starting a measurement, the main object will read out several text boxes for the experimental parameters in the GUI and save them together with the name of the data-file in a logging file.

At the beginning of each measurement, the plotting thread is stopped and a new data object is created and replaces the data object used for the live plotting. The following loop is shown in figure 2.13 b). The delay line moves to the initial position, and starting from here, the DAC detects the first train of electronic pulses emitted from the detector for the set number of trigger events. In the next step, the delay line controller receives the command to move to the delay line's next position. While the controller moves the delay line, the collection of data pulses is sorted and averaged. Together with the delay line position, averaged detector intensities are added as a new data point in the data object. After the experiment is finished, the data object writes a '.txt' file in the form shown in table 2.1.

Table 2.1: Strucure of the save file created after the measurement is completed.

Delay(1,1)	$(U_{\text{A-B}})_{\text{ON}}$	$(U_{\text{A-B}})_{\text{OFF}}$	$(U_{\text{A}})_{\text{ON}}$	$(U_{\text{A}})_{\text{OFF}}$	$(U_{\text{B}})_{\text{ON}}$	$(U_{\text{B}})_{\text{OFF}}$
Delay(1,2)		⋱				⋮
⋮			⋱			⋮
Delay(2,1)				⋱		⋮
⋮						⋮

Delay (i, j) denotes the exact delay position for scan number i and the position j within the scan. For non-time-resolved experiments, as static magnetic fields sweeps, the free experimental parameter will be listed in an additional column.

The programming structure of the DAC is set by the manufacturer to be compatible with different programming languages. The data types of the variables are similar to those in the C programming language, but a shared library allows them to be used across multiple languages. The software driver provides functions for creating the card handle, controlling the data transfer and setting or retrieving parameters of software register entries. The hardware settings are given by the entries of the so-called software register, which either executes a command or sets the entry to a defined value. Some of them are the number of acquired trigger events, the segment size or acquisition window in units of discretization steps, the delay between trigger and acquisition, and the dynamic range of the analog to digital conversion (ADC).

The data is transferred between the card and computer in a first-in-first-out method. The total shared buffer has a size of

$$\text{Buffersize} = 2\,\text{byte} \cdot \textit{loops} \cdot \textit{Segment size} \cdot \textit{Active channels} \tag{2.17}$$

corresponding to 2 bytes for each detected value. The minimum segment size is eight and the variable *loops* indicates the number of acquired trigger events, res. total probe pulses. The detected data is organized in the card by an array, starting with the first sample of the first channel and iterating through the channels first and then the trigger events. The samples are saved in values of the ADC and can be converted into actual values of the input voltage V_{in} via:

$$V_{\text{in}} = ADC \frac{V_{\text{range}}}{ADC_{\text{max}}} \tag{2.18}$$

Here ADC is a value given by the analogue to digital conversion with a maximum range up to, ADC_{max} and a maximum set voltage range of V_{range}. It is also possible to apply individual offset voltages to each channel to fill out the maximum dynamic range.

2.9 Conclusion

In summary, we build and demonstrate a versatile state-of-the-art optical setup for use in time-resolved pump-probe experiments. The laser system allows continuous and independent tuning of the pump and probe photon energies between 0.5 eV and 3.5 eV. Another standout feature of the laser system is the electro-optical modulator, which is triggered by the laser system itself and allows for a 100% pump amplitude modulation at 50% of the laser repetition rate. For the detection, the high modulation frequency is combined with a data acquisition card (DAC). The DAC performs a single pulse detection and gives an easy interface for adding additional detection instruments, which can possibly be used as reference signals in transmission or reflectivity experiments. An experimental software in Python controls the experiment and minimizes the impact on computational time caused by sorting and averaging processes. The closed loop magnet can create fields of up to 9 T and the continuous-flow cryostat can cool the sample down to liquid helium temperature. The mechanical decoupling between the two systems reduced the transfer of vibrations. The setup can be adapted for use on microscopic samples, which is done by employing a dedicated collinear scheme with a microscope objective. The piezo-driven three-axis translation stage in the cryostat can precisely position different sample positions into the focus of the laser light.

3 Ultrafast demagnetization in Cobalt[1]

In this chapter, we will demonstrate the capabilities of the apparatus built within this thesis's framework. We chose a simple system to study to ensure accurate benchmarking, namely the prototypical $3d$ ferromagnet cobalt that can be described within the Stoner model of band ferromagnetism. We use a (0001) cut of the hexagonal crystal at a thickness of 2.5 mm to perform a characterization by static Kerr rotation and by measuring the ultrafast demagnetization, an already well-investigated phenomenon. Moreover, the Kerr rotation experienced from the probe beam by a magnetized cobalt sample provides a strong magneto-optical effect [81]. The demagnetization measurements are performed as a function of various free experimental parameters, namely the pump fluence, sample temperature, pump photon energy and magnetic field, to prove the setup's reliability and performance.

3.1 Basics of ultrafast demagnetization in ferromagnets

The ultrafast demagnetization describes the quenching of the magnetization in a metal after the excitation via a femtosecond light pulse. It has been a topic of major interest since its discovery in 1996 [2] and has been widely studied since then [82–87]. The basic concept of ultrafast magnetization quenching is the excitation of hot electrons via the laser pulse and the following transfer of energy and angular momentum to the lattice and, most importantly, the spin system.

A macroscopic, phenomenological description is given by the three-temperature model (see Fig.3.1). In the three-temperature model, we consider three subsystems given by the electron, lattice, and spin system. Each of the subsystems is assigned a temperature (T_e,T_l,T_s) and heat capacity (C_e, C_l, C_s). The heat reservoirs of the three systems are in exchange with each other, which is described by the coupling constants G for the electron-lattice, electron-spin, and spin-lattice interaction, which, as a part of a phenomenological description, are typically left as free fit parameters.

[1] Parts of this chapter are published in "Wide Spectral Range Ultrafast Pump–Probe Magneto-Optical Spectrometer at Low Temperature, High-Magnetic and Electric Fields" In: *Review of Scientific Instruments* 91.11 (2020)

With the given assumptions, a differential equation for each of the subsystems can be formulated [2, 88]:

$$C_e(T_e)dT_e/dt = -G_{el}(T_e - T_l) - G_{es}(T_e - T_s) + P(t) \tag{3.1}$$
$$C_s(T_s)dT_s/dt = -G_{es}(T_s - T_e) - G_{sl}(T_s - T_l) \tag{3.2}$$
$$C_l(T_I)dT_l/dt = -G_{el}(T_l - T_e) - G_{sl}(T_s - T_l) \tag{3.3}$$

The term $P(t)$ describes the initial heating from the laser pulse introduced into the electron heat reservoir by the absorbed photons, which are then transferred to the lattice and spin system. After the electron excitation, the system is brought into a non-equilibrium state and until the three subsystems regain a thermal equilibrium, the classic thermodynamical approach can not be applied [30]. Typical timescales, as the demagnetization or re-equilibration time, lie in the sub-picosecond to picosecond range.

Different studies about the ultrafast magnetization quenching in cobalt have been performed on thin films grown on a substrate [82, 89–91]. They have revealed a dependence of the spin dynamic on the magnetization axis in cobalt [89] and a lower demagnetization amplitude compared to nickel due to its comparably high Curie temperature [82].

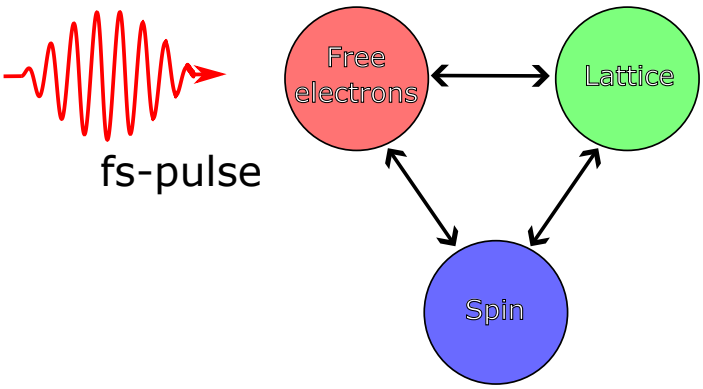

Figure 3.1: Schematic of the three temperature model. A fs-laser pulse excites free electrons, which interact with the lattice and spin subsystem by the exchange of energy and angular momentum, leading to a decrease in magnetization.

3.2 Static characterization

In preparation for the experiments on ultrafast demagnetization in cobalt, we perform a static magneto-optical characterization of the sample. The magnetization curve obtained will provide quantification of the saturation field strength and the Kerr rotation. These informations provide the necessary field strength to have the sample in a defined fully magnetized initial state and enable the conversion of transient Kerr rotation values into demagnetization values.

We use the probe line of the setup described in the previous chapter to measure the static polar magneto-optical Kerr effect from a cobalt (0001) single crystal. The sample is mounted inside the cryostat at room temperature and a magnetic field is applied in the out-of-plane direction, while the linear polarized probe beam is focussed via a spherical mirror on the sample surface. The field is varied in a loop from $\mu_0 H$ =3 T to $\mu_0 H = -3$ T and back. During the field sweep the rotation of the polarization of the probe beam is continuously detected, resolving the magnetization curve (see Fig. 3.2). The measurement is performed for three different probe

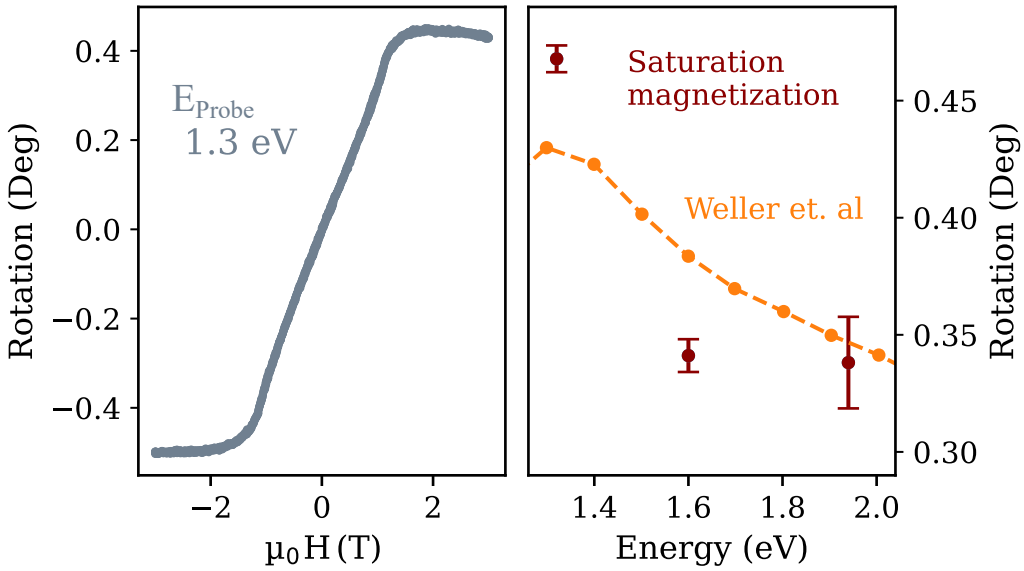

Figure 3.2: Left: Static Kerr rotation of Co(0001) as a function of the external magnetic field field. The field is ramped in a ±3 T loop. A paramagnetic background is removed from the data. Right: Kerr rotation at the saturation magnetization for different photon energies, compared to literature data taken from ref.[81]. Figure adapted from [6].

photon energies to investigate the photon energy dependence of the magneto-optical response.

A diamagnetic background is present in the raw field sweeps and was removed within the process of the data analysis. It is caused by the glass of the cryostat and optics within the range of the magnetic field, which is superimposed on the cobalt crystal's ferromagnetic contribution. The saturation magnetization is reached at about 1.5 T for all measurements. By averaging the absolute rotation values of the magnetization curves plateaus, where the saturation magnetization is reached and the Kerr effect from the cobalt is supposed to induce the maximum rotation, we receive a measure for the strength of the magneto-optical response at the individual photon energy (see right part of Fig.3.2). The strongest response is observed at 1.3 eV, which further on will be used as the probe in the time-resolved experiments. The spectral dependence is consistent with the one reported in the literature [81], which shows the maximum magneto-optical effect at 1.3 eV and is decreasing for higher photon energies.

The polarization rotation θ_{Sat} at the saturation of the magnetization $M_{\mathrm{Sat}} > 1.5\,\mathrm{T}$ will be used in the demagnetization measurements to convert the transient rotation into relative values of demagnetization. In general, the following relation holds for the conversion between magnetization in the z-direction and the transient Kerr rotation in the polar geometry:

$$\frac{\Delta M_z}{M_z(\mu_0 H)} = \frac{\Delta\theta}{\theta(\mu_0 H)} \tag{3.4}$$

With $\Delta\theta$ corresponding to the pump-induced rotation of the probe polarization.

In the appendix, the static characterization is demonstrated on a flake sample of Fe_2GeTe_2, which exhibits a strong out-of-plane magnetic anisotropy [92, 93]. In contrast to the static magnetization curves on the bulk cobalt crystal an apparent hysteresis is visible.

3.3 Pump fluence dependence

We now turn to the time-resolved experiments and conduct pump-probe measurements on the cobalt (0001) sample. The probe photon energy is fixed at 1.3 eV, since it was proven in the previous section to be within the range of the highest magneto-optical response. The pump photon energy is set to 1.8 eV, a value showing high conversion efficiency in the OPA. While both photon energies are fixed, we tune the pump fluence by rotating the $\lambda/2$-waveplate in a waveplate-polarizer attenuator combination. The Co-crystal is mounted within the evacuated cryostat and kept at

room temperature. To ensure that the sample is fully magnetized, we apply a 2 T magnetic field, which lies above the saturation field of 1.5 T.

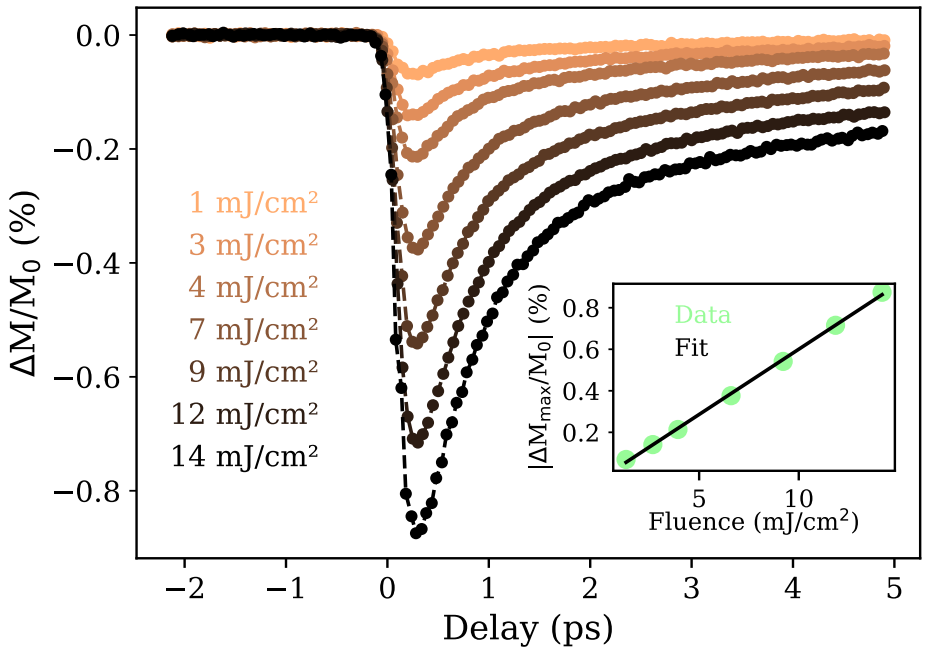

Figure 3.3: Pump-fluence dependence of the ultrafast demagnetization curves in a bulk cobalt crystal. The inset shows the maximum demagnetization plotted against the pump-fluence together with a linear regression curve. The error bars lie within the size of the markers.

Figure 3.3 displays the pump-probe traces for a pump fluence varied between 1 mJ/cm^2 and 14 mJ/cm^2. The transient rotation of the probe polarization is converted into a value of the relative demagnetization $\Delta M/M_0$ by using the static rotation of polarization at the saturation level (see Fig. 3.2) as a normalization factor. Since in the saturation magnetization all domains are aligned along the z-direction, we can adjust equation 3.4 to:

$$\frac{\Delta M}{M_0} = \frac{\Delta\theta}{\theta(\mu H_{\text{sat}})} \tag{3.5}$$

The transient demagnetization shows the typical profile of a fast demagnetization after the laser excitation on a timescale of 100 fs, followed by a first magnetization recovery in the order of 1 ps, after which the electron, lattice and spin subsystems achieve thermal equilibrium and a slow magnetization recovery over tens of picoseconds begins [89, 94]. It can be seen that the demagnetization increases with

increasing pump power. By extracting the maximum demagnetization $\Delta M/M_0$ and plotting it as a function of the pump fluence (see inset Fig.3.3), a linear dependence becomes evident, as already reported for the maximum demagnetization in nickel [87].

Moreover, the increase in the pumping fluence also impacts the characteristic time scales within the demagnetization [82, 87]. Figure 3.4 displays the fluence-dependent demagnetization curves normalized on their maximum demagnetization. At late delays, the normalized demagnetization recovers faster for lower pump fluences. This becomes clear when the normalized demagnetization for late delays ($t < 4.5\,\mathrm{ps}$) is plotted as a function of the fluence in the inset of figure 3.4. Still, the relative change in the recovery level only lies at approximately 30 % at a pump-fluence increase from $1\,\mathrm{mJ/cm^2}$ to $14\,\mathrm{mJ/cm^2}$ and no further variations in the dynamics, as the delay-time of the maximum magnetization quenching, are observed. Thus, the effect of the pump fluence on the demagnetization dynamics is lower than reported for other systems [86, 87]. The origin of the resilience of the de- and remagnetization dynamics can be ascribed to the high Curie-temperature of cobalt compared to other ferromagnets [82] and the bulk type of our sample, as most demagnetization studies have been performed on thin film materials [89].

Sensitivity

As this chapter's main aim is to benchmark the setup, we can now use the pump-probe traces to verify the system's sensitivity. To quantify the minimum detectable polarization, we use the probe rotation at negative delays of the previous pump-probe experiment and calculate the standard deviation of the data points. We display the distribution for the single scans and the average over three pump-probe scans in Figure 3.5. The standard deviation returns for single scans a sensitivity of $43\,\mu\mathrm{deg}$ in accordance to the in chapter 2 determined value. The pump-probe traces shown in figure 3.3 and 3.4 display the average over three scans for each trace, resulting in a minimum detectable rotation of $26\,\mu\mathrm{deg}$, which is well following the expected factor of $1/\sqrt{3}$ for normally distributed data. Regarding relative demagnetization, the conversion via Eq. (3.5) returns a sensitivity equal to $\Delta M/M = 0.002\,\%$.

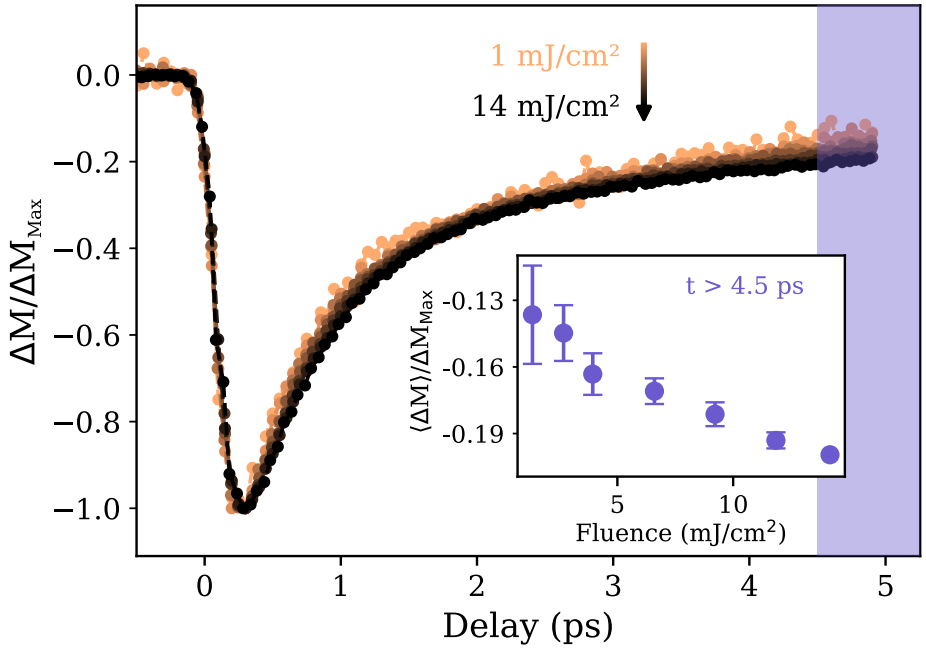

Figure 3.4: Demagntization curves for different pump-fluences normalized to the maximum demagnetization. The remagnetization time increases for higher fluences. Inset: Mean normalized demagnetization at delays above 4.5 ps (purple area).

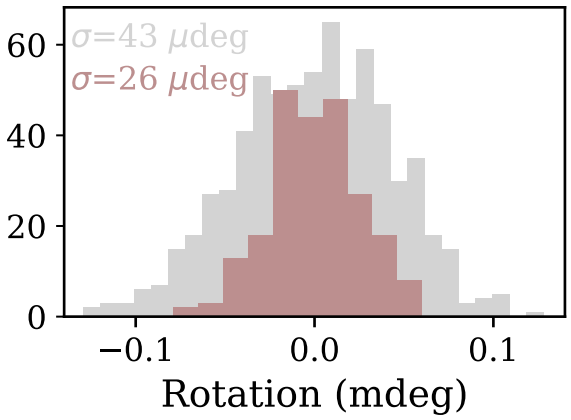

Figure 3.5: Distribution of the probe rotation of polarization at negative delays for single scans (grey) and over three scans averaged (brown) data points.

3.4 Temperature dependence

In the next step, the functionality of the cryostat is highlighted. A liquid helium flux through the cryostat is established to decrease the sample temperature down to 10 K. The sample is heated in incremental steps of 50 K and the ultrafast demagnetization is detected for each temperature increment (see Fig. 3.6). Throughout the measurements, the pump fluence is kept constant at 9 mJ/cm^2. It is worth noting that cobalt has a higher Curie temperature than nickel or iron, exceeding 1300 K [95]. Since this value is considerably higher than the maximum temperature used in the experiment, no significant change in the maximum demagnetization was observed. Still, the remagnetization visibly slows down at higher temperatures, as it can be observed at late delays in the pump-probe traces. The change in demagnetization time is consistent with previous findings in nickel [87].

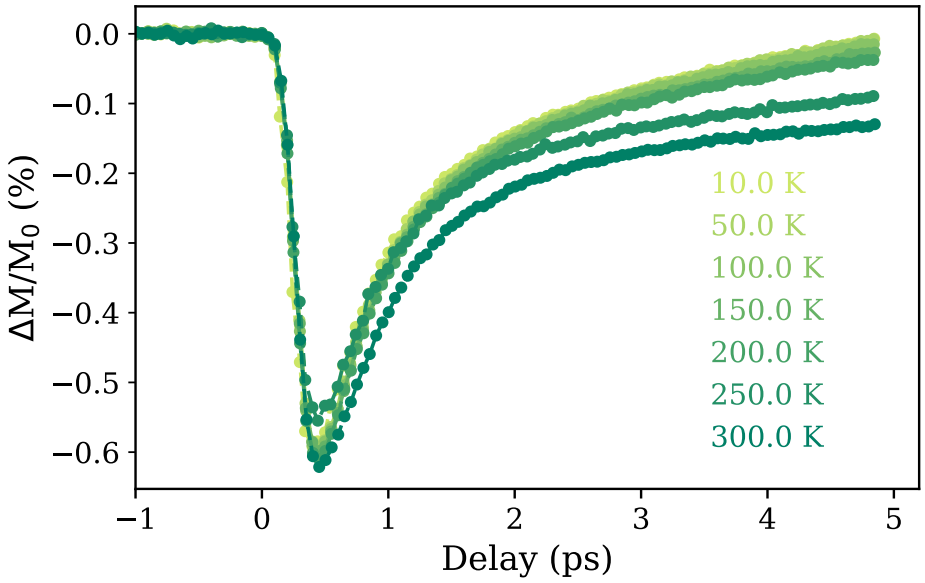

Figure 3.6: Temperature dependence of the ultrafast demagnetization curves in cobalt at a fluence of 9 mJ/cm^2. The pump and probe photon energies are set to 1.8 eV and 1.3 eV respectively.

3.5 Pump photon energy dependence

We tune the pump photon energy between 0.8 eV and 3.0 eV, while keeping the fluence at 1.2 mJ/cm^2, a value that can be reached even by the low conversion

factor ranges of the OPA. For proper comparability, it is ensured that the fluence is correctly set by measuring the beam diameter of the pump in the focus position for each photon energy and the pump power is adjusted accordingly. The sample is kept at room temperature throughout the whole experiment.

As the photon energy is tuned, the zero delay position changes due to the movement of the OPA internal delay line and the switching of the wavelength separator mirrors, depending on the current spectral range. Therefore, a common condition for the zero position for each pump-probe trace is set to achieve good comparability between the pump-probe traces. We define the zero delay as the delay where the demagnetization surpasses a threshold of a multiple of the negative-delay noise and apply the offset in the delay accordingly.

Figure 3.7 a) displays a selection of different demagnetization curves obtained for the varying excitation energies. Without further quantification, it already becomes clear that the maximum demagnetization level and the characteristic timescales vary as a function of the excitation energy. Figure 3.7 b) shows the transient demagnetization in a colormap for the whole range of excitation photon energies. The gaps between the single energy steps are interpolated for a better representation. We mark the maximum demagnetization position and the position where the magnetization quenching is reduced to 70% of the maximum, which is used as a measure of the remagnetization time. Distinct features that become visible are a non-monotonous variation of the demagnetization strength and remagnetization time. These observed spectral dependencies can not be solely attributed to the changes in the absorption spectrum, as the optical constants show a monotonous behavior [96, 97]. A definite interpretation and quantitative analysis are hindered by the fact that the exact pulse duration of the pump could not be measured during the experiment. Moreover, it might surpass the scope of this chapter, as it shall focus on proving the setup's performance. It becomes clear that the additional installation of a dedicated autocorrelation system can expand the capabilities of the setup and the range of investigatable phenomena which, as the demagnetization appears as a function of the pulse duration [98, 99].

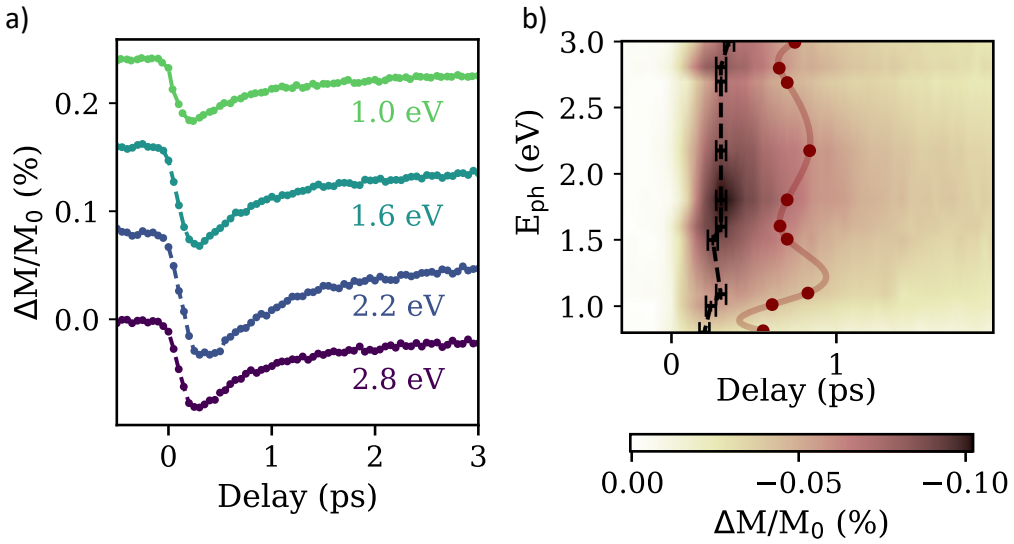

Figure 3.7: a) Ultrafast demagnetization curves for selected pump photon energies. b) Color map of the demagnetization. The black markers indicate the maximum demagnetization positions. The positions of 70% maximum demagnetization are marked in brown. The brown line functions as a guide to the eye.

3.6 Magnetic field dependence

Earlier, we showed the system's functionality at detecting the static Kerr rotation at varying magnetic fields. We will expand this demonstration by measuring the light-induced demagnetization depending on the externally applied magnetic field, increasing it up to 4 T. We keep the fluence constant at 9 mJ/cm^2 and pump at a photon energy of 1.5 eV. The pump-probe traces at different fields and the field dependence of the maximum demagnetization is displayed in figure 3.8. The demagnetization increases with increasing magnetic fields until approximately 2 T, when the saturation magnetization is reached and the pump-probe traces become hardly distinguishable. The maximum transient Kerr rotation of each trace approximately matches the Kerr rotation values extracted from the static experiment, as shown in figure 3.8 b).

In figure 3.8 the relative demagnetization is calculated and plotted against the applied magnetic field. it can be seen that the relative demagnetization increases up to 1 T, meaning that ΔM increases faster than the static magnetization, leading to a positive value of $\Delta M/M_0$. We attribute this effect to the fact that we are detecting the polar-Kerr effect, which is sensitive to the longitudinal component of the magnetization vector. While the magnetization is not saturated, some domains

do not fully align in the field direction. Even if these domains experience the same absolute demagnetization, only their magnetization component in field direction is detected by our methods.

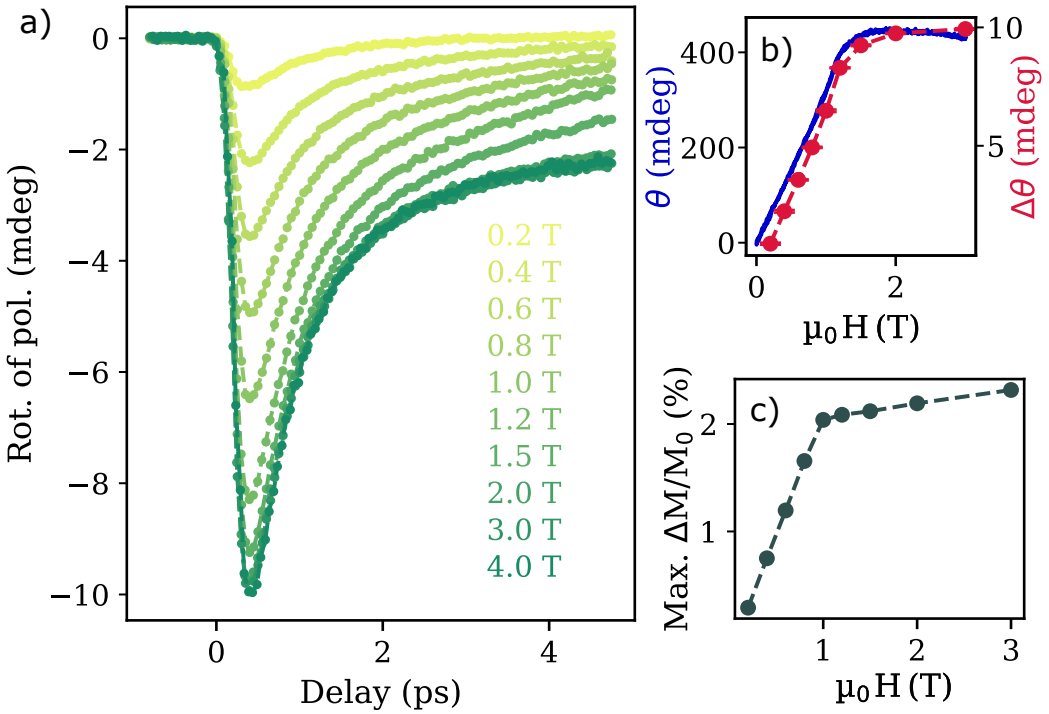

Figure 3.8: Pump-probe traces at external magnnetic fields ranging from 0.2 T to 4 T. a) Static Kerr rotation and the maximum transient Kerr rotation as a function of the magnetic field. b) Maximum demagnetization.

3.7 Conclusion

In this chapter, we have explored the experimental capabilities of the system by studying the ultrafast light-induced magnetization quenching in a single crystal of the prototypical 3*d* ferromagnet cobalt. The apparatus built for this study has been benchmarked for its sensitivity, being able to resolve rotations of the probe polarization down to $\theta_{\text{min}} = 43\,\mu\text{deg}$. The demagnetization measurements were performed as a function of various experimental parameters, including pump fluence, sample temperature, pump photon energy, and the external magnetic field.

Due to the high Curie temperature of cobalt, we observed the linear regime of the fluence dependence of the maximum demagnetization. Moreover, reduced remagnetization times were observed with increasing fluence or sample temperature. The photon energy dependence indicates a relation between the demagnetization dynamics and the excitation energy, not merely following the spectral dependence of the optical constants. This observation can be the basis for further investigations.

The demagnetization increases with increasing magnetic fields until saturation magnetization is reached. The relative demagnetization seems to increase faster than the sample magnetization, which can be attributed to the polar-Kerr effect's sensitivity to the longitudinal component of the magnetization vector.

In total, we could demonstrate the state-of-the-art sensitivity of the system and prove its wide application range for time-resolved magneto-optical experiments. Moreover, the hints for an excitation energy dependence of the ultrafast demagnetization could be used as a starting point for follow-up experiments.

4 Coherent lattice and phonon–magnonic dynamics in bulk $FePS_3$[1]

This chapter presents a study of the coherent phonon and phonon-magnonic dynamics in a free-standing bulk crystal of the van der Waals semiconductor $FePS_3$. The central element of the study is a 3.2 THz phonon mode and its close relation to the magnetic moments of the Fe^{2+} ions. First, we will introduce the optically excited phonon mode and the data analysis steps performed before the excitation process is discussed. We will explore the direct coupling of the phonon mode to the antiferromagnetically ordered state by tuning the sample temperature and exploit its hybridization with a magnon mode to induce coherent spin dynamics. All the above is performed by observing the magneto-optical effect origination from the stripe-like formation of the magnetic moments in $FePS_3$, as it can be seen in the schematic of the magnetic structure in figure 4.1.

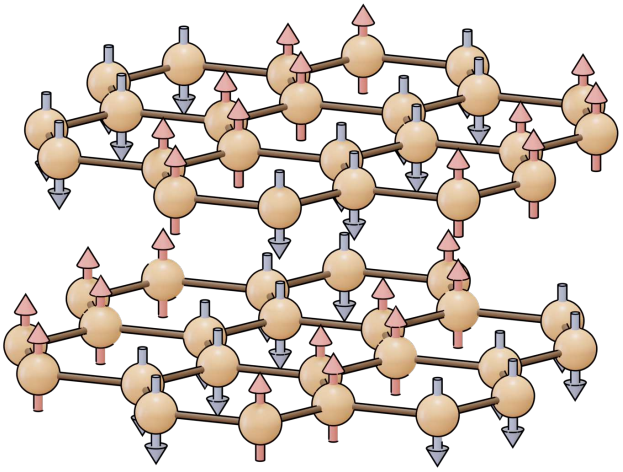

Figure 4.1: Schematic illustrating the magnetic structure of the Fe^{2+} ions within the honeycomb structure of $FePS_3$. The arrows indicate the orientation of the magnetic moments.

[1]Parts of this chapter are published in: F. Mertens et al. "Ultrafast Coherent THz Lattice Dynamics Coupled to Spins in the van Der Waals Antiferromagnet FePS3" In: *Advanced Materials* 35.6 (2023)

4.1 Coherent excitation of the phonon modes

We begin the time-resolved experiments on $FePS_3$ by pumping at a photon energy of 1.03 eV, which corresponds to the *d-d* transition between crystal field split $3d$ electrons[49, 100, 101]. The probe is kept at 1.45 eV right below the band-gap energy of E_g =1.5 eV. Both beams are aligned to near-normal incidence on the sample and are focused via $f = 50$ cm and $f = 20$ cm focal length optics, respectively. The fluence of the pump is adjusted to 2 mJ/cm^2, while the probe fluence is below 10 µJ/cm^2. The sample is cooled down via liquid helium and maintained at a temperature of $T = 10$ K . We detect the reflected probe beam in a balanced detection scheme.

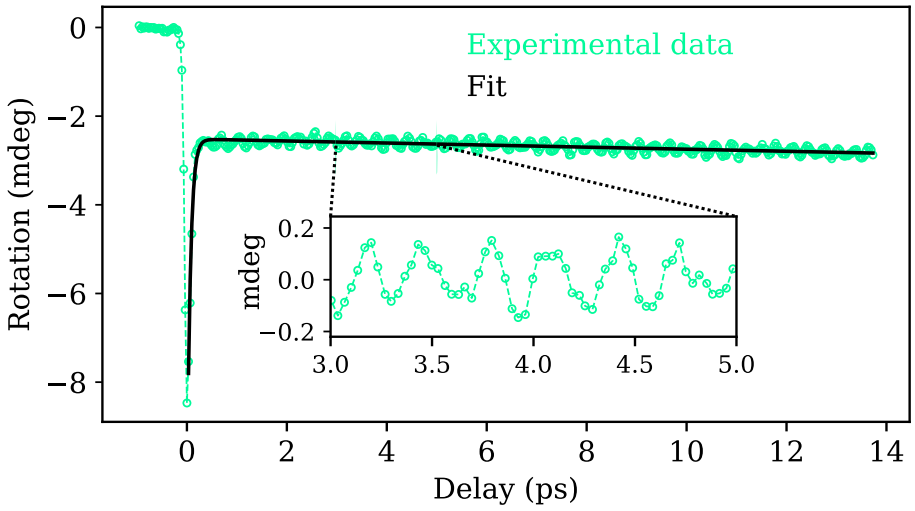

Figure 4.2: Transient probe polarization after an excitation by a pump pulse of 1.03 eV photon energy. The experimental data points are marked with the green circles and the fit to the incoherent background is shown in black. The inset shows a close-in view of the oscillations with the contibution from the incoherent background subtracted.

The time traces of the transient rotation reveal an oscillatory contribution, superimposed by an incoherent background (See Fig.4.2), which originates from an ultrafast quenching of the antiferromagnetic order parameter[32]. We estimate the incoherent background by fitting the pump-probe trace data to the following function:

$$g(t) = A_{\text{exp}} e^{-t/\tau} + A_{\text{lin}} t + c \tag{4.1}$$

We thus model the background by an exponential function in addition to a linear correctional term. The correctional term describes any dynamics with characteristic time scales exceeding the maximum delay of the measurement, which can include thermal recovery, strain-induced birefringence or lattice modes with frequencies in the gigahertz regime or lower.

We fit the transient rotation of polarization for positive delays to the incoherent background $g(t)$ and subtract it from the data to isolate the oscillatory contribution. This procedure is illustrated in Figure 4.2. Figure 4.3 shows the Fast Fourier transformation (FFT) applied to the background corrected data. The Fourier spectrum of the transient rotation reveals two distinct features at frequencies of 3.2 THz and 4.8 THz. These two frequency components in $FePS_3$ are known from Raman-scattering experiments as phonon modes, dominated by the Fe^{2+} ion vibrations [39, 57, 58, 102]. We therefore assign the oscillations to these Raman-active phonons. The two modes will be investigated closely in the following sections, focusing on the 3.2 THz mode, which is known to hybridize with a magnon mode in the presence of an external magnetic field [102, 103].

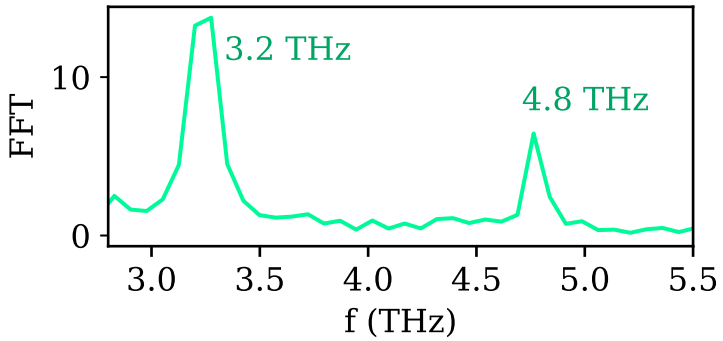

Figure 4.3: Fourier spectrum of the oscillatory signal after the contribution of the incoherent background is subtracted from the pump-probe trace.

4.2 Pump-photon energy dependence

We perform pump-probe experiments on the bulk $FePS_3$ sample as a function of the pump-photon energy to investigate the excitation mechanism of the 3.2 THz and 4.8 THz phonon modes.

The pump photon energy is tuned in a range from 0.83 eV up to 1.9 eV, while the probe is again set to 1.45 eV. Thus, we cover a broad spectrum, ranging from the

nearly transparent area in the near-infrared, across the crystal field split interband transition and above the band gap energy. The pump fluence is kept constant at $2\,\mathrm{mJ/cm^2}$ for photon energies below the band gap and, to avoid thermal damage in the highly absorbing region, at $1\ \mathrm{mJ/cm^2}$ for photon energies above the band gap. Again, the beam profile was measured before recording each pump-probe trace to compensate for spectral-dependent changes in the beam profile to adjust the laser power accordingly.

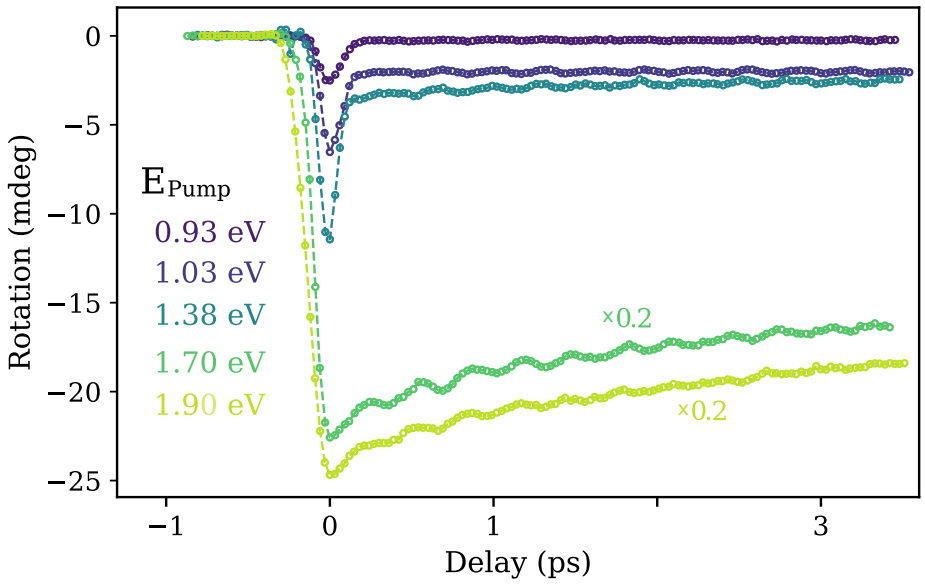

Figure 4.4: a) Transient rotation of the probe polarization for varying pump photon energies: For better comparison, only a group of data is shown. The traces excited by energies above the band gap are multiplied by a factor of 0.2 for presentational purposes.

Figure 4.4 shows the transient probe rotations for selected pump photon energies. Next to the clear increase of the incoherent background, some apparent photon-energy-dependent changes of the phonon-induced oscillations are visible as the amplitude and oscillation decay. Before interpreting the data, we describe the data-analysis steps in the following.

Data handling and phonon-lifetime

We begin the description of the data analysis by better understanding the time evolution of the phonon mode and performing pump-probe scans for longer delay

ranges up to 25 ps. The long delay range allows a precise determination of the phonon frequencies and lifetimes.

At a sample temperature of $T = 10\,\mathrm{K}$ we excite with a pump photon energy below (1.03 eV) and above (1.9 eV) the band-gap energy of $FePS_3$. The time traces (see Fig. 4.5) of both photon energies are then fitted to a term describing the incoherent background $\tilde{g}(t) = g(t) + bx^2 + dx^3$. This term corresponds to eq.(4.1) expanded by a third-order correction term, which is justified, as the isolated oscillations are the topic of interest within this study. We define the zero-delay position ($t = 0$) of the pump and probe overlap as the time position of the minimum probe rotation and shift the data accordingly.

The incoherent background is subtracted from the signal, as described before and displayed in the insets of figure 4.5. After the incoherent background is subtracted, we fit the rotation to the function $f(t)$, which contains the sum of two decaying sine waves, approximating the two phonon-induced oscillations in the signal:

$$f(t) = P_1 \sin(\omega_1 t + \Phi_1) \cdot \mathrm{e}^{-t/\tau_1} + P_2 \sin(\omega_2 t + \Phi_2) \cdot \mathrm{e}^{-t/\tau_2} \tag{4.2}$$

The amplitude of the 3.2 THz mode is described by P_1 and the amplitude for the 4.8 THz mode by P_2. At pump photon energies above 1.5 eV, only the component at 3.2 THz could be observed. Consequently, P_2 is set to zero for these pump photon energies. The phases of the two sine waves is given by Φ_1 and Φ_2, while τ_1 and τ_2 refer to the decay constants. The resulting phonon-lifetimes, retrieved by the fitting procedure, are listed in table 4.1. We assign the reduction in phonon lifetime for

Table 4.1: Lifetimes of the 3.2 THz (τ_1) and 4.8 THz (τ_2) phonon modes.

Photon Energy	τ_1	τ_2
$1.03\,\mathrm{eV} < E_\mathrm{g}$	$21\,\mathrm{ps} \pm 2\,\mathrm{ps}$	$12\,\mathrm{ps} \pm 2\,\mathrm{ps}$
$1.90\,\mathrm{eV} > E_\mathrm{g}$	$5\,\mathrm{ps} \pm 1\,\mathrm{ps}$	-

the higher energy excitation to the increased amount of scattering partners when exciting free electrons with a pump of $E_{ph} > E_g$. The already comparably low lifetime of $\tau_2 = 5\,\mathrm{ps}$ of the higher frequency mode (4.8 THz) may also be further reduced for excitations above the band gap, causing it to vanish below the noise level before it can be detected.

Moreover, the fit over many periods allows for a precise determination of the phonon frequencies. Based on the fit of eq.(4.2) applied to the pump-probe trace excited

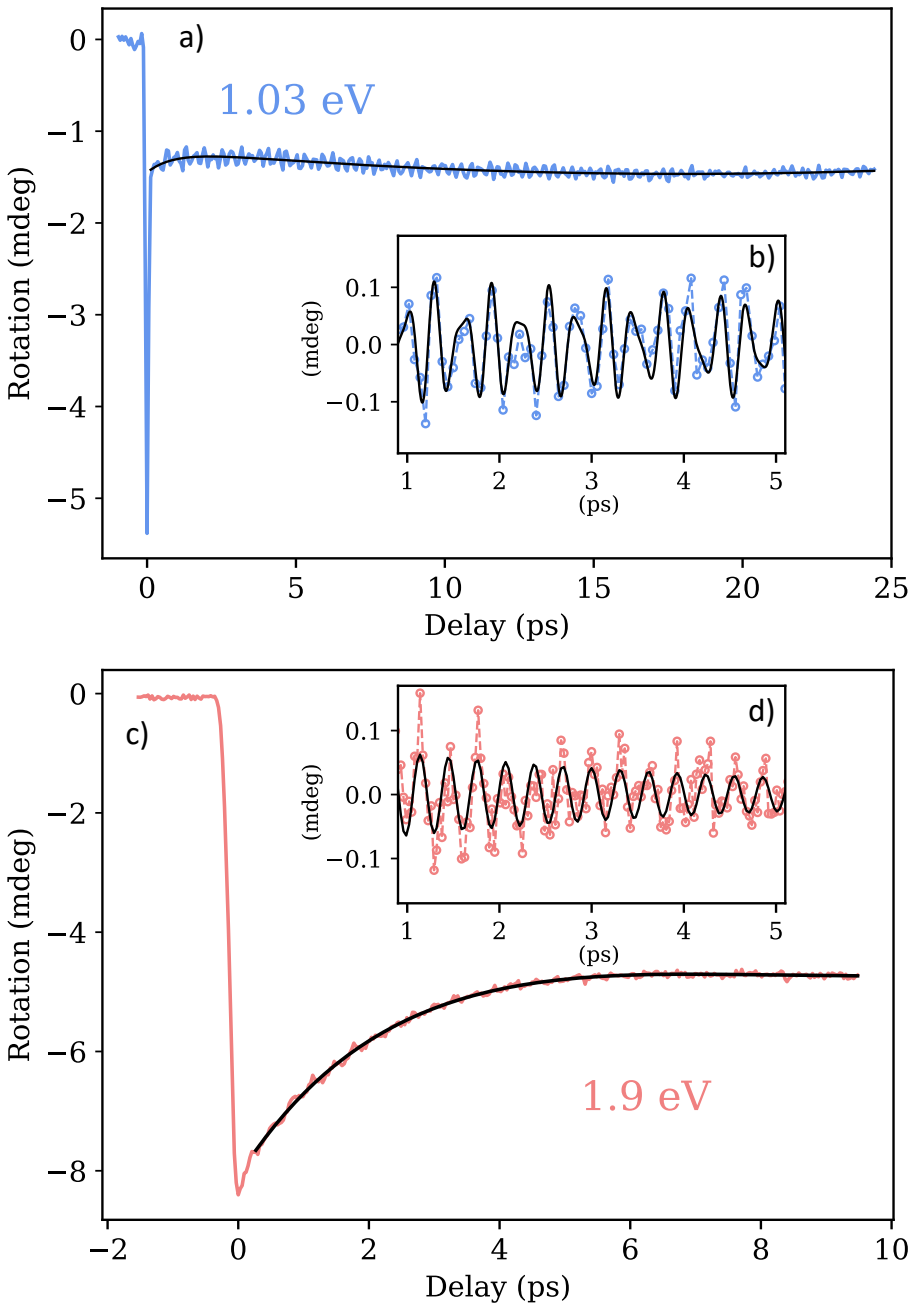

Figure 4.5: Extended pump-probe traces and background fits (represented by a black curve) were obtained at pump photon energies of (a) 1.03 eV and (b) 1.9 eV. The phonon-induced oscillations were fitted to the signal without the background contribution at 1.03 eV and 1.9 eV, as shown in (c) and (d).

below the band gap energy, we extract the following frequency values:

$$\omega_1 = 3.2407\,\text{THz} \pm 0.0006\,\text{THz}$$
$$\omega_2 = 4.780\,\text{THz} \pm 0.002\,\text{THz}$$

We can now use the findings from the long-timescale measurements and apply them to the following fitting procedures. Typically, the scan range will be less than five picoseconds, which is short compared to the lifetime of the 3.2 THz mode when excited below the band gap energy. Consequently, the decay of the 3.2 THz mode can be neglected for $E_{ph} < E_g$. For pump photon energies exceeding the band gap energy ($E_{ph} > 1.5\,\text{eV}$), the 4.8 THz mode is not present and therefore does not need to be considered for the fit. Overall, it is reasonable to separate the fit function between excitations above and below the band gap. We therefore use the following functions to approximate the time traces:

$$f_{\mathrm{E_{ph}<Eg}}(t) = P_1 \sin(\omega_1 t + \Phi_1) + P_2 \sin(\omega_2 t/\Phi_2) + g(t) \tag{4.3}$$
$$f_{\mathrm{E_{ph}>Eg}}(t) = P_1 \sin(\omega_1 t + \Phi_1) \cdot \mathrm{e}^{-t/\tau_1} + g(t) \tag{4.4}$$

The term $g(t)$ is the incoherent background, as described by equation (4.1) The two frequencies ω_1 and ω_2 will be set as fixed parameters, as well as τ_1 for excitations above E_g. It should be noted that no dependence of the phonon-frequencies for any of the following measurements was observed when ω_1 and ω_2 were left as free parameters for control purposes. Therefore, it is justified to keep the phonon frequencies as fixed parameters, using the values that could be extracted before from the long timescale fits shown in figure 4.5.

Phonon amplitude

Following the scheme presented above, we extract the photon energies for the full range of excitation energies and display them in Figure 4.6. As described before, at energies above the band gap, the 4.8 THz mode can not be detected anymore. Therefore, only the 3.2 THz component is presented for pump energies above 1.5 eV.

The detected amplitude of the phonon modes increases at two distinct electronic features. One feature lies at the electronic band gap at $E_g \approx 1.5\,\text{eV}$, where the amplitude strongly inclines. The second lies at the position of electronic *d-d* transitons (0.98 eV - 1.1 eV) between 3*d*-states of the Fe^{2+} ions split by the hexagonal and trigonal crystal fields[49, 100, 101]. The absorption spectrum, together with a

schematic of the energy levels of the crystal field split 3*d*-states is shown in figure 4.7a). This excitation is of particular interest for the miniaturization of the sample, as it lies below the band gap and thus avoids the introduction of excessive amounts of thermal energy into the delicate structure of an atomically thin specimen. The phonon amplitude almost vanishes below 1 eV, i.e., in the absence of electronic transitions[101].

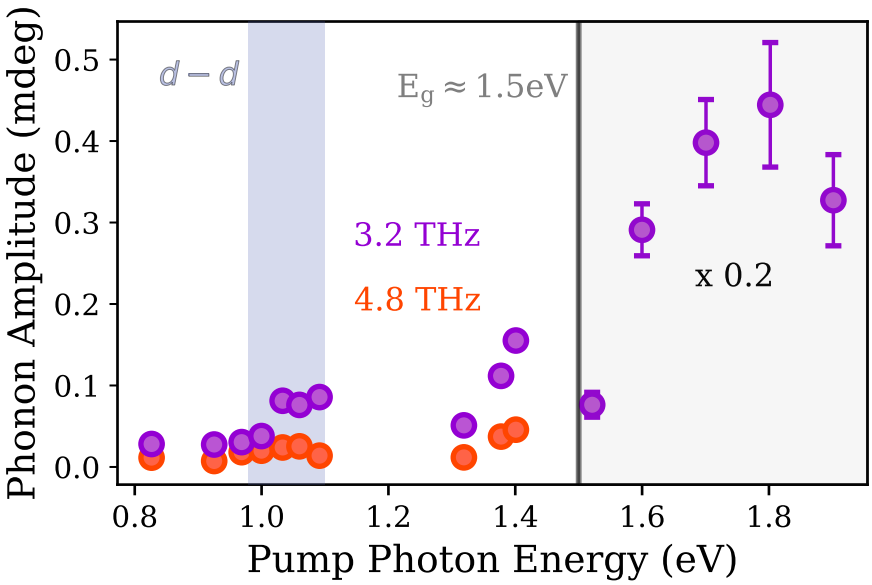

Figure 4.6: Amplitudes of the two phonon modes at 3.2 THz (purple) and 4.8 THz (orange) as a function od the pump photon energy. The amplitude of the phonon at excitations above the band gap is multiplied by a 0.2 for a better visualization. The photon energy range corresponding to the Fe^{2+} *d*-*d* transitions is marked in blue.

The observed phonon generation thus shows a strong correlation to the electronic excitations, which hints at a displacive mechanism - the displacive excitation of coherent phonons (DECP). It describes a process of driving optical phonon modes via femtosecond laser pulse excitation. By pumping in an absorbing spectral range, electrons are excited into previously unoccupied states, causing an abrupt change in the interionic potential (see Fig. 4.7b)). The new potential creates a force on the lattice, driving it to the new equilibrium position and leaving it oscillating in the phonon eigenmodes[104, 105].

Another generally possible excitation process would be the impulsive stimulated Raman scattering (ISRS). In the ISRS mechanism, the electric fields at different frequencies of a short laser pulse interact with each other and can generate a

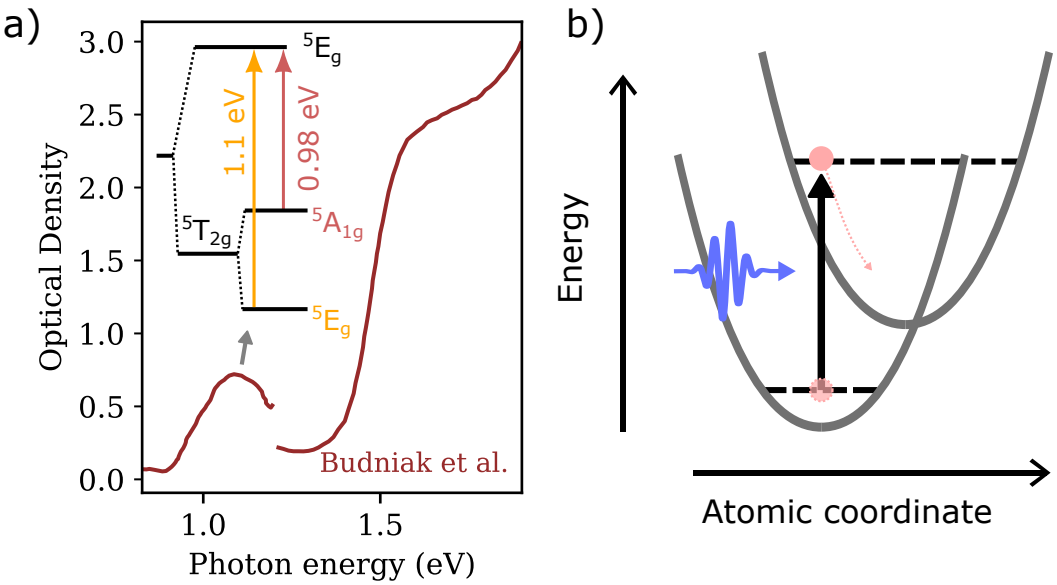

Figure 4.7: a) Optical absorption spectrum in $FePS_3$, taken from Ref. [101]. Inset: Schematic of the light-induced transitions between the crystal field split $3d$ states in the Fe^{2+} ions. b)Schematic of the DECP process. After the excitation via the light pulse, the interionic potential shifts, driving the atoms into the new equilibrium positions. Adapted from Ref.[106].

phonon (or magnon) mode. The condition for the generation is that the difference in the photon energies of two frequency components contained in the light pulse corresponds to the energy of the excited mode [107]. A precise distinction between the two processes could be made by evaluating their characteristic phases. In DECP, a cosine behavior is expected as the lattice adapts to the potential that was initially changed. In contrast to ISRS, which is a purely impulsive mechanism, where a sine-like phonon oscillation is expected when $t = 0$ corresponds to the center of the pump-pulse[104]. In our case, the $\pi/2$ of the phonon period is shorter than the typical pulse duration. This fact does not allow a reliable identification of the zero-delay position and oscillation phase. Still, in the opaque range, DECP is typically favored over a purely impulsive mechanism and can therefore be identified as the generating mechanism. [108].

4.3 Probe polarization dependence

In this section, we investigate the detection mechanism of the magnetic order and phonon modes in $FePS_3$ by examining the probe polarization dependence. We rotate the probe polarization using a half-wave plate and detect the pump-induced signal for probe polarizations in a range up to 180 degrees offset from the initial value. The sample is maintained at a temperature of $T = 10\,\mathrm{K}$ and we excite it with a photon energy of 1.03 eV, which is below the band gap energy of 1.5 eV.

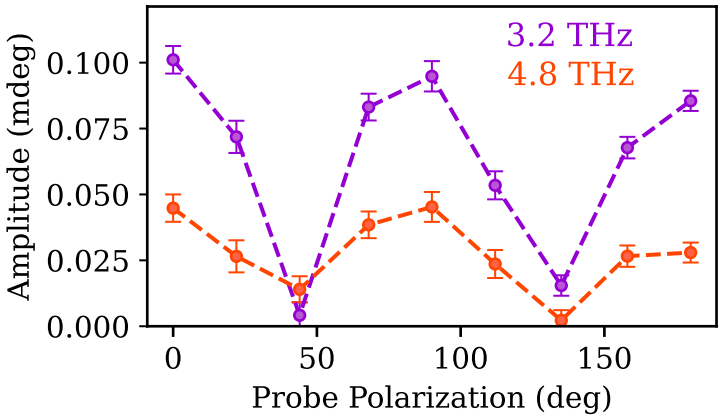

Figure 4.8: Amplitude of the 3.2 THz (purple) and 4.8 THz (orange) phonon modes as a function of the probe polarization. Adapted from Ref.[24].

The oscillation amplitude induced by the 3.2 THz and 4.8 THz phonon modes is extracted from the rotational signal and plotted as a function of probe polarization in figure 4.8. The figure shows that the oscillation amplitude has a $\pi/2$ periodicity with respect to the probe polarization. In the transition from the paramagnetic to the magnetically ordered phase, the three-fold symmetry of the lattice is broken by the formation of spin stripes of the magnetically ordered Fe^{2+} ions (see Fig.4.9). Moreover, this ordering also leads to an electronic anisotropy since the movement of electrons to a position within the same spin stripe is energetically preferred to positions of different magnetic orientations, which would require a spin flip process. This suggests the existence of optical anisotropy in the form of magnetic linear dichroism (MLD), caused by different absorption coefficients for light polarized perpendicular or parallel to the spin stripes (assuming a light incidence normal to the *ab* plane)[22, 32, 46, 47]. The observed $\pi/2$ periodicity of the oscillation amplitude is consistent with the observations of the MLD and a maximum of the dichroism-induced polarization rotation at 45° relative to the symmetry axis[46].

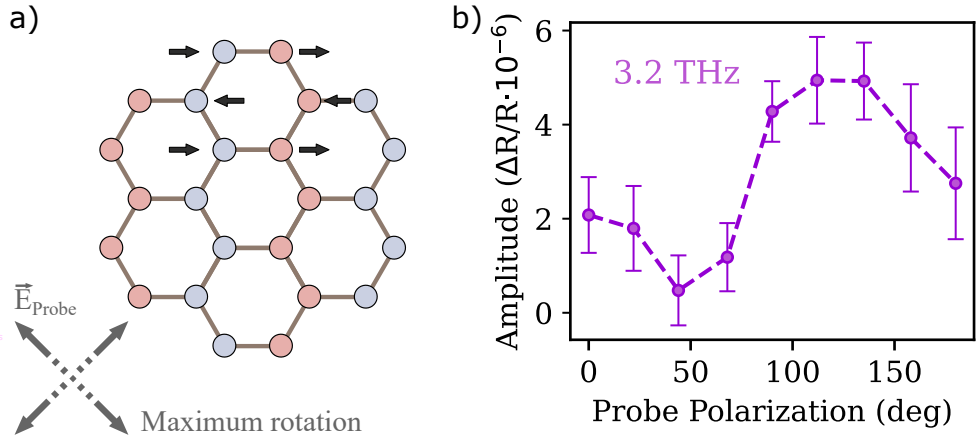

Figure 4.9: a)Formation of the magnetic Fe^{2+} ions within a monolayer of the crystal. The red and blue color correspond to the different, antiparrallel spin orientations, while the black arrows indicate the displacement caused by the phonon modes. Probe polarizations following the bottom left cross showed the highest oscillation amplitudes in the rotational signal. b) The oscillation amplitude within the transient reflectivity of the probe, as a function of the probe polarization.

From the same data set as shown in figure 4.8 and following the same data analysis procedure, we extract the oscillation amplitude from the transient reflectivity (see fig.4.9b)). Here, the oscillation amplitude shows a π periodicity, with the maximum amplitude at the position of one of the amplitude minima in the rotational signal, i.e. along or perpendicular to the spin stripe formation. In contrast to other Raman active phonon modes, the modes observed here are dominated by in-plane motions perpendicular to the spin stripe direction [39, 109]. The in-plane oscillations of the Fe^{2+} ions lead to a distortion of the spin stripes and a modulation of the light reflectivity $R_{\parallel}$ for polarizations along one axis. This axis lies either within the spin-stripe direction or perpendicular to it and an exact assignment from the present experiment is not possible. However, the phonon-induced reflectivity modulation for one polarization $R_{\parallel}(t)$, while the other ($R_{\perp}$) stays mostly unaffected, leads to a transient variation of the linear dichroism

$$\mathrm{LD}(t) = \frac{R_{\parallel}(t) - R_{\perp}}{R_{\parallel}(t) + R_{\perp}}\,. \tag{4.5}$$

which we can detect here as a rotation of the probe polarization.

The correlation between both, the probe polarization and intensity with the oscillation amplitude allows us to establish the magnetic linear dichroism as the connection between the magnetic order and the detected signal. In the following we

will continue to present the dichroism-induced probe polarization, as it provided a higher sensitivity and set the incidence polarisation to 0°.

An additionally performed the pump polarization dependend measuerment is attached to the appendix.

4.4 Temperature dependence

The results of the previous section indicate the close relationship between the observed phonon mode and the magnetic order via the magnetic linear dichroism. In the following section, we will further investigate the connection to the magnetic order by ramping the sample temperature from 10 K across the critical temperature of $T_N = 120\,K$ up to room temperature.

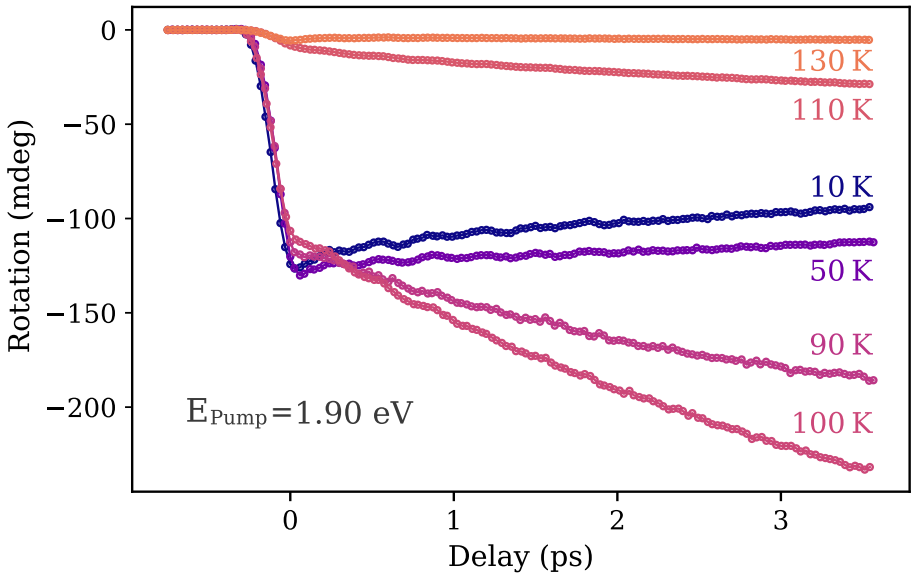

Figure 4.10: Selected pump-probe traces of the rotational signal in bulk $FePS_3$ at different sample temperatures, below and above the Néel-Temperature.

The pump photon energy is tuned to 1.9 eV into the excitation-energy regime, where the highest phonon amplitudes were observed. The pump-fluence is kept constant at $2\,mJ/cm^2$. Figure 4.10 shows the time-resolved signal for the most significant temperature steps. It is striking that the phonon amplitude and the incoherent background display a strong temperature dependence.

The temperature-dependent behavior of the background is consistent with ultrafast light-induced demagnetization. In this context, the incoherent background shows two essential features. The first and most apparent is that the appearance of the background is bound to the magnetic phase and vanishes as the critical temperature is surpassed and no demagnetization effects can be observed. We quantify the level of the incoherent background with the constant term c of the background contribution $g(t)$ (see eq.(4.1)) of the fit function and plot it as a function of the sample temperature in the inset of figure 4.11. Second, the spin dynamics show a clear temperature dependence, as the demagnetization time increases with higher temperatures until the maximum demagnetization is shifted to delays exceeding the scanning range of Figure4.10. This effect follows observations of the critical slowdown of the spin dynamics in the vicinity of T_N, which has been reported for $FePS_3$[22, 32]. The light-induced demagnetization dynamics will be further discussed in section 5.3.

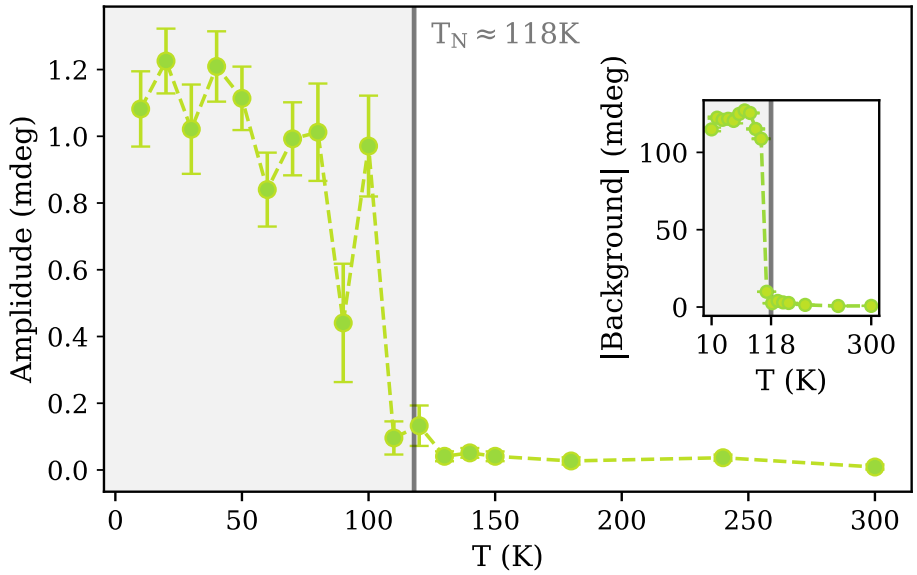

Figure 4.11: Selected pump-probe traces of the rotational signal in bulk $FePS_3$ at different sample temperatures, below and above the Néel-Temperature. Inset: Temperature dependence of the incoherent background strength.

We extract the phonon amplitude of the 3.2 THz mode, as described in section 4.2 from the transient rotation and plot it against the sample temperature (see Fig. 4.11). Here again, a clear dependence on the long-range magnetic order becomes visible. Beyond the Néel-temperature, the 3.2 THz mode vanishes from the signal. This leads to the conclusion that the 3.2 THz phonon-mode can only be excited and

detected within the antiferromagnetic ordered state of $FePS_3$.

The relation between the magnetic ordering in $FePS_3$ and the excitation of the 3.2 THz phonon mode lies in the difference between the magnetic and crystallographic unit cell, as illustrated in figure 4.12. In the transition from the unordered state into the antiferromagnetically ordered state, the unit cell is doubled in size in the *ab*-plane (see Fig.4.12a)) and expanded to the next atomic layer, as already shown in figure 1.4. As the unit cell in the *ab*-plane doubles in size, the Brilloin-zone is halved or, in other words, folded, with the *M*-Point of the non-magnetic cell collapsing into the *Γ*-Point (see Fig. 4.12b)). The 3.2 THz phonon mode, which is a zone boundary mode in the unordered state, becomes zone-centered and optically active [39, 110]. Therefore, the 3.2 THz mode is labeled a zone-folded phonon mode. The term zone-folded phonon refers to optical-phonon modes which only appear in the dispersion of the ordered phase.

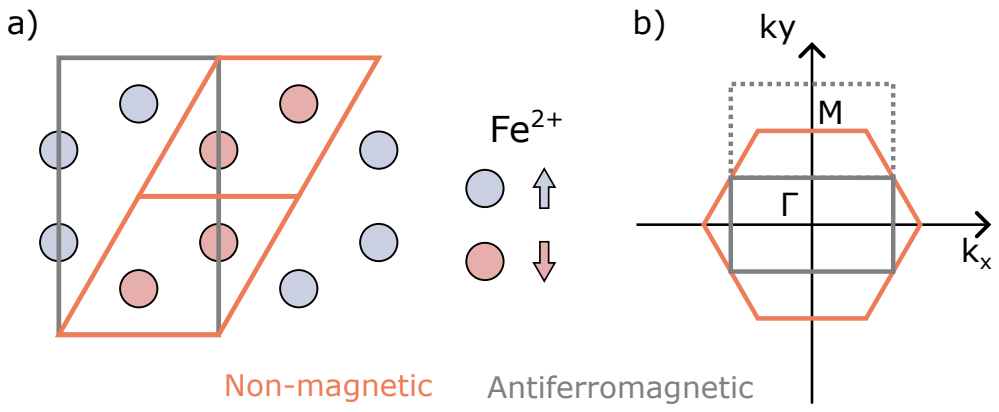

Figure 4.12: a) Magnetic (grey) and crystallographic (orange) unit cell within the *ab*-plane of $FePS_3$. The orientations of the magnetic moments are color-coded in red and blue. b) Brillouin zone of $FePS_3$ in the unordered and the antiferromagnetically ordered state. The dashed grey line shows the extension over the nearest Brillouin zone. Adapted from Ref.[39].

Transient reflectivity

We now confirm that the effect of the zone folding can also be detected in the transient reflectivity $\Delta R/R$. The magnetic linear dichroism causes the detected transient rotation, which relies on the difference between optical constants parallel and perpendicular to the magnetic stripe order in $FePS_3$. As depicted in Figure 4.13, the 3.2 THz mode can also be seen in the reflectivity and also in this case,

it vanishes above the critical temperature. The same fitting procedure as before described is used to extract the oscillation amplitude.

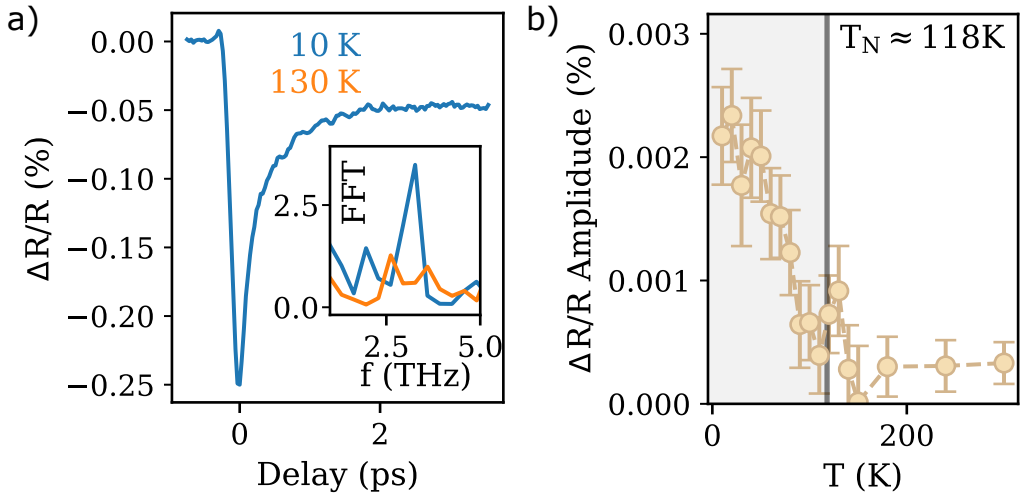

Figure 4.13: a) Pump-probe trace of the transient reflectivity at $T = 10\,\mathrm{K}$. The inset shows the Fourier transformed signal after subtracting the incoherent contribution for sample temperatures of $T = 10\,\mathrm{K}$ and $T = 130\,\mathrm{K}$. b) Oscillation amplitude of the phonon mode in the reflectivity signal as a function of the sample temperature.

4.5 Excitation of a coherent hybridized phonon-magnon mode

So far, we demonstrated the excitation and detection of two coherent zone-folded phonon modes. Due to their zone-folded origin, these modes already show a close connection to the magnetization in the material and can function as an indicator for the magnetic ordering in $FePS_3$. In this section, we will focus on the behavior of the phonon mode within the presence of an external magnetic field and study its hybridization with a zone-center magnon mode.

As a fact, the presence of a magnon mode at a frequency of 3.6 THz at 0 T has been reported in previous Raman experiments known from the literature [58]. In the presence of an external magnetic field, the Zeeman-splitting lifts the degeneracy between the modes of the two antiferromagnetic sublattices precessing clockwise and counterclockwise [111]. The lift of the degeneracy creates two frequency-branches of opposite spin ($\Delta S_z = \pm 1$), one increasing (M_+) and the other one decreasing (M_-)

its eigenfrequency as a function of the external magnetic field [112]. The frequencies of the two magnon-branches ω_+ and ω_- of change in the presence of an external field as follows[58]:

$$\omega_\pm = \gamma\left(\left(2H_E + H_A\right) H_A\right)^{1/2} \pm \gamma H_0 \tag{4.6}$$

The variable H_E is the exchange field, H_A the anisotropy field, H_0 the externally applied field in the z-direction and γ the gyromagnetic ratio.

For higher magnetic fields ($\mu_0 H \gtrsim 5\,\mathrm{T}$) applied in the direction of the easy axis (here: out of plane) the M_- branch approaches the frequency of the 3.2 THz zone-folded phonon mode, entering the strong coupling regime between the two modes [113]. In this regime, the two modes from a hybridized phonon-magnon (PM) quasiparticle (magnon-polaron), which is formed by the exchange of angular momentum from the magnon to the phonon[109]

At this point, the two modes can only be regarded as being of a hybridized character, and they become the upper (PMU) and lower (PML) branches of a hybridized phonon-magnon mode. With increasing fields, the two branches show an anticrossing behavior, leading to a frequency reduction of the PML mode and a convergence of the PMU frequency to the zero field phonon frequency of 3.2 THz. A schematic of the magnetic-field dependent branches emerging from the phonon and magnon mode are presented in figure 4.14.

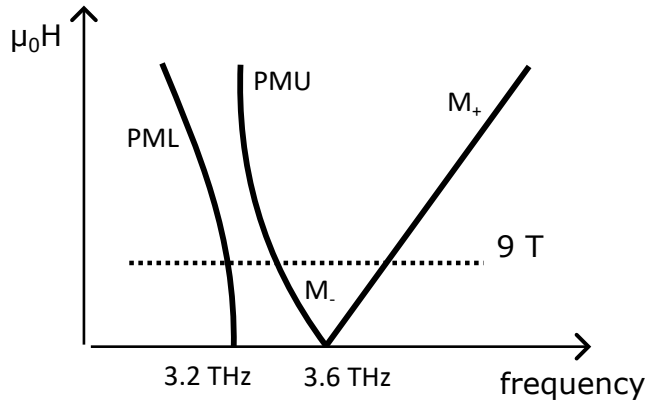

Figure 4.14: Schematic of the frequency branches originating from the 3.2 THz phonon mode and the magnon mode. Created according to the observations made in the Refereneces [103, 109, 112].

We keep the probe phonon energy at 1.45 eV at the same level as in the previous experiments and excite with a pump photon energy of 1.03 eV. At this pump photon energy, we resonantly excite the crystal field split *d*-*d* transition to induce a high

phonon amplitude while staying below the band-gap energy, where the phonon lifetime is increased compared to excitations above the band-gap energy. With a decay time of τ=21 ps it is possible to observe the changes in the signal, which emerge over time from small frequency variations. We make use of this by detecting in two different time intervals:
The first interval lies between -1 ps and 1 ps around $t = 0$ and is used to identify the zero-delay position. The second interval is in between 20 ps and 23 ps and detects several periods of the phonon mode induced oscillations (see Fig.4.15). Here, we expect to see the small variation of the frequency as apparent shifts of the phase Φ[114].

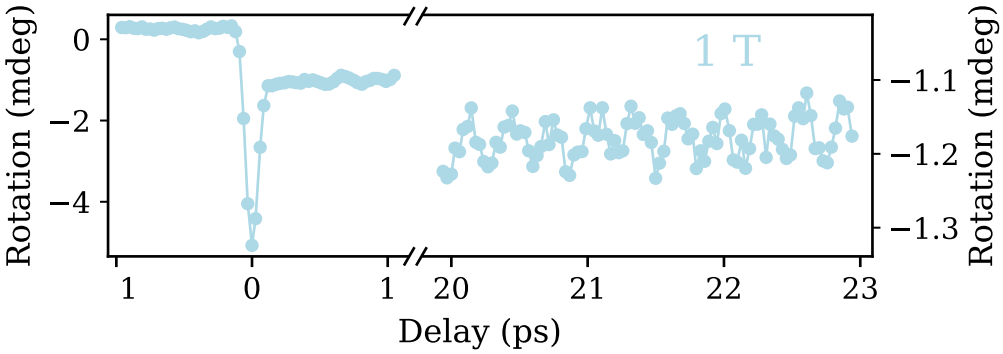

Figure 4.15: Exemplary time trace for the magnetic field dependent study. The scan is performed in two intervals containing the zero delay position and the late delay time traces, which are used to determine the changes in frequency.

As the hybridization is expected to manifest itself in small changes of the phonon oscillation frequency, we evaluate the frequency changes by determining the phase shift

$$\Delta\Phi = \Phi(0\,T) - \Phi(\mu_0 H) \tag{4.7}$$

of the oscillations at an applied field ${}_0H$ and the oscillations at zero-field in the second scan range. We fit the time traces by a sine function in the form of:

$$\Delta\theta = A\sin(\omega(0\,\mathrm{T})t - \Phi(0\,T) - \Delta\Phi)\,, \tag{4.8}$$

with $t = 21.4$ ps and $\omega(0\,T) = (3.2407 \pm 0.0006)$ THz. The oscillation frequency is set as a fixed parameter, which is justified, as the maximum time difference of one period within the scan range is expected to be shorter than the laser's pulse duration. We tune the external field in steps of 1 T up to 9 T, to the limit of our system and display the late delay traces in Fig.4.16. Now the frequency shift can be extracted according to the following relation:

$$\Delta\Phi = t \cdot (\omega(0\,\mathrm{T}) - \omega(\mu_0 H)) \tag{4.9}$$

We plot the oscillation frequency as a function of the applied magnetic field (see

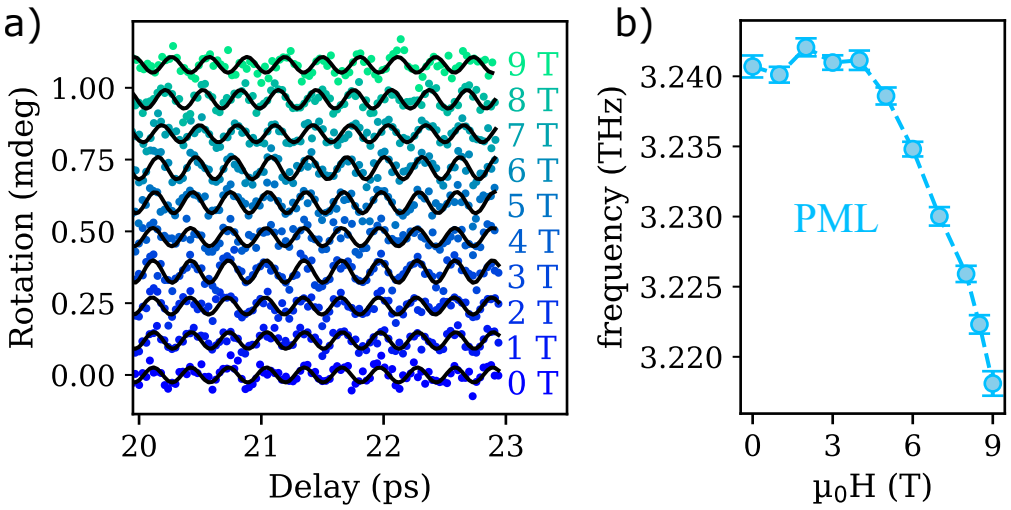

Figure 4.16: Pump-probe traces at late delays for increasing external magnetic fields. The solid black line is a fitted sine-function. The frequency shift by increasing fields becomes visible by observing the interception of the fit function with the y-axis.

Fig.4.17 b)). It reveals a frequency reduction as the field increases and the magnon mode hybridization occurs.

Two long scans at 0 T and 9 T with a gapless range between 0.1 ps and 24 ps give more inssight of the hybridized modes. Figure 4.17 shows the Fourier transformation for both cases. It can be seen that the frequency of the purely phononic PML mode at 0 T is reduced at 9 T, as already calculated before. Additionally, a second peak emerges at (3.42±0.04) THz, corresponding to the PMU mode. With our technique, the pure magnon mode with a frequency of 3.6 THz at zero field has not been detected. Therefore, we can assign the 3.4 THz component in the fourier transformed signal to the phononic contribution of the upper branch phonon-magnon mode.

We thus demonstrated a possible way to generate coherent magnetization dynamics optically via a resonant phonon excitation. The hybridized origin of the phonon and magnon mode allowed the excitation of partly magnonic dynamics using the same excitation process studied in the previous sections.

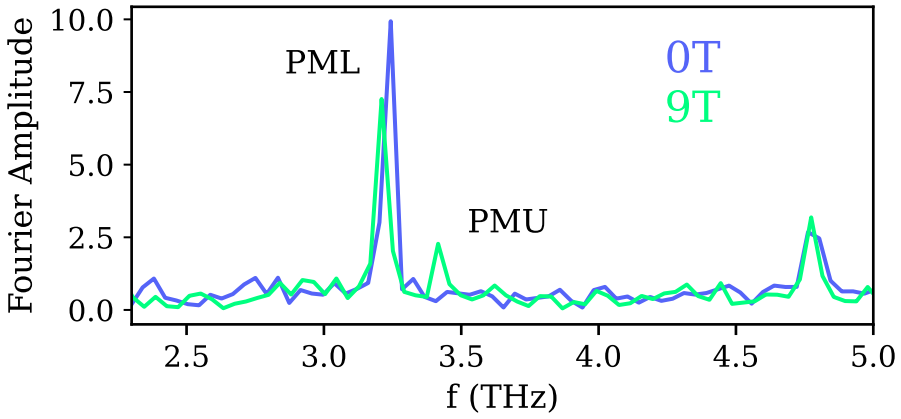

Figure 4.17: Fourier transformation of the extended scans at fields of 0 T (green) and 9 T (blue). The inset shows the lower branch phonon magnon mode (PML) frequency as a function of the externally applied field.

4.6 Conclusion

Concluding the time-resolved experiments on a bulk $FePS_3$ crystal, we demonstrated the optical excitation of coherent lattice and spin modes. The excitation process of the phonon mode could be explored by the excitation energy variation and was identified as the displacive excitation of coherent phonon. The observed phonon mode is fundamentally related to the magnetic order, as, due to its zone-folded origin, it can only be excited and detected in the antiferromagnetic phase and it hybridizes with a magnon mode in the presence of strong magnetic fields. We utilized the excitation process of the phonon mode and its hybridization to create, with the phonon-magnon polaron, a coherent magnetic excitation. The combination of pump photon energies below the absorption edge of $FePS_3$ and magnetic linear dichroism as a detection method, which is sensitive to the magnetization and was already applied down to the monolayer [47], paves the way for the generation of coherent modes in a flake sample.

5 Lattice and spin dynamics in flake $FePS_3$[1]

In the previous chapter, we performed a comprehensive investigation of coherent lattice and spin dynamics in an $FePS_3$ bulk sample. We revealed the intimate coupling of a 3.2 THz phonon mode with the antiferromagnetic order, its hybridization with a magnon mode and the displacive excitation process in a low absorption regime. Building upon this foundation, our investigation now extends toward the scalability of the observed phenomena in the experimental approach. Even though the intralayer coupling typically dominates the physical properties of van der Waals materials, the magnetic properties can be modified drastically as the few- or monolayer limit is approached [53, 92]. Moreover, miniaturization is of major importance for the fabrication of heterostructures and devices[92], as well as for the implementation in technical applications. Therefore, proof of scalability is paramount when two-dimensional magnetic materials are discussed.

In this chapter, we will present time-resolved optical experiments on an exfoliated flake $FePS_3$ sample placed on a substrate. The process of exfoliation allows the creation of specimens ranging from the quasi-bulk form down to thicknesses consisting of few- and monolayers. It is one of the default methods in the creation of these sample types. We will explore the excitation of the zone-folded lattice mode across the accessible optical range and tune the temperature across the phase transition while observing the coherent phonon and incoherent magnetization dynamics.

5.1 Sample

$FePS_3$ is exfoliated and placed as a collection of various flakes on a commercially available Si/SiO_2 substrate[2]. The 285 nm SiO_2 creates an insulating layer between the silicon and the $FePS_3$ flakes (see Fig.5.1 a)).

We selected a flake that is relatively large compared to a few-layer flake, in terms of both surface area and thickness. The reasoning behind this selection was to

[1] Parts of this chapter are published in F. Mertens et al. "Ultrafast Coherent THz Lattice Dynamics Coupled to Spins in the van Der Waals Antiferromagnet FePS3" In: *Advanced Materials* 35.6 (2023)

[2] The samples were produced within a collaboration with the group of Eugenio Coronado from the University of Valencia and Alberta Bonanni from Johannes Kepler University Linz.

ensure that the specimen has a large homogeneous surface and increased robustness. With this sample we take a first step into the investigation of flake samples, so at a later point, outside of the framework of this study, atomically thin specimens can be approached. Figure 5.1 presents a microscope image of the sample. The interference between the light reflected from the flake surface and the substrate changes the spectra of the reflected light, making different thicknesses appear in different colors in the microscopic image. The sample thickness is mapped via

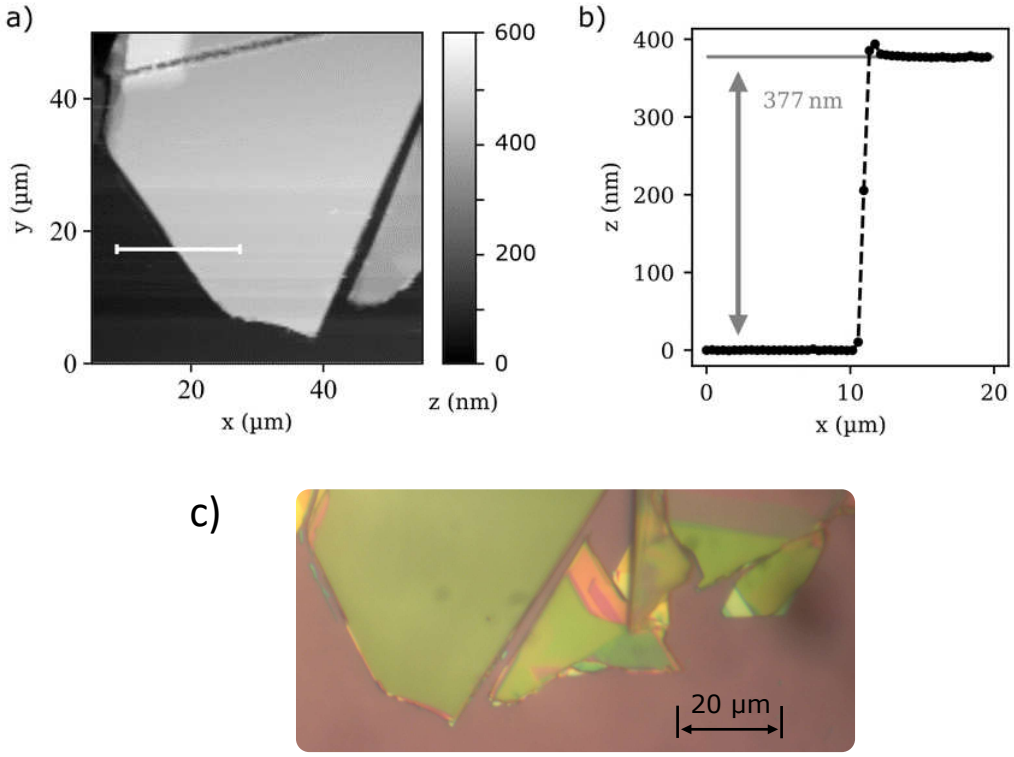

Figure 5.1: a) AFM image of the investigated flake. b) Linear height profile of the AFM-image across the edge of the flake. The thickness is estimated to 377 nm. Taken from Ref.[24]. c) Sample surface in the area of the mostly investigated flake. The image was taken using an optical microscope with reflected light illumination.

atomic force microscopy (AFM). By scanning in the tapping mode, we avoid lateral forces on the flake from the tip. The movement speed is set to 10 μm/s. Figure 5.1 presents the full AFM image and thickness calculation. We calculate the flake thickness over a linear profile along the scanning direction and taking the height difference between the substrate and the flake surface. We thus retrieve a flake thickness of 377 nm.

5.2 Pump-photon energy dependence

We modify the setup into the collinear scheme for the time-resolved optical experiments with the flake samples as described in section 2.7. We use the infinity-corrected apochromatic microscope objective (Mitutoyo) with a 50x magnification. The sample is kept at a temperature of 10 K and the probe photon energy is again set to 1.45 eV while the pump-photon energy is tuned and kept at a constant fluence of $2\,\mathrm{mJ/cm^2}$.

In the previous experiments, the pump fluence could be controlled by setting the pump power according to the beam spot size measured with the CCD beam profiler. The spot size of a 50x amplification microscope objective lies in the micrometer order and, therefore, in the same ballpark as the pixel size of the beam profiler. Here, we use a knife-edge method, relying on the cryostat-integrated piezo-driven three-axis translation stage. The edges of rectangular gold markers placed on the substrate are aligned along the lateral movement axis of the translation stage. Now the stage moves the edge of the gold marker stepwise into the position of the focused beam while the reflected light intensity I is detected. Afterward, the procedure is repeated for the other axis in case of an elliptical beam shape. The intensity of the reflected light equals the integrated beam profile. Therefore, the spot size can be estimated via the numerical derivate of I (see Fig.5.2). As the projection of a 2D Gaussian along one of its main axes is again a 1D Gaussian with the same variance, we estimate the beam diameter by approximating the beam shape in the focus position with a 1D Gaussian and use the following relation:

$$\frac{\mathrm{d}I}{\mathrm{d}x} = A \exp\left(-\frac{(x-\mu)^2}{2\sigma^2}\right) . \tag{5.1}$$

With this method, we receive a beam diameter of $(1.5 \pm 0.1)\,\mu$m for the pump and $(1.3 \pm 0.1)\,\mu$m for the probe beam along the x-axis.

The pump-probe traces for a selected range of pump-photon energies are shown in Figure 5.3. In this particular configuration, the optical range is limited to pump-photon energies below 1.1 eV - the band-gap energy of silicon. Excitations above this threshold will lead to the additional excitation of free electrons within the Si layer of the SiO_2/Si substrate, disturbing the signal. The pump-probe traces display an oscillatory and an incoherent component with intensities depending on the excitation energy, similar to the bulk sample. The fast Fourier transformation of the background removed signal reveals the 3.2 THz contribution from the zone-folded phonon mode at resonant pumping energies and an absence of any coherent modes

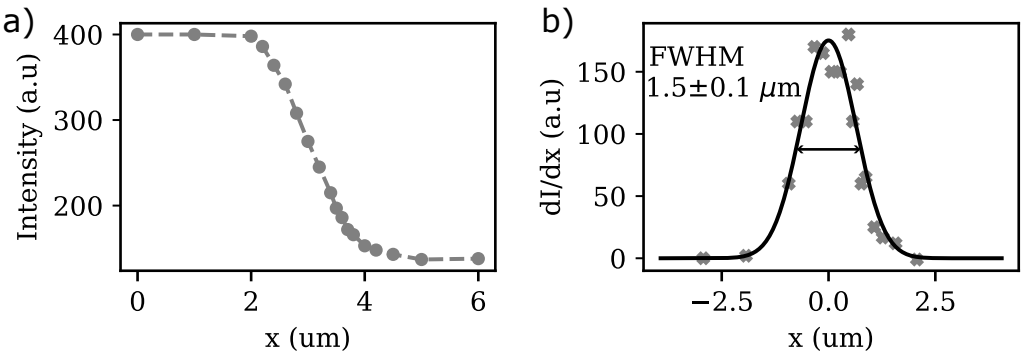

Figure 5.2: a) Reflected light intensity as a function of the probe beam position relative to the edge of the gold marker. b) Intensity profile of the probe beam, in the focus position, calculated with the numerical derivation of a).

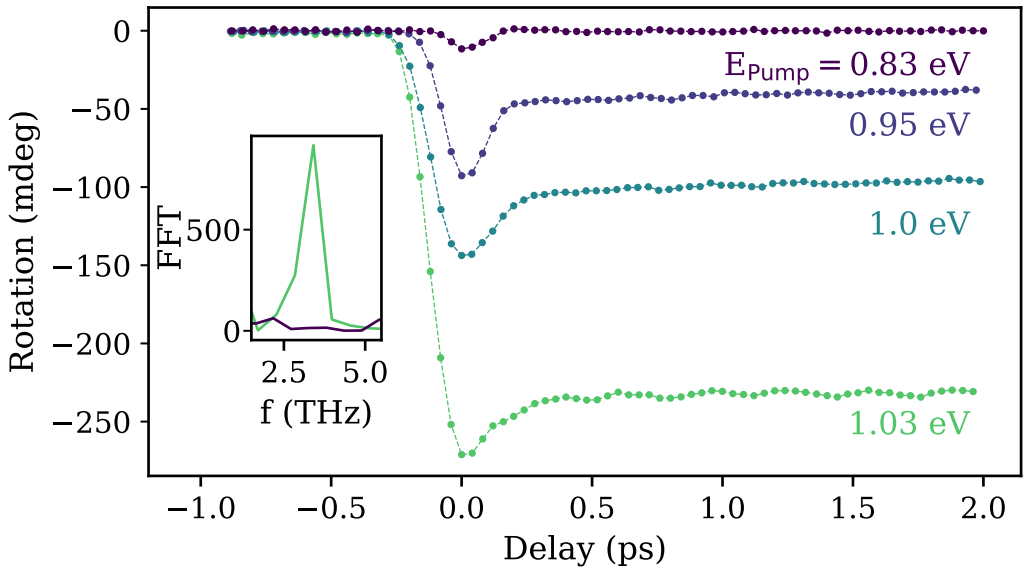

Figure 5.3: Pump-probe traces from $FePS_3$ on a SiO/Si substrate at $T = 10\,\mathrm{K}$. Inset: Fast Fourier transformation for excitation energies at E_{Ph}=1.03 eV (green) and E_{Ph}=0.83 eV (purple).

for energies below (see inset Fig.5.3). The 4.8 THz phonon mode visible in the bulk sample is not observed in the flake sample.

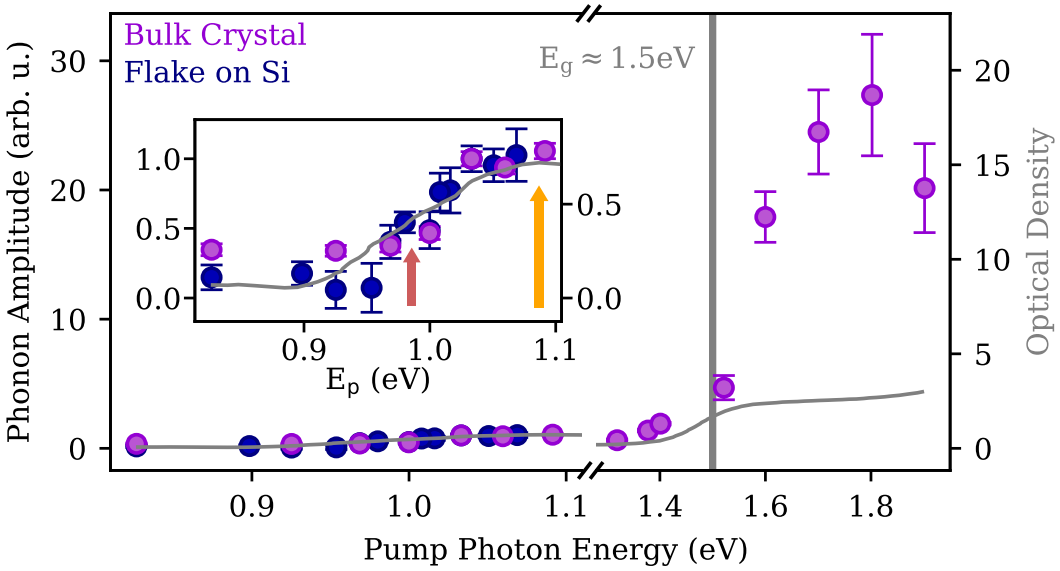

Figure 5.4: The amplitude of the 3.2 THz signal in the flake sample (blue markers) is being compared to the signal obtained from the bulk crystal (purple). Both datasets were measured at a temperature of 10 K and normalized to the value at 1.03 eV. Additionally, the grey curve represents the optical absorption of $FePS_3$, as measured in reference [101]. The red and orange arrows indicate the positions of the crystal-field split *d-d* transitions. Adapted from Ref.[24].

We apply the fitting procedure described in chapter 4, excluding the term for the missing 4.8 THz contribution. Figure 5.4 shows the amplitude of the 3.2 THz phonon mode as a function of the pump photon energy in direct comparison with the phonon amplitude detected in the bulk crystal. For a better comparison, the phonon amplitudes are normalized to the value at E_p=1.03 eV. Both samples exhibit identical behavior, with the phonon amplitude tracking the electronic features of $FePS_3$. For both specimens, the amplitude is increased at the position of the two *d-d* transitions. Therefore, the excitation of crystal-split electronic states has proven to be a legitimate lever for generating coherent phonon modes in flake samples. It holds significant importance, as it allows the utilization of photon energies below the band gap, which is crucial to reduce the amount of light-induced thermal heating and, therefore, thermal damage to the low-dimensional structures.

5.3 Temperature dependence

We measure the temperature dependence of the pump-induced polarization rotation in the flake sample, starting from $T = 10\,\mathrm{K}$ up to room temperature. Relying on the results from section 5.2, two complete sets of the experiment are performed with different pump-photon energies, corresponding to the two interband *d-d* transitions at 1.03 eV and 0.98 eV. For each temperature increment the z-position of the translation stage in the cryostat is adjusted to compensate the thermal expansion of the cold-finger and to keep the sample in the focal plane. Lateral movements of the sample are exlcuded by comparing the microscope image on the camera to a reference image taken at T =10 K . A selection of pump-probe traces for an excitation energy of E_{ph}=1.03 eV is shown in Figure 5.5. The pump-probe experiments on the flake revealed the exact behavior of the zone-folded phonon mode and the incoherent background as it was observed in the bulk sample. For both sets of excitation energies, the amplitude of the phonon mode and the incoherent background vanish as the sample temperature T exceeds the magnetic transition temperature ($T_N \approx 118\,\mathrm{K}$).

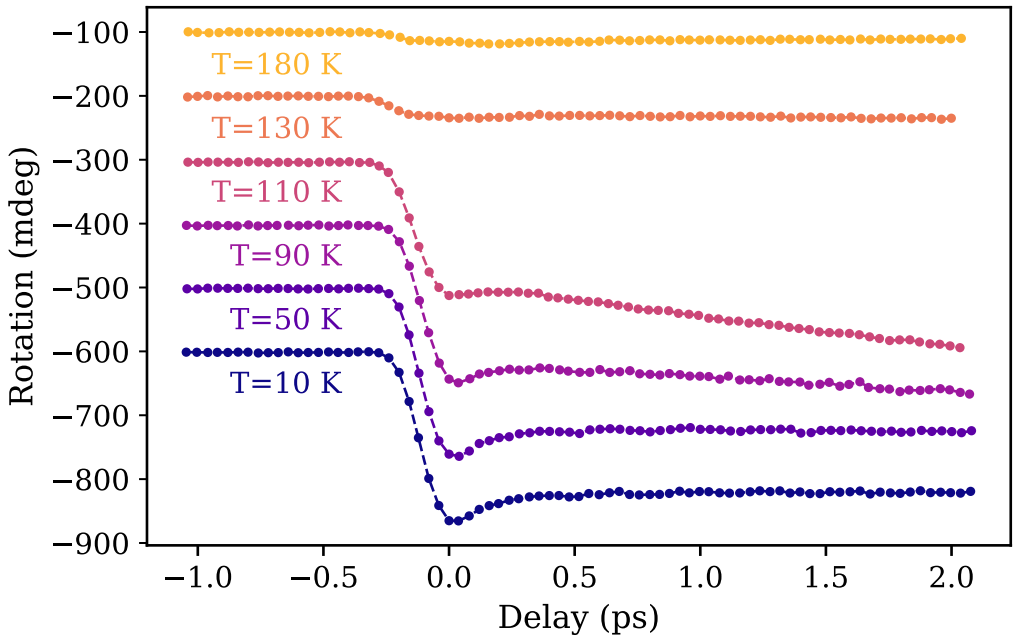

Figure 5.5: Transient rotation of the probe polarization for different sample temperatures at an excitation energy of 1.03 eV. A rotation offset is applied for comparison purposes.

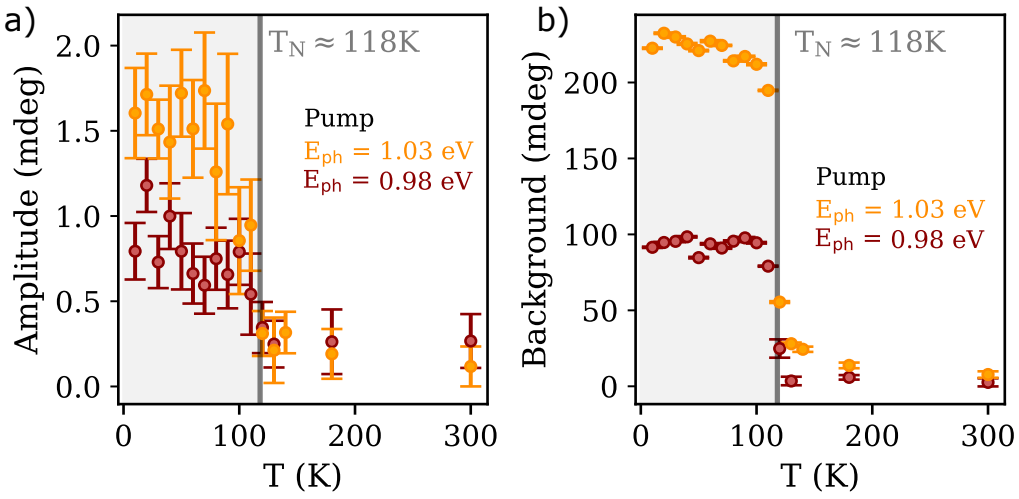

Figure 5.6: a) Phonon amplitude in the transient rotational signal of flake $FePS_3$ as a function of the sample temperature for pump photon energies of 1.03 eV (orange) and 0.98 eV (red). b) Temperature dependence of the incoherent background contribution for the same set of the photon energies. The errorbars do not exceed the marker size. Taken from Ref.[24].

Critical slow-down

The description of the demagnetization dynamics in $FePS_3$, or semiconductors and insulators in general, differs from the typical three-temperature model applied for metals, as presented in chapter 3. In contrast to metals, the magnetic moments in $FePS_3$ are bound by the localized Fe^{2+} ions. The optical excitation of the localized electrons and their recombinations within 100 ps transfers energy to the lattice system via the generation of phonon cascades. As a consequence, the spin-lattice coupling heats the spin system, reducing the antiferromagnetic order parameter [45, 94, 115].

Here, we have a closer look at the demagnetization dynamics in $FePS_3$ on a larger timescale (2000 ps), as shown in figure 5.7 for $T = 10$ K and $T = 115$ K, which is just below the Néel temperature of $T_N = 120$ K. It can be seen that the maximum quenching of the magnetic order is reached only after about 400 ps at 115 K and is reached after less than one picosecond at $T = 10$ K (see Fig.5.5). In the previous parts, we already mentioned an increase in the timescales of the incoherent magnetization dynamics close to the Néel temperature but only resolved their onset. This effect of a critical spin dynamic slowdown has already been observed and discussed in the two Ising type antiferromagnets within the MPS_3 group, $FePS_3$ [22, 32] and

$NiPS_3$ [45]. Here it is outlined in order to understand the previous temperature-dependent data better. The spin-lattice interaction is the dominating channel of energy transfer. Moreover, the specific heat of the spin subsystem in an Ising-system shows a critical behavior near the phase transition as it was also experimentally and theoretically confirmed for $FePS_3$[116]. Therefore, the characteristic timescales of the demagnetization dynamics are expected to follow the same divergence as the magnetic specific heat [32].

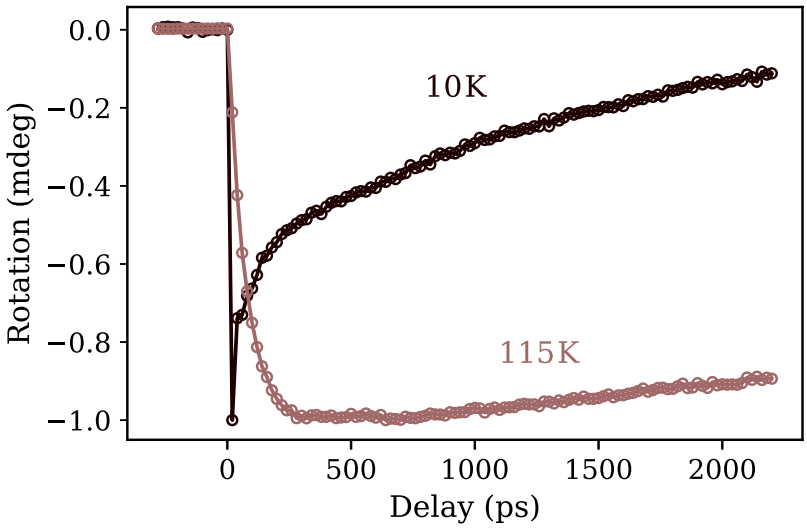

Figure 5.7: Time traces with long scan ranges at T=10 K (black) and T=115 K (brown), normalized to one. It is evident that the characteristic timescales of the magnetization quenching increase at the higher temperature.

5.4 Flake degradation

Exfoliated flake samples are known to be sensitive to ambient conditions. Here, we discuss the degradation caused by ambient air, and how far it can be reduced by a covering layer shielding the $FePS_3$ surface from oxygen. Therefore, we selected a flake of $FePS_3$, which was partially covered by an h-BN layer (hexagonal boron nitride). At a temperature of T =10 K, we measure the pump-probe signal on two different flake positions. The first position is fully exposed to the ambient atmosphere, while the second position is covered by h-BN. The results are shown in figure 5.8. Approximately one year has passed between the sample's fabrication and this measurement. The sample was stored in a desiccator in a nitrogen atmosphere

or a vacuum during this time. While the covered part of the sample still shows a clear transient signal in the magnetic linear dichroism caused by light-induced demagnetization, the uncovered part does not show any explicit dynamical behavior. A magneto-optical signal appears only at the position of temporal overlap between the pump and probe beam. This clearly shows that as the dimensionality is further reduced, the sample degradation is a critical experimental challenge, which can be reduced in its effect by the capping layer of h-BN.

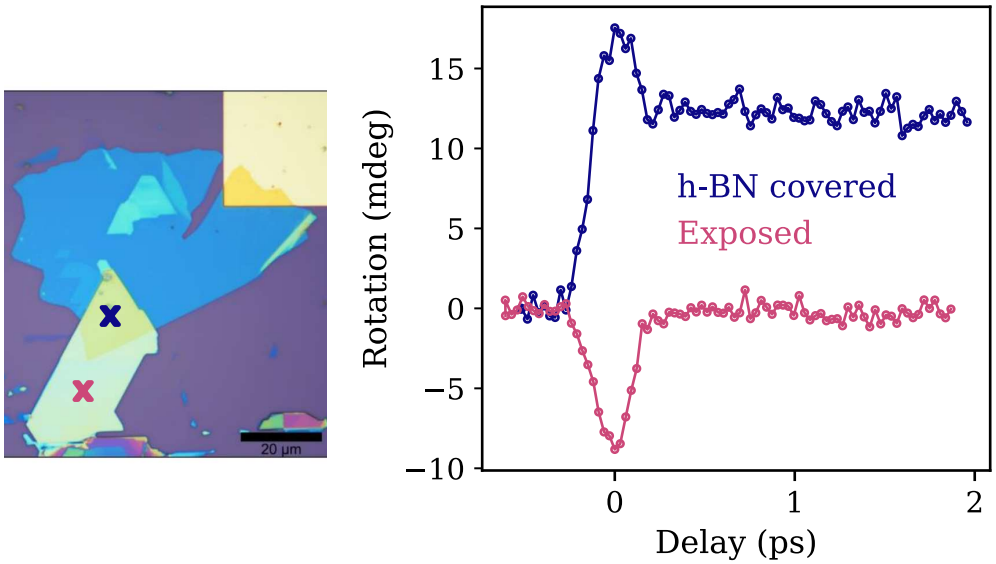

Figure 5.8: a) Partially h-BN covered $FePS_3$ flake. The marked areas are used for the time resolved experiments. b) Pump-probe traces measured on the corresponding marked areas.

5.5 Conclusion

We successfully applied the findings about the coherent phonon excitation from the bulk sample to the exfoliated flake on a SiO/Si substrate. The dimensions of the 377 nm flake were measured via atomic force microscopy in the tapping mode. For the pump-probe experiments, the collinear setup with an achromatic microscope objective of 50x amplification was employed and could detect the pump-induced variations of the magnetic linear dichroism. The pump photon energy dependence of the 3.2 THz phonon mode is consistent with the results from the single crystal sample. In the temperature-dependent pump-probe measurement, the observation

of the zone-folded origin of the phonon modes was reproduced via the excitation of the sub-bandgap *d-d* transitions at 1.03 eV and 0.98 eV.

We thus demonstrated the successful excitation and observation of a coherent lattice mode, closely related to the antiferromagnetic order, in a flake sample. It demonstrated the scalability of the findings from chapter 4, a significant step in the miniaturization of the optical magnetization control.

6 Conclusion

In conclusion, the research presented in this thesis lays a path toward the optical, ultrafast control of spins in magnetically ordered 2D materials. Additionally, we have successfully developed a state-of-the-art optical setup, adaptable for a wide range of antiferromagnetic semiconductors and insulators.

The ultrafast light-induced-demagnetization in the prototypical $3d$ ferromagnet cobalt was used to set a benchmark for the system and its sensitivity. Furthermore, we have explored the lattice and spin dynamics in the exfoliateable van der Waals antiferromagnet $FePS_3$ in bulk and flake form. $FePS_3$ is a promising member of the MPS_3 (M = transition metal) material family, in which the selection of the transition metal can tune magnetic and electronic properties. In the specific case of M = Fe, the magnetization upholds even down to the monolayer. In $FePS_3$, we could establish a close relation between a phonon mode and the magnetic order of the system, finally using it to generate coherent spin dynamics.

The magneto-optical pump-probe setup, characterized by its broad spectral range (0.5 eV-3.5 eV), high modulation rate, and single-pulse detection, can apply high magnetic and electric fields. The laser system is designed to excite and probe dynamics at different electronic transitions in a broad range of photon energies with laser pulses of 100 fs duration or less. The detection method, containing the combined use of an electro-optical modulator and a high-frequency digitizer, makes the single light pulses accessible while maintaining the highest possible modulation frequency and high sensitivity. The self-programmed experimental software, designed in Python, ensures minimal computational time impact. With the ability to apply large magnetic fields up to $\mu_0 H = \pm 9\,\mathrm{T}$ and control the sample temperature in a range between $4-420\,\mathrm{K}$. Furthermore, the system was designed with the adaptability to microscope objectives, which allow for a laser spot down to 1.5 µm, and thus, for probing the magnetic phenomena locally.

The system's capability is experimentally proven by studying the ultrafast light-induced magnetization quenching in a cobalt single crystal. The widely studied demagnetization mechanism and the typically high rotational signal that can be retrieved from the Kerr rotation in a ferromagnet make it a suitable test environment. The leading free experimental parameters (photon energy, magnetic field, temperature, fluence) were explored, giving insight into the demagnetization dynamics of

cobalt and the capabilities of each subsystem. The experimental setup displayed state-of-the-art sensitivity, capable of detecting a polarization rotation as small as 50 µdeg.

We performed magneto-optical experiments on the antiferromagnetic van der Waals semiconductor $FePS_3$ and studied the close relation between the lattice dynamics and the magnetic order. We optically excitated two lattice modes at 3.2 THz and 4.8 THz. The temperature dependence of the phonon modes revealed their zone-folded origin, as both modes vanish above T_N. In $FePS_3$, the unit cell differs between the disordered and the magnetically ordered state, consequently changing the Brillouin zone and the phonon-dispersion. Only in the antiferromagnetic state are the two lattice modes optically active.

By tuning the excitation photon energy, we could observe a relation between the two phonon amplitudes and electronic transitions, leading to the conclusion that the displacive excitation of coherent phonons is the excitation process. Moreover, it revealed that exciting a crystal field split *d*-*d* transition allows for an efficient phonon excitation while maintaining a long phonon lifetime due to low heating.

The probe polarization dependence revealed the interaction between the magneto-optical effect and the phonon modes. The zig-zag structure of the in-plane antiferromagnetic order creates an optical anisotropy, preferring the absorption for polarizations along a defined axis, which is the source for magnetic linear dichroism. As the phonon oscillation modulates the zig-zag pattern, they also modulate the magnitude of the linear dichroism and become visible as a rotation of the polarization of the probe and as a variation in the reflectivity.

We observe the evolution of phonon-induced oscillations at late delays to precisely monitor the phonon frequency at externally applied magnetic fields. Under the influence of the external field, we achieve the optical excitation of a hybridized phonon magnon mode and detect the phononic contributions of the upper and lower branches of the phononic contribution. Thus, we could demonstrate the excitation of coherent magnetic excitations via the excitation and detection process of the zone-folded phonon mode.

The findings within the bulk $FePS_3$ sample can also be applied to thinner specimens. We adapt the system to use a microscope objective and investigate a 380 nm thick flake of $FePS_3$ on a SiO_2/Si substrate. By exciting the same *d*-*d* transition it is possible to pump below the band gap and avoid thermal damage on the flake and the disruptive excitation of free electrons from the Si substrate. The excitation of the phonon mode in the flake sample proves the scalability of our approach. The pump photon energy dependence and the temperature dependence of the mode confirm the same relation with the phonon mode as demonstrated in the bulk crystal.

The findings of this thesis show a close interaction between the lattice modes and the magnetization in $FePS_3$. The zone-folded lattice modes can only be optically excited within the magnetically ordered state and can thus function as a probe of the magnetization. Moreover, the coherent excitation of the hybridized phonon magnon mode offers a new possibility for controlling magnetism on the terahertz timescale, which could be exploited in photo-magnonic spintronic devices.

From a fundamental point of view, scaling down to single atomic layers of $FePS_3$ can be a first step towards understanding magnetization dynamics in the two-dimensional limit. For this, the demonstrated phono-magnonic dynamics and coherent lattice dynamics in the flake sample can be used as a starting point. Moreover, one remaining hurdle is the small signal expected from mono or few-layer samples. A recent study has revealed the spectral dependence of the magnetic linear dichroism and the possibility of enhancing the magneto-optical effect with optical cavities [47]. The tunability of the probe beam can be used to probe in an area that shows especially strong dichroism, possibly within the resonance of a flake-substrate cavity. Furthermore, the low necessary laser power allows for a further increase of the laser repetition rate up to 1 MHz, increasing the collected statistic and thus the sensitivity of the system.

Appendix

Static Kerr rotation in Fe_2GeTe_2

We use a flake sample from the van der Waals ferromagnet Fe_2GeTe_2 (FGT) placed on a SiO/Si substrate to demonstrate the detection of static magnetization curves on a flake sample with a strong out-of-plane anisotropy [92, 93]. From comparing the microscopic image to other flakes, the thickness is estimated to lie in the order of 100 nm. The setup is switched into the configuration described in section 2.7, with the microscope objective replaced by a nonmagnetic model by Olympus with a numerical aperture of NA=0.25 and 10x magnification. The objective is fixed by a threaded aluminum plate and mounted directly into the bore of the magnet. The layout is capable of imaging the sample (see Fig. 6.1 a)) and the probe is focused on the flake. Figure 6.1 b) shows the hysteresis loop, detected via the Kerr rotation, revealing the distinct coercivity and remanence of the FGT flake.

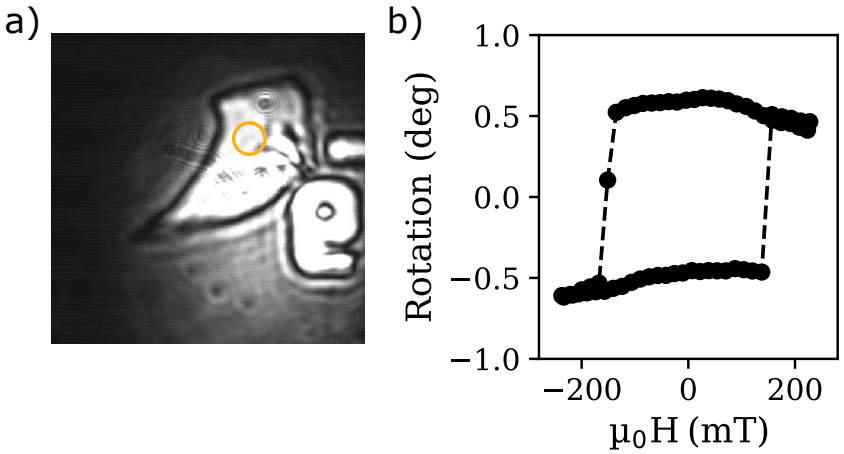

Figure 6.1: a)Optical image of the flake, taken inside the setup. The orange circle marks the focus position of the laser. The structure on the bottom right is a gold marker on the substrate. b) Hysteresis loop of the FGT flake sample, measured via the static, field-dependent Kerr rotation.

Pump polarization dependence in $FePS_3$

Figure 6.2 shows the pump polarization dependence of the 3.2 THz and 4.8 THz zone-folded phonon modes in the bulk $FePS_3$ sample. The phonon amplitude shows a clear π periodicity, consistent with the symmetry of the magnetized ab plane. Pump and probe are linearly polarized and the photon energies are set to $E_{\text{Probe}} = 1.45\,\text{eV}$ and $E_{\text{Pump}} = 1.03\,\text{eV}$. The sample is cooled down to 10 K.

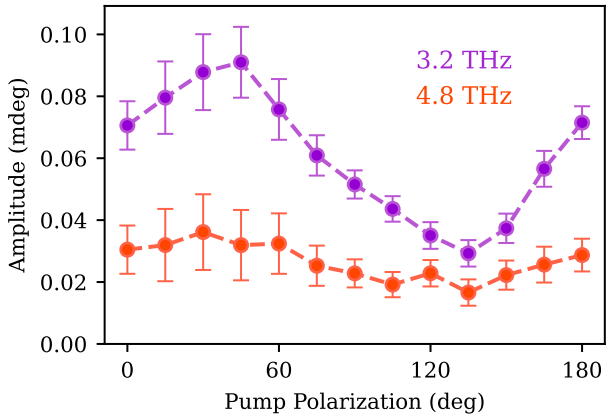

Figure 6.2: The phonon amplitudes of the 3.2 THz and 4.8 THz phonon modes as a function of the probe polarization.

Bibliography

[1] N Bloembergen and Pierce Hall. "From Nanosecond to Femtosecond Science." In: *Rev. Mod. Phys.* 71.2 (1999).

[2] E. Beaurepaire, J.-C. Merle, A. Daunois, and J.-Y. Bigot. "Ultrafast Spin Dynamics in Ferromagnetic Nickel." In: *Physical Review Letters* 76.22 (1996), pp. 4250–4253. DOI: 10.1103/PhysRevLett.76.4250.

[3] P Nemec, M Fiebig, T Kampfrath, and A V Kimel. "Antiferromagnetic Opto-Spintronics." In: *Nature Physics* 14.3 (2018), pp. 229–241. DOI: 10.1038/s41567-018-0051-x.

[4] Zeyuan Sun, Yangfan Yi, Tiancheng Song, et al. "Giant Nonreciprocal Second-Harmonic Generation from Antiferromagnetic Bilayer CrI3." In: *Nature* 572.7770 (2019), pp. 497–501. DOI: 10.1038/s41586-019-1445-3.

[5] C Manzoni and G Cerullo. "Design Criteria for Ultrafast Optical Parametric Amplifiers." In: *Journal of Optics* 18.10 (2016), p. 103501. DOI: 10.1088/2040-8978/18/10/103501.

[6] F. Mertens, M. Terschanski, D. Mönkebüscher, S. Ponzoni, D. Bossini, and M. Cinchetti. "Wide Spectral Range Ultrafast Pump–Probe Magneto-Optical Spectrometer at Low Temperature, High-Magnetic and Electric Fields." In: *Review of Scientific Instruments* 91.11 (2020), p. 113001. DOI: 10.1063/5.0024449.

[7] D. Bossini, S. Dal Conte, M. Terschanski, et al. "Femtosecond Phononic Coupling to Both Spins and Charges in a Room-Temperature Antiferromagnetic Semiconductor." In: *Physical Review B* 104.22 (2021), p. 224424. DOI: 10.1103/PhysRevB.104.224424.

[8] T. F. Nova, A. Cartella, A. Cantaluppi, M. Först, D. Bossini, R. V. Mikhaylovskiy, A. V. Kimel, R. Merlin, and A. Cavalleri. "An Effective Magnetic Field from Optically Driven Phonons." In: *Nature Physics* 13.2 (2017), pp. 132–136. DOI: 10.1038/nphys3925.

[9] D. Bossini, A. M. Kalashnikova, R. V. Pisarev, Th. Rasing, and A. V. Kimel. "Controlling Coherent and Incoherent Spin Dynamics by Steering the Photoinduced Energy Flow." In: *Physical Review B* 89.6 (2014), p. 060405. DOI: 10.1103/PhysRevB.89.060405.

[10] U. Parlak, R. Adam, D. E. Bürgler, S. Gang, and C. M. Schneider. "Optically Induced Magnetization Reversal in [Co / Pt] N Multilayers: Role of Domain Wall Dynamics." In: *Physical Review B* 98.21 (2018), p. 214443. DOI: 10.1103/PhysRevB.98.214443.

[11] A Stupakiewicz, K Szerenos, D Afanasiev, A Kirilyuk, and A V Kimel. "Ultrafast Nonthermal Photo-Magnetic Recording in a Transparent Medium." In: *Nature* 542 (2017), p. 71. DOI: 10.1038/nature20807.

[12] Sebastian Manz, Masakazu Matsubara, Thomas Lottermoser, Jonathan Büchi, Ayato Iyama, Tsuyoshi Kimura, Dennis Meier, and Manfred Fiebig. "Reversible Optical Switching of Antiferromagnetism in TbMnO3." In: *Nature Photonics* 10.10 (2016), pp. 653–656. DOI: 10.1038/nphoton.2016.146.

[13] K. S. Novoselov, A. K. Geim, S. V. Morozov, D. Jiang, Y. Zhang, S. V. Dubonos, I. V. Grigorieva, and A. A. Firsov. "Electric Field Effect in Atomically Thin Carbon Films." In: *Science* 306.5696 (2004), pp. 666–669. DOI: 10.1126/science.1102896.

[14] Kenneth S. Burch, David Mandrus, and Je-Geun Park. "Magnetism in Two-Dimensional van Der Waals Materials." In: *Nature* 563.7729 (2018), pp. 47–52. DOI: 10.1038/s41586-018-0631-z.

[15] Meng-Chien Wang, Che-Chun Huang, Chi-Ho Cheung, et al. "Prospects and Opportunities of 2D van Der Waals Magnetic Systems." In: *Annalen der Physik* 532.5 (2020), p. 1900452. DOI: 10.1002/andp.201900452.

[16] Hyunsoo Yang, Sergio O. Valenzuela, Mairbek Chshiev, et al. "Two-Dimensional Materials Prospects for Non-Volatile Spintronic Memories." In: *Nature* 606.7915 (2022), pp. 663–673. DOI: 10.1038/s41586-022-04768-0.

[17] M. Gibertini, M. Koperski, A. F. Morpurgo, and K. S. Novoselov. "Magnetic 2D Materials and Heterostructures." In: *Nature Nanotechnology* 14.5 (2019), pp. 408–419. DOI: 10.1038/s41565-019-0438-6.

[18] S. Calder, A. V. Haglund, A. I. Kolesnikov, and D. Mandrus. "Magnetic Exchange Interactions in the van Der Waals Layered Antiferromagnet Mn P Se 3." In: *Physical Review B* 103.2 (2021), p. 024414. DOI: 10.1103/PhysRevB.103.024414.

[19] Gen Long, Hugo Henck, Marco Gibertini, Dumitru Dumcenco, Zhe Wang, Takashi Taniguchi, Kenji Watanabe, Enrico Giannini, and Alberto F. Morpurgo. "Persistence of Magnetism in Atomically Thin MnPS3 Crystals." In: *Nano Letters* 20.4 (2020), pp. 2452–2459. DOI: 10.1021/acs.nanolett.9b05165.

[20] Kangwon Kim, Soo Yeon Lim, Jae-Ung Lee, et al. "Suppression of Magnetic Ordering in XXZ-type Antiferromagnetic Monolayer NiPS3." In: *Nature Communications* 10.1 (2019), p. 345. DOI: 10.1038/s41467-018-08284-6.

[21] Matthew J. Coak, David M. Jarvis, Hayrullo Hamidov, et al. "Emergent Magnetic Phases in Pressure-Tuned van Der Waals Antiferromagnet FePS3." In: *Physical Review X* 11.1 (2021), p. 011024. DOI: 10.1103/PhysRevX.11.011024.

[22] Faran Zhou, Kyle Hwangbo, Qi Zhang, et al. "Dynamical Criticality of Spin-Shear Coupling in van Der Waals Antiferromagnets." In: *Nature Communications* 13.1 (2022), p. 6598. DOI: 10.1038/s41467-022-34376-5.

[23] D. Afanasiev, B. A. Ivanov, A. Kirilyuk, Th. Rasing, R. V. Pisarev, and A. V. Kimel. "Control of the Ultrafast Photoinduced Magnetization across the Morin Transition in DyFeO 3." In: *Physical Review Letters* 116.9 (2016), p. 097401. DOI: 10.1103/PhysRevLett.116.097401.

[24] Fabian Mertens, David Mönkebüscher, Umut Parlak, et al. "Ultrafast Coherent THz Lattice Dynamics Coupled to Spins in the van Der Waals Antiferromagnet FePS3." In: *Advanced Materials* 35.6 (2023), p. 2208355. DOI: 10.1002/adma.202208355.

[25] Wassen Mohammad, Adel Elomri, and Laoucine Kerbache. "The Global Semiconductor Chip Shortage: Causes, Implications, and Potential Remedies." In: *IFAC-PapersOnLine*. 10th IFAC Conference on Manufacturing Modelling, Management and Control MIM 2022 55.10 (2022), pp. 476–483. DOI: 10.1016/j.ifacol.2022.09.439.

[26] J M D Coey. *Magnetism and Magnetic Materials*. Cambridge University Press, 2010.

[27] Joachim Stöhr and Hans Christoph Siegmann. *Magnetism: From Fundamentals to Nanoscale Dynamics*. Springer Series in Solid-State Sciences 152. Berlin ; New York: Springer, 2006.

[28] A. V. Kimel, A. Kirilyuk, A. Tsvetkov, R. V. Pisarev, and Th Rasing. "Laser-Induced Ultrafast Spin Reorientation in the Antiferromagnet TmFeO3." In: *Nature* 429.6994 (2004), pp. 850–853. DOI: 10.1038/nature02659.

[29] Kannan M. Krishnan. *Fundamentals and Applications of Magnetic Materials*. First edition. Oxford, United Kingdom: Oxford University Press, 2016.

[30] Qing Hua Wang, Amilcar Bedoya-Pinto, Mark Blei, et al. "The Magnetic Genome of Two-Dimensional van Der Waals Materials." In: *ACS Nano* 16.5 (2022), pp. 6960–7079. DOI: 10.1021/acsnano.1c09150.

[31] Amikam Aharoni. *Introduction to the Theory of Ferromagnetism*. 2nd ed. Oxford Science Publications, 2001.

[32] Xiao-Xiao Zhang, Shengwei Jiang, Jinhwan Lee, Changgu Lee, Kin Fai Mak, and Jie Shan. "Spin Dynamics Slowdown near the Antiferromagnetic Critical Point in Atomically Thin FePS3." In: *Nano Letters* 21.12 (2021), pp. 5045–5052. DOI: 10.1021/acs.nanolett.1c00870.

[33] Rudolf Gross and Achim Marx. *Festkörperphysik, Gross*. München: Oldenbourg, 2012.

[34] J. M. D. Coey and Stuart S.P. Parkin, eds. *Handbook of Magnetism and Magnetic Materials*. Cham: Springer International Publishing, 2021. DOI: 10.1007/978-3-030-63210-6.

[35] D. Lançon, H. C. Walker, E. Ressouche, B. Ouladdiaf, K. C. Rule, G. J. McIntyre, T. J. Hicks, H. M. Rønnow, and A. R. Wildes. "Magnetic Structure and Magnon Dynamics of the Quasi-Two-Dimensional Antiferromagnet FePS 3." In: *Physical Review B* 94.21 (2016), p. 214407. DOI: 10.1103/PhysRevB.94.214407.

[36] Maria Ramos, Felix Carrascoso, Riccardo Frisenda, et al. "Ultra-Broad Spectral Photo-Response in FePS3 Air-Stable Devices." In: *npj 2D Materials and Applications* 5.1 (2021), pp. 1–9. DOI: 10.1038/s41699-021-00199-z.

[37] Hui Li, Shuangchen Ruan, and Yu-Jia Zeng. "Intrinsic Van Der Waals Magnetic Materials from Bulk to the 2D Limit: New Frontiers of Spintronics." In: *Advanced Materials* 31.27 (2019), p. 1900065. DOI: 10.1002/adma.201900065.

[38] N. D. Mermin and H. Wagner. "Absence of Ferromagnetism or Antiferromagnetism in One- or Two-Dimensional Isotropic Heisenberg Models." In: *Physical Review Letters* 17.22 (1966), pp. 1133–1136. DOI: 10.1103/PhysRevLett.17.1133.

[39] Jae-Ung Lee, Sungmin Lee, Ji Hoon Ryoo, Soonmin Kang, Tae Yun Kim, Pilkwang Kim, Cheol-Hwan Park, Je-Geun Park, and Hyeonsik Cheong. "Ising-Type Magnetic Ordering in Atomically Thin FePS $_3$." In: *Nano Letters* 16.12 (2016), pp. 7433–7438. DOI: 10.1021/acs.nanolett.6b03052.

[40] Sarah Jenkins, Levente Rózsa, Unai Atxitia, Richard F. L. Evans, Kostya S. Novoselov, and Elton J. G. Santos. "Breaking through the Mermin-Wagner Limit in 2D van Der Waals Magnets." In: *Nature Communications* 13.1 (2022), p. 6917. DOI: 10.1038/s41467-022-34389-0.

[41] Cheng Gong, Lin Li, Zhenglu Li, et al. "Discovery of Intrinsic Ferromagnetism in Two-Dimensional van Der Waals Crystals." In: *Nature* 546.7657 (2017), pp. 265–269. DOI: 10.1038/nature22060.

[42] Yinlu Gao, Xue Jiang, Zhiyong Qiu, and Jijun Zhao. "Photoexcitation Induced Magnetic Phase Transition and Spin Dynamics in Antiferromagnetic MnPS3 Monolayer." In: *npj Computational Materials* 9.1 (2023), pp. 1–7. DOI: 10.1038/s41524-023-01071-y.

[43] Bevin Huang, Genevieve Clark, Efrén Navarro-Moratalla, et al. "Layer-Dependent Ferromagnetism in a van Der Waals Crystal down to the Monolayer Limit." In: *Nature* 546.7657 (2017), pp. 270–273. DOI: 10.1038/nature22391.

[44] Yujun Deng, Yijun Yu, Yichen Song, et al. "Gate-Tunable Room-Temperature Ferromagnetism in Two-Dimensional Fe3GeTe2." In: *Nature* 563.7729 (2018), pp. 94–99. DOI: 10.1038/s41586-018-0626-9.

[45] D. Khusyainov, T. Gareev, V. Radovskaia, et al. "Ultrafast Laser-Induced Spin–Lattice Dynamics in the van Der Waals Antiferromagnet CoPS3." In: *APL Materials* 11.7 (2023), p. 071104. DOI: 10.1063/5.0146128.

[46] Qi Zhang, Kyle Hwangbo, Chong Wang, Qianni Jiang, Jiun-Haw Chu, Haidan Wen, Di Xiao, and Xiaodong Xu. "Observation of Giant Optical Linear Dichroism in a Zigzag Antiferromagnet FePS3." In: *Nano Letters* 21.16 (2021), pp. 6938–6945. DOI: 10.1021/acs.nanolett.1c02188.

[47] Huiqin Zhang, Zhuoliang Ni, Christopher E. Stevens, Aofeng Bai, Frank Peiris, Joshua R. Hendrickson, Liang Wu, and Deep Jariwala. "Cavity-Enhanced Linear Dichroism in a van Der Waals Antiferromagnet." In: *Nature Photonics* 16.4 (2022), pp. 311–317. DOI: 10.1038/s41566-022-00970-8.

[48] Carla Boix-Constant, Samuel Mañas-Valero, Alberto M. Ruiz, Andrey Rybakov, Krzysztof Aleksander Konieczny, Sébastien Pillet, José J. Baldoví, and Eugenio Coronado. "Probing the Spin Dimensionality in Single-Layer CrSBr van Der Waals Heterostructures by Magneto-Transport Measurements." In: *Advanced Materials* n/a.n/a (), p. 2204940. DOI: 10.1002/adma.202204940.

[49] P. A. Joy and S. Vasudevan. "Magnetism in the Layered Transition-Metal Thiophosphates M PS 3 (M =Mn, Fe, and Ni)." In: *Physical Review B* 46.9 (1992), pp. 5425–5433. DOI: 10.1103/PhysRevB.46.5425.

[50] R. Brec, D. M. Schleich, G. Ouvrard, A. Louisy, and J. Rouxel. "Physical Properties of Lithium Intercalation Compounds of the Layered Transition-Metal Chalcogenophosphites." In: *Inorganic Chemistry* 18.7 (1979), pp. 1814–1818. DOI: 10.1021/ic50197a018.

[51] Ramesh Naidu Jenjeti, Muthu P. Austeria, and Srinivasan Sampath. "Alternate to Molybdenum Disulfide: A 2D, Few-Layer Transition-Metal Thiophosphate and Its Hydrogen Evolution Reaction Activity over a Wide pH Range." In: *ChemElectroChem* 3.9 (2016), pp. 1392–1399. DOI: 10.1002/celc.201600235.

[52] Ke-zhao Du, Xing-zhi Wang, Yang Liu, Peng Hu, M. Iqbal Bakti Utama, Chee Kwan Gan, Qihua Xiong, and Christian Kloc. "Weak Van Der Waals Stacking, Wide-Range Band Gap, and Raman Study on Ultrathin Layers of Metal Phosphorus Trichalcogenides." In: *ACS Nano* 10.2 (2016), pp. 1738–1743. DOI: 10.1021/acsnano.5b05927.

[53] M. J. Coak, D. M. Jarvis, H. Hamidov, et al. "Tuning Dimensionality in Van-Der-Waals Antiferromagnetic Mott insulatorsTMPS3." In: *Journal of Physics: Condensed Matter* 32.12 (2019), p. 124003. DOI: 10.1088/1361-648X/ab5be8.

[54] K. Momma and F. Izumi. "VESTA 3 for Three-Dimensional Visualization of Crystal, Volumetric and Morphology Data." In: *Journal of Applied Crystallography* 44.6 (2011), pp. 1272–1276. DOI: 10.1107/S0021889811038970.

[55] Dmytro Afanasiev, Jorrit R. Hortensius, Mattias Matthiesen, et al. "Controlling the Anisotropy of a van Der Waals Antiferromagnet with Light." In: *Science Advances* 7.23 (2021), eabf3096. DOI: 10.1126/sciadv.abf3096.

[56] E. Ressouche, M. Loire, V. Simonet, R. Ballou, A. Stunault, and A. Wildes. "Magnetoelectric MnPS3 as a Candidate for Ferrotoroidicity." In: *Physical Review B* 82.10 (2010), p. 100408. DOI: 10.1103/PhysRevB.82.100408.

[57] Xingzhi Wang, Kezhao Du, Yu Yang Fredrik Liu, et al. "Raman Spectroscopy of Atomically Thin Two-Dimensional Magnetic Iron Phosphorus Trisulfide (FePS3) Crystals." In: *2D Materials* 3.3 (2016), p. 031009. DOI: 10.1088/2053-1583/3/3/031009.

[58] Amber McCreary, Jeffrey R. Simpson, Thuc T. Mai, Robert D. McMichael, Jason E. Douglas, Nicholas Butch, Cindi Dennis, Rolando Valdés Aguilar, and Angela R. Hight Walker. "Quasi-Two-Dimensional Magnon Identification in Antiferromagnetic FePS3 via Magneto-Raman Spectroscopy." In: *Physical Review B* 101.6 (2020), p. 064416. DOI: 10.1103/PhysRevB.101.064416.

[59] A. K. Zvezdin and V. A. Kotov. *Modern Magnetooptics and Magnetooptical Materials*. CRC Press, 1997.

[60] Katsuaki Sato and Takayuki Ishibashi. "Fundamentals of Magneto-Optical Spectroscopy." In: *Frontiers in Physics* 10 (2022), p. 946515. DOI: 10.3389/fphy.2022.946515.

[61] Z. Q. Qiu and S. D. Bader. "Surface Magneto-Optic Kerr Effect." In: *Review of Scientific Instruments* 71.3 (2000), pp. 1243–1255. DOI: 10.1063/1.1150496.

[62] "Magneto-Optic Effect, Faraday Effect, Kerr Effect, Polarization, Magnetoelectronics." In: *International Journal of Electromagnetics and Applications* (2017).

[63] Wolfgang Kuch, Rudolf Schäfer, Peter Fischer, and Franz Ulrich Hillebrecht. *Magnetic Microscopy of Layered Structures*. Vol. 57. Springer Series in Surface Sciences. Berlin, Heidelberg: Springer Berlin Heidelberg, 2015. DOI: 10.1007/978-3-662-44532-7.

[64] Tomoya Higo, Huiyuan Man, Daniel B. Gopman, et al. "Large Magneto-Optical Kerr Effect and Imaging of Magnetic Octupole Domains in an Antiferromagnetic Metal." In: *Nature Photonics* 12.2 (2018), pp. 73–78. DOI: 10.1038/s41566-017-0086-z.

[65] Kisung Kang, Kexin Yang, Krithik Puthalath, David G. Cahill, and André Schleife. "Polar Magneto-Optical Kerr Effect in Antiferromagnetic M 2 As (M = Cr , Mn , Fe) under an External Magnetic Field." In: *Physical Review B* 105.18 (2022), p. 184404. DOI: 10.1103/PhysRevB.105.184404.

[66] H.-Ch. Mertins, P. M. Oppeneer, J. Kuneš, A. Gaupp, D. Abramsohn, and F. Schäfers. "Observation of the X-Ray Magneto-Optical Voigt Effect." In: *Physical Review Letters* 87.4 (2001), p. 047401. DOI: 10.1103/PhysRevLett.87.047401.

[67] Tobias Kampfrath, Alexander Sell, Gregor Klatt, et al. "Coherent Terahertz Control of Antiferromagnetic Spin Waves." In: *Nature Photonics* 5.1 (2011), pp. 31–34. DOI: 10.1038/nphoton.2010.259.

[68] Marc Terschanski. "Phononkopplung an Spins und Ladungen auf der ultraschnellen Zeitskala im antiferromagnetischen Halbleiter MnTe." In: ().

[69] Galan Moody, John Schaibley, and Xiaodong Xu. "Exciton Dynamics in Monolayer Transition Metal Dichalcogenides." In: *Journal of the Optical Society of America B* 33.7 (2016), p. C39. DOI: 10.1364/JOSAB.33.000C39.

[70] Alexander O. Goushcha and Bernd Tabbert. "On Response Time of Semiconductor Photodiodes." In: *Optical Engineering* 56.9 (2017), p. 097101. DOI: 10.1117/1.OE.56.9.097101.

[71] R. Baumgartner and R. Byer. "Optical Parametric Amplification." In: *IEEE Journal of Quantum Electronics* 15.6 (1979), pp. 432–444. DOI: 10.1109/JQE.1979.1070043.

[72] Kuo-Chen Lang and Hui-Kang Teng. "Optical Balanced Detection in Heterodyne Interferometric Ellipsometry." In: *Applied Optics* 54.27 (2015), pp. 8108–8115. DOI: 10.1364/AO.54.008108.

[73] James R. P. Bain, Michael Lengden, George Stewart, and Walter Johnstone. "Recovery of Absolute Absorption Line Shapes in Tunable Diode Laser Spectroscopy Using External Amplitude Modulation With Balanced Detection." In: *IEEE Sensors Journal* 16.3 (2016), pp. 675–680. DOI: 10.1109/JSEN.2015.2489929.

[74] Christopher A. Werley, Stephanie M. Teo, and Keith A. Nelson. "Pulsed Laser Noise Analysis and Pump-Probe Signal Detection with a Data Acquisition Card." In: *Review of Scientific Instruments* 82.12 (2011), p. 123108. DOI: 10.1063/1.3669783.

[75] Herman Hinsch. *Elektronik. Ein Werkzeug für Naturwissenschaftler*. 9. Auflage. Springer, 1996.

[76] Fabian Mertens. *Optical and Magneto-Optical Investigation of Magneto-Electric Cr2O3*. Master Thesis. 2018.

[77] Zhizhen Ma, Zhuoran Li, Ke Liu, Chenran Ye, and Volker J. Sorger. "Indium-Tin-Oxide for High-performance Electro-optic Modulation." In: *Nanophotonics* 4.2 (2015), pp. 198–213. DOI: 10.1515/nanoph-2015-0006.

[78] Sabine Lenz and Marlene Thaler. *Grundlagen der Licht- und Elektronenmikroskopie*. Ed. by Alexander Linnemann and Susanne Kühl. UTB Biologie Medizin Molekularbiologie Ernährungs-/Lebensmittelwissenschaften 4864. Stuttgart: UTB, 2018.

[79] Wolfgang Demtröder. *Experimentalphysik 2*. Springer-Lehrbuch. Berlin, Heidelberg: Springer Berlin Heidelberg, 2017. DOI: 10.1007/978-3-662-55790-7.

[80] Marie Krečmarová, Daniel Andres-Penares, Ladislav Fekete, et al. "Optical Contrast and Raman Spectroscopy Techniques Applied to Few-Layer 2D Hexagonal Boron Nitride." In: *Nanomaterials* 9.7 (2019), p. 1047. DOI: 10.3390/nano9071047.

[81] D Weller, G R Harp, R F C Farrow, A Cebollada, and J Sticht. "Orientation Dependence of the Polar Kerr Effect in Fcc and Hcp Co." In: *Physical Review Letters* 72.13 (1994), pp. 2097–2100. DOI: 10.1103/physrevlett.72.2097.

[82] B. Koopmans, G. Malinowski, F. Dalla Longa, D. Steiauf, M. Fähnle, T. Roth, M. Cinchetti, and M. Aeschlimann. "Explaining the Paradoxical Diversity of Ultrafast Laser-Induced Demagnetization." In: *Nature Materials* 9.3 (2010), pp. 259–265. DOI: 10.1038/nmat2593.

[83] A Eschenlohr, M Battiato, P Maldonado, et al. "Ultrafast Spin Transport as Key to Femtosecond Demagnetization." In: *Nature Materials* 12.4 (2013), pp. 332–336. DOI: 10.1038/nmat3546.

[84] A Weber, F Pressacco, S Günther, E Mancini, P M Oppeneer, and C H Back. "Ultrafast Demagnetization Dynamics of Thin Fe/W(110) Films: Comparison of Time- and Spin-Resolved Photoemission with Time-Resolved Magneto-Optic Experiments." In: *Physical Review B* 84.13 (2011), p. 132412. DOI: 10.1103/physrevb.84.132412.

[85] J Hohlfeld, E Matthias, R Knorren, and K H Bennemann. "Nonequilibrium Magnetization Dynamics of Nickel." In: *Physical Review Letters* 78.25 (1997), pp. 4861–4864. DOI: 10.1103/physrevlett.78.4861.

[86] U Atxitia, O Chubykalo-Fesenko, J Walowski, A Mann, and M Münzenberg. "Evidence for Thermal Mechanisms in Laser-Induced Femtosecond Spin Dynamics." In: *Physical Review B* 81.17 (2010), p. 174401. DOI: 10.1103/physrevb.81.174401.

[87] T. Roth, A. J. Schellekens, S. Alebrand, O. Schmitt, D. Steil, B. Koopmans, M. Cinchetti, and M. Aeschlimann. "Temperature Dependence of Laser-Induced Demagnetization in Ni: A Key for Identifying the Underlying Mechanism." In: *Physical Review X* 2.2 (2012), p. 021006. DOI: 10.1103/PhysRevX.2.021006.

[88] Chuangtang Wang and Yongmin Liu. "Ultrafast Optical Manipulation of Magnetic Order in Ferromagnetic Materials." In: *Nano Convergence* 7.1 (2020), p. 35. DOI: 10.1186/s40580-020-00246-3.

[89] Vivek Unikandanunni, Rajasekhar Medapalli, Eric E. Fullerton, Karel Carva, Peter M. Oppeneer, and Stefano Bonetti. "Anisotropic Ultrafast Spin Dynamics in Epitaxial Cobalt." In: *Applied Physics Letters* 118.23 (2021), p. 232404. DOI: 10.1063/5.0049692.

[90] Michael Krauß, Tobias Roth, Sabine Alebrand, Daniel Steil, Mirko Cinchetti, Martin Aeschlimann, and Hans Christian Schneider. "Ultrafast Demagnetization of Ferromagnetic Transition Metals: The Role of the Coulomb Interaction." In: *Physical Review B* 80.18 (2009), p. 180407. DOI: 10.1103/PhysRevB.80.180407.

[91] J. -Y. Bigot, M. Vomir, L. H. F. Andrade, and E. Beaurepaire. "Ultrafast Magnetization Dynamics in Ferromagnetic Cobalt: The Role of the Anisotropy." In: *Chemical Physics*. Molecular Nanoscience 318.1 (2005), pp. 137–146. DOI: 10.1016/j.chemphys.2005.06.016.

[92] Zaiyao Fei, Bevin Huang, Paul Malinowski, et al. "Two-Dimensional Itinerant Ferromagnetism in Atomically Thin Fe3GeTe2." In: *Nature Materials* 17.9 (2018), pp. 778–782. DOI: 10.1038/s41563-018-0149-7.

[93] Houlong L. Zhuang, P. R. C. Kent, and Richard G. Hennig. "Strong Anisotropy and Magnetostriction in the Two-Dimensional Stoner Ferromagnet Fe3FeTe2." In: *Physical Review B* 93.13 (2016), p. 134407. DOI: 10.1103/PhysRevB.93.134407.

[94] Andrei Kirilyuk, Alexey V Kimel, and Theo Rasing. "Ultrafast Optical Manipulation of Magnetic Order." In: *Reviews of Modern Physics* 82.3 (2010), pp. 2731–2784. DOI: 10.1103/revmodphys.82.2731.

[95] H. P. Myers and Willie Sucksmith. "The Spontaneous Magnetization of Cobalt." In: *Proceedings of the Royal Society of London. Series A. Mathematical and Physical Sciences* 207.1091 (1997), pp. 427–446. DOI: 10.1098/rspa.1951.0132.

[96] P. B. Johnson and R. W. Christy. "Optical Constants of Transition Metals: Ti, V, Cr, Mn, Fe, Co, Ni, and Pd." In: *Physical Review B* 9.12 (1974), pp. 5056–5070. DOI: 10.1103/PhysRevB.9.5056.

[97] Wolfgang S. M. Werner, Kathrin Glantschnig, and Claudia Ambrosch-Draxl. "Optical Constants and Inelastic Electron-Scattering Data for 17 Elemental Metals." In: *Journal of Physical and Chemical Reference Data* 38.4 (2009), pp. 1013–1092. DOI: 10.1063/1.3243762.

[98] G. Malinowski, F. Dalla Longa, J. H. H. Rietjens, P. V. Paluskar, R. Huijink, H. J. M. Swagten, and B. Koopmans. "Control of Speed and Efficiency of Ultrafast Demagnetization by Direct Transfer of Spin Angular Momentum." In: *Nature Physics* 4.11 (2008), pp. 855–858. DOI: 10.1038/nphys1092.

[99] J. Walowski, G. Müller, M. Djordjevic, M. Münzenberg, M. Kläui, C. A. F. Vaz, and J. A. C. Bland. "Energy Equilibration Processes of Electrons, Magnons, and Phonons at the Femtosecond Time Scale." In: *Physical Review Letters* 101.23 (2008), p. 237401. DOI: 10.1103/PhysRevLett.101.237401.

[100] P. A. Joy and S. Vasudevan. "Optical-Absorption Spectra of the Layered Transition-Metal Thiophosphates MPS3 (M=Mn, Fe, and Ni)." In: *Physical Review B* 46.9 (1992), pp. 5134–5141. DOI: 10.1103/PhysRevB.46.5134.

[101] Adam K. Budniak, Szymon J. Zelewski, Magdalena Birowska, Tomasz Woźniak, Tatyana Bendikov, Yaron Kauffmann, Yaron Amouyal, Robert Kudrawiec, and Efrat Lifshitz. "Spectroscopy and Structural Investigation of Iron Phosphorus Trisulfide—FePS3." In: *Advanced Optical Materials* 10.7 (2022), p. 2102489. DOI: 10.1002/adom.202102489.

[102] Anudeepa Ghosh, Mainak Palit, Sujan Maity, Vivek Dwij, Sumesh Rana, and Subhadeep Datta. "Spin-Phonon Coupling and Magnon Scattering in Few-Layer Antiferromagnetic FePS3." In: *Physical Review B* 103.6 (2021), p. 064431. DOI: 10.1103/PhysRevB.103.064431.

[103] D. Vaclavkova, M. Palit, J. Wyzula, et al. "Magnon-Polarons in van Der Waals Antiferromagnet FePS3." In: *arXiv:2108.10945 [cond-mat]* (2021). arXiv: 2108.10945 [cond-mat].

[104] H. J. Zeiger, J. Vidal, T. K. Cheng, E. P. Ippen, G. Dresselhaus, and M. S. Dresselhaus. "Theory for Displacive Excitation of Coherent Phonons." In: *Physical Review B* 45.2 (1992), pp. 768–778. DOI: 10.1103/PhysRevB.45.768.

[105] R Merlin. "Generating Coherent THz Phonons with Light Pulses." In: *Solid State Communications* 102.2-3 (1997), pp. 207–220. DOI: 10.1016/s0038-1098(96)00721-1.

[106] Min-Cheol Lee, Choong H. Kim, Inho Kwak, et al. "Strong Spin-Phonon Coupling Unveiled by Coherent Phonon Oscillations in Ca 2 RuO 4." In: *Physical Review B* 99.14 (2019), p. 144306. DOI: 10.1103/PhysRevB.99.144306.

[107] *Broadband Impulsive Stimulated Raman Scattering Based on a Chirped Detection*. DOI: 10.1021/acs.jpclett.9b03061. (Visited on 08/20/2023).

[108] Flavio Giorgianni, Mattia Udina, Tommaso Cea, et al. "Terahertz Displacive Excitation of a Coherent Raman-active Phonon in V2O3." In: *Communications Physics* 5.1 (2022), pp. 1–7. DOI: 10.1038/s42005-022-00882-7.

[109] Qi Zhang, Mykhaylo Ozerov, Emil Vinas Boström, et al. "Coherent Strong-Coupling of Terahertz Magnons and Phonons in a Van Der Waals Antiferromagnetic Insulator." In: *arXiv:2108.11619 [cond-mat]* (2021). arXiv: 2108.11619 [cond-mat].

[110] M. Bernasconi, G. L. Marra, G. Benedek, L. Miglio, M. Jouanne, C. Julien, M. Scagliotti, and M. Balkanski. "Lattice Dynamics of Layered MP X 3 ($M=$ Mn,Fe,Ni,Zn; $X=$ S,Se) Compounds." In: *Physical Review B* 38.17 (1988), pp. 12089–12099. DOI: 10.1103/PhysRevB.38.12089.

[111] F. Keffer and C. Kittel. "Theory of Antiferromagnetic Resonance." In: *Physical Review* 85.2 (1952), pp. 329–337. DOI: 10.1103/PhysRev.85.329.

[112] Sheng Liu, Andrés Granados del Águila, Dhiman Bhowmick, et al. "Direct Observation of Magnon-Phonon Strong Coupling in Two-Dimensional Antiferromagnet at High Magnetic Fields." In: *Physical Review Letters* 127.9 (2021), p. 097401. DOI: 10.1103/PhysRevLett.127.097401.

[113] Yu-Jia Sun, Jia-Min Lai, Si-Min Pang, Xue-Lu Liu, Ping-Heng Tan, and Jun Zhang. "Magneto-Raman Study of Magnon–Phonon Coupling in Two-Dimensional Ising Antiferromagnetic FePS $_3$." In: *The Journal of Physical Chemistry Letters* (2022), pp. 1533–1539. DOI: 10.1021/acs.jpclett.2c00023.

[114] E. Evers, T. Kazimierczuk, F. Mertens, D. R. Yakovlev, G. Karczewski, T. Wojtowicz, J. Kossut, M. Bayer, and A. Greilich. "Nuclear Spin Dynamics Influenced and Detected by Electron Spin Polarization in CdTe/(Cd,Mg)Te Quantum Wells." In: *Physical Review B* 99.4 (2019), p. 045303. DOI: 10.1103/PhysRevB.99.045303.

[115] Sebastian F. Maehrlein, Ilie Radu, Pablo Maldonado, et al. "Dissecting Spin-Phonon Equilibration in Ferrimagnetic Insulators by Ultrafast Lattice Excitation." In: *Science Advances* 4.7 (2018), eaar5164. DOI: 10.1126/sciadv.aar5164.

[116] Y Takano, N Arai, A Arai, Y Takahashi, K Takase, and K Sekizawa. "Magnetic Properties and Specific Heat of MPS3 (M=Mn, Fe, Zn)." In: *Journal of Magnetism and Magnetic Materials*. Proceedings of the International Conference on Magnetism (ICM 2003) 272–276 (2004), E593–E595. DOI: 10.1016/j.jmmm.2003.12.621.

Acknowledgements

After the completion of the thesis and the work of several years, I want to express my deepest gratitude to many individuals who have been part of this time and deserve some recognition.

First and foremost, I want to thank Prof. Dr. Mirko Cinchetti for the supervision of the thesis and for giving me the opportunity to perform research on this interesting topic. Thank you for the many discussions and for being a good teacher. Next, I want to thank Dr. Davide Bossini for his supervision. I learned a lot from you about science, presentations, writing and project management. I wish you a lot of success in your group in Konstanz. Thank you, Dr. Stefano Ponzoni, for teaching me so much about scientific instrumentation and experimental methods. I strongly appreciated your input and experience when we built the lab. You are an outstanding experimentalist. I also want to thank Dr. Alexandra Kalashnikova for her contribution on the project initialization, the discussions and the contribution to the $FePS_3$ paper. The time in 2020 I could spend in your group taught me a lot and I value it very much. Although we did not directly work on the same project, I still want to thank you, Dr. Matija Stupar and Dr. Giovanni Zamborlini. I enjoyed every discussion with you and I could always approach you with questions in the fields of your specialty. Thank you, Dr. Umut Parlak for joining the team. I strongly appreciate your commitment in the lab and talking about new ideas with you. Additionally, I want to acknowledge my fellow (former) PhD students, who have been alongside me throughout this journey. Especially I want to name those who shared the time in the lab with me or accompanied me from the beginning: David, Marc, Sophie, Henning and Mattia. We had some tough but very enjoyable times together. Thank you for this and for all the memories.

Im Anschluss möchte ich mich auch bei denen bedanken, die mir außerhalb der Uni den nötigen Rückhalt gegeben haben. Bei all den Freunden, die mich schon seit Ewigkeiten begleiten und bei denen, die in den Jahren des Studiums dazu gekommen sind und jetzt genauso unmöglich wegzudenken sind. Vor allem möchte ich mich auch bei meiner Familie bedanken, die mir immer den Rücken gestärkt hat. Besonders bei meinen Eltern und meinem Bruder Frederick: Ich danke euch für alles!